Abstract

Production of ^{26}Al in Oxygen-Neon-Magnesium Novae

Anuj Ramesh Parikh

2006

In the beta-decay of the ground state of ^{26}Al (denoted ^{26g}Al, $t_{1/2} = 7.2 \times 10^5$ y), a characteristic 1.809 MeV gamma-ray is emitted. This signature of the presence of ^{26g}Al has been widely observed throughout the Galaxy. Indeed, the observation of this gamma-ray proves the ongoing nucleosynthesis of ^{26g}Al in astrophysical environments, given its short half-life on cosmological timescales. Reproduction of the Galactic ^{26g}Al steady-state abundance implied by the observations (~ 3 $M_{\odot}$) provides a powerful constraint on nucleosynthesis model calculations. These calculations may also be used to determine the relative contributions to the ^{26g}Al abundance by different types of astrophysical phenomena.

The amount of ^{26g}Al produced in nova explosions on oxygen-neon-magnesium white dwarfs is thought to be relatively minor (~ 0.1 - 0.4 $M_{\odot}$). Nuclear uncertainties in the ^{25}Al(p,γ)^{26}Si and ^{26g}Al(p,γ)^{27}Si reactions may change this by a factor of ~2, however. A direct study of the ^{25}Al(p,γ)^{26}Si reaction has been proposed and accepted at the TRIUMF-ISAC radioactive beams facility in Vancouver, Canada, and is awaiting the production of a sufficiently-intense ^{25}Al beam. To both guide this direct study, and to improve the accuracy of the current ^{25}Al(p,γ)^{26}Si calculations (based on indirect measurements), we have made a new measurement of the ^{26}Si mass. We find the mass excess of ^{26}Si to be

$\Delta(^{26}Si)$ = -7139.5 ± 1.0 keV; this new mass leads to a reduction in the $^{25}Al(p,\gamma)^{26}Si$ rate by as much as ~30% at nova temperatures. We have also made new measurements of the energy and strength of a key resonance for the $^{26g}Al(p,\gamma)^{27}Si$ reaction: we find E_R^{CM} = 184 ± 1 keV and $\omega\gamma = 35 \pm 4_{stat} \pm 5_{sys}$ μeV. These results lead to a decrease in the $^{26g}Al(p,\gamma)^{27}Si$ rate by as much as ~15% at nova temperatures.

Our measurements of the ^{26}Si mass and the resonance in $^{26g}Al(p,\gamma)^{27}Si$ both imply an increase in the ^{26g}Al yield from novae, but still confirm the secondary nature of their contribution to the Galactic abundance of ^{26g}Al.

Production of ^{26}Al in Oxygen-Neon-Magnesium Novae

A Dissertation

Presented to the Faculty of the Graduate School

of

Yale University

in Candidacy for the Degree of

Doctor of Philosophy

by

Anuj Ramesh Parikh

Dissertation Director: Peter D. Parker

December 2006

Table of Contents

List of Figures

List of Tables

List of Acronyms

ADC – Analog-to-Digital Converter

AGB – Asymptotic-Giant-Branch star

BGO – Bismuth Germanium Oxide

CCSN – Core-Collapse Supernova

CFD – Constant-Fraction Discriminator

CNO – Carbon-Nitrogen-Oxygen cycle

CO – Carbon-Oxygen white dwarf

COMPTEL – the imaging COMPton TELescope on the Compton Gamma-ray Observatory

CSD – Charge-State Distribution

CSF – Charge-State Fraction

DC – Direct Capture

DRAGON – Detector of Recoils And Gammas Of Nuclear reactions

DSSSD – Double-Sided Silicon Strip Detector

DWBA – Distorted Wave Born Approximation

EMS – ElectroMagnetic Separator

FWHM – Full Width at Half Maximum

HRMS – High Resolution Mass Separator

IC – Ionization Chamber

INTEGRAL – INTErnational Gamma-Ray Astrophysics Laboratory

ISAC – Isotope Separation and ACceleration facility at TRIUMF

ISM – InterStellar Medium

ISOL – Isotope Separation OnLine

LIS – Laser Ionization System

LMS – Left Mass Slit of DRAGON

MCP – MicroChannel Plate

OLIS – OffLine Ion Source

ONeMg – Oxygen-Neon-Magnesium white dwarf

PIDC – Position-sensitive Ionization Drift Chamber

PMT – PhotoMultiplier Tube

PSA – Position-Sensitive Assembly

RFQ – RadioFrequency Quadrupole

RHESSI – Ramaty High Energy Solar Spectroscopic Imager

TAC – Time-to-Amplitude Converter

TNR – ThermoNuclear Runaway

TOF – Time-Of-Flight

TRIUMF – TRI-University Meson Facility

WNSL – Wright Nuclear Structure Laboratory

Acknowledgements

I owe many thanks to many people, not only for help in the completion of this work, but also for making my time as a student in New Haven thoroughly entertaining.

Peter Parker has been an ideal supervisor for my graduate studies, allowing me the freedom to pursue and investigate the different areas of nuclear astrophysics. With his levelheaded approach to research, insight and experience in the field, and friendly demeanor, he creates an environment in which students feel comfortable, confident, and valued. I look forward to trading dry remarks with him in the future.

John D'Auria, my undergraduate advisor at SFU, continues to always be looking out for my best interests – helping me join the ^{26g}Al(p,γ) experiment at TRIUMF. Chris Ruiz, the PI of that experiment, graciously allowed me to horn in on his measurement. His efforts, along with those of Dave Hutcheon and Jonty Pearson, were crucial to ensuring the success of that work.

Jac Caggiano, postdoc and then research scientist at Yale when I joined the group, has a great, intuitive feel for experimental nuclear physics. Detectors, electronics, software and crazy ideas all fall under his majestic cloak. He motivated, and along with Ted Rounsaville, designed the current focal plane detector for the Split-pole spectrograph. His taste in nightclubs is highly questionable, however. Jason Clark, current postdoc with our group, is a tireless, relentless worker who takes nothing for granted. He has been of great help in understanding/fixing/improving/destroying our electronics.

Dale Visser and Rachel Lewis were graduate students when I arrived, and helped me learn the techniques and procedures of our group. Dale's work on JAM, as well as on other software, has made analysis of our data considerably less painful. Between her singing, meditation retreats and surreal 'dungeon parties', Rachel helped make our group much more interesting. Catherine Deibel and Chris Wrede are current graduate students. They have fit in very, very well, and our 'lunches' have been a welcome escape from the confines of WNSL.

Thanks to Jeff Ashenfelter, Sal DeFrancesco, Sam Ezeokoli, Walter Garnett, and Frank Lopez for keeping the Yale tandem running (relatively) smoothly. Thanks also to Marik Dombsky, Pierre Bricault, Jens Lassen, Bob Laxdal, and their teams for their incredible work in producing, ionizing and tuning the ^{26}Al beam at TRIUMF.

The backbone of WNSL is undoubtedly the support staff: thanks to Karen DeFelice, Paula Farnsworth, Kelli Kathman and Mary Anne Schulz, all of whom are instrumental in keeping the lab running smoothly; Tom Barker, Craig Miller and Richard Wagner for advice when things mysteriously break; and John Baris for help whenever my laptop hard drive died.

Last but never least, I thank my family and friends everywhere. A person is defined by their memories and stories, and thanks to you, I have lots of both (mostly true)!

for my parents

I. INTRODUCTION

A. Nuclear Astrophysics

"So how do real people benefit from your research?"

-countless friends, acquaintances and adversaries

Nuclear astrophysics addresses a deceptively simple question once thought to be objectively unanswerable, an issue that has piqued the curiosity of countless 'real people': where do we come from? Restating this as a more tractable question: what is the origin of the raw materials of which we are composed and by which we are surrounded? Certainly, the Big Bang was dominant in producing the hydrogen and helium in our universe, but where did everything else (see fig. 1) come from? Investigating the details behind the surprising answer (that 'everything else' is entirely material synthesized in astrophysical phenomena such as the interiors of stars or catastrophic explosions [Bur57]) comprises the efforts of scientists in this field.

There is great diversity in the astrophysical phenomena that enrich (or perhaps, pollute) space with their ejecta or outflow. These include (see e.g. [Rol88, Car96] for a review):

Type II supernovae: These explosive events are thought to be the greatest overall contributors to the enrichment of the interstellar medium. As massive stars ($\gtrsim 10$ $M_\odot$) evolve over their lifetimes of $\sim 10^7$ years, they are capable of producing all elements up to the Fe region via charged-particle fusion reactions. (Heavier elements may also be produced during the evolution of the star via the s-process.) However, once sufficient energy (and corresponding radiation pressure) can no longer be produced in this manner (see fig. 2), the star undergoes gravitational collapse. The core collapses faster than the outer layers (eventually becoming a neutron star or black hole, depending on the initial mass of the entire star), yielding a large flux of neutrinos that interacts with the envelope. These neutrinos deposit momentum and are thought to lead to the ejection of these layers in the energetic ($\sim 10^{51}$ ergs) supernova explosion (e.g. [Bet85]). Within the neutron wind ejected from the core region by the stream of neutrinos, nuclei above the Fe region may be created via the r-process. Release of nucleosynthesis products may also occur prior to the supernova for certain very massive ($\gtrsim 20$ $M_\odot$) stars. These are termed Wolf-Rayet stars and suffer gross mass loss ($\gtrsim 10^{-5}$ $M_\odot$/yr) through stellar wind.

<u>Type Ia supernovae</u>: In the evolution of low mass stars ($\lesssim 10$ $M_\odot$), charged-particle fusion reactions achieve temperatures and densities high enough to produce elements only up to the C/O/Ne/Mg region. (If the star has Fe-region 'seed' nuclei, the s-process may also occur within these stars, yielding elements heavier than Fe.) Once fusion ends, the outer layers disperse and a bare CO or ONeMg core (termed a white dwarf) remains. The mechanism for this mass loss towards the white dwarf stage is poorly understood: high angular momentum, superwinds, and thermal pulses are among the possible explanations. If this white dwarf lies in a binary system and accretes sufficient material (see fig. 3) from

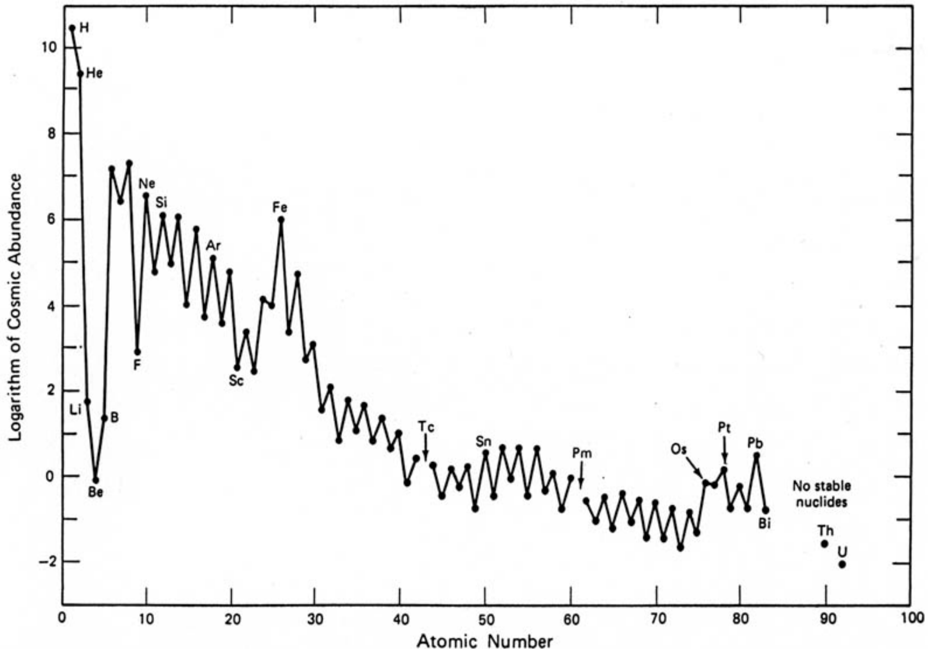

Figure 1: The abundances of the elements in the solar system, expressed as the logarithm of the number of atoms relative to 10^6 atoms of silicon. Data are from [And82].

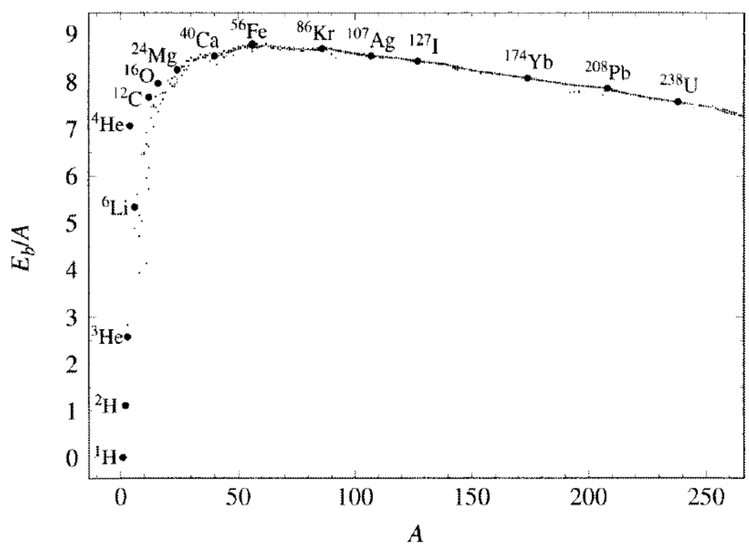

Figure 2: Binding energy per nucleon as a function of mass number. Charged-particle fusion reactions in stars create successively more bound nuclei, releasing energy. With the production of iron, however, further fusion reactions are no longer exothermic. Figure from [Car96].

its companion to reach the Chandreshekar mass of 1.4 $M_\odot$, the white dwarf then collapses under its own pressure – leading to increased temperatures and densities at which fusion reactions (creating elements up to the Fe region) can begin anew. (The merger of two white dwarfs may have a similar effect.) This sudden detonation has explosive results – the type Ia supernova – which distributes the

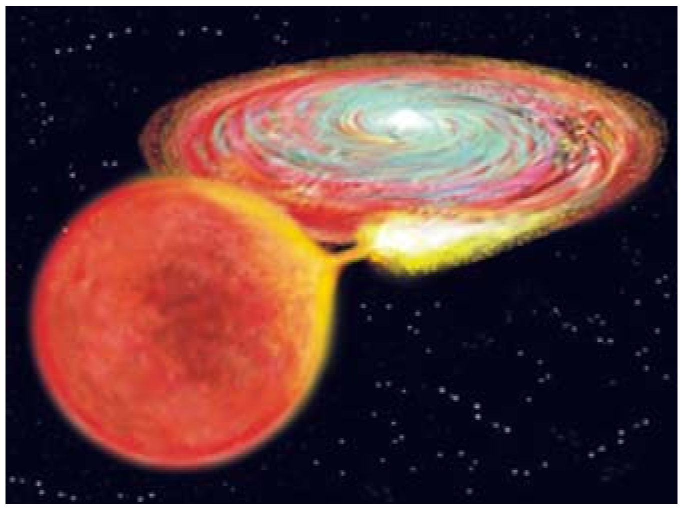

Figure 3: Artist's impression of a white dwarf binary star system, showing material flowing from a main-sequence star onto a white dwarf through an accretion disk. Figure from [NASA].

produced nuclei throughout the interstellar medium (ISM) and totally disrupts the white dwarf [Hil00]. We note that low mass stars may also release matter when they reach the asymptotic-giant-branch (AGB) stage in their evolution; instabilities and pulsations may give rise to mass loss at a rate of $\gtrsim 10^{-8}$ $M_\odot$/yr through stellar winds.

<u>X-ray bursts and novae</u>: these are both thought to be caused by thermonuclear ignition and runaway (TNR) in a shell of hydrogen-rich material accreted by a

compact object in a binary system – see fig. 3. If the compact object is a neutron star, temperatures and densities can be so extreme ($\gtrsim 10^9$ K and 10^6 g/cm^3) that elements on the proton-rich side of stability up to A ~ 60 [Woo04] -and perhaps even up to A ~ 100 [Sch01]- may be produced via the (α,p) and rp processes (releasing up to 10^{39} ergs over a few seconds). It is uncertain how much of this material is ejected during the burst due to the strong gravitational field of the neutron star; however, if the amount is even 1% of the accreted material, this may be enough to explain the abundances of certain isotopes [Sch01]. X-ray bursters have an accretion rate of ~ 10^{-8} $M_\odot$/yr and the nuclear burning is unstable, repeating on timescales of hours or days.

Novae occur when the compact object is a white dwarf; temperatures and densities in the explosion may reach $\gtrsim 10^8$ K and ~10^4 g/cm^3, and the energy output is ~10^{45} ergs over ~100 days. White dwarfs were thought to be composed primarily of carbon and oxygen until the observation of strong neon lines in some novae (e.g. Nova Cyg 1992, Nova QU Vul 1984) prompted the notion of another class of white dwarf enriched in heavier elements such as neon and magnesium. For a CO white dwarf, reactions between the hydrogen in the accreted shell and the underlying white dwarf material proceed mainly via the hot CNO cycle, yielding elements in the CNO region; for a ONeMg white dwarf, the NeNa and MgAl cycles will also be involved (see Chapter II). Breakout from these latter cycles to create somewhat heavier elements [Ili02, Geh98] may occur as well. The mass ejected from a single nova may reach 10^{-4} $M_\odot$ (the Galactic nova rate is

~ 30/year), with an accretion rate on the white dwarf of ~10^{-9} $M_{\odot}$/yr. Novae on ONeMg white dwarfs will be of particular interest in the present work.

The nucleosynthetic production in these various astrophysical sites is determined by both the environment (e.g. temperature, density and composition) and the relevant nuclear physics (e.g. the level structure of nuclei). These factors combine to give reaction rates which control the nuclear abundances produced within the lifetime of the source. So if we knew the nuclear structure and reaction rates for all involved nuclei in a particular site, as well as the temperature and density conditions at the site as a function of time, we could model the nucleosynthetic output from each site. We could then conjecture how these intermingle to give our observed solar system abundance distribution (fig. 1) - if we could also model the fraction of synthesized material that actually escapes the production site.

B. Gamma-ray Line Astronomy

When radioactive nuclei are produced at nucleosynthesis sites, they may beta-decay to a daughter nucleus in an excited state, which subsequently de-excites through the emission of a gamma-ray (see fig. 4). It is the search for these characteristic gamma-ray 'signatures' -uniquely identifying the daughter nuclei- that currently occupies many astrophysicists. The high penetrating power of gamma-rays permits direct translation of these observables into abundances of the mother nuclei, which can then be used to constrain and test nucleosynthesis models. (Obtaining absolute abundances using measurements from elsewhere in the electromagnetic spectrum generally requires assumptions regarding line excitation in whatever medium is involved. See e.g. [Rya99], where ^{7}Li abundances are extracted from absorption lines in stellar atmospheres.)

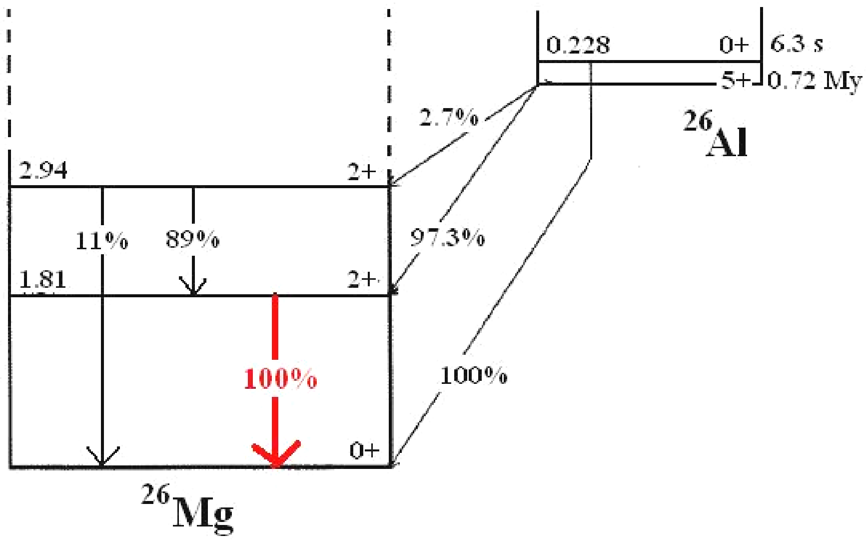

Figure 4: the beta-decay of the ground and first excited states of ^{26}Al to states in ^{26}Mg. The beta-decay of the ground state of ^{26}Al results in the emission of the 1.809 MeV gamma-ray; the first excited state of ^{26}Al bypasses the emission of any gamma-ray through a superallowed beta-decay to the ground state of ^{26}Mg. Figure after [End90].

The number of present radioactive nuclei n is related to the flux F in a gamma-ray line as

$$n = F \cdot 4\pi \cdot d^2 \cdot \tau ,$$

where τ is the lifetime of the radioactive nucleus and d is the source distance. The number of radioactive nuclei originally produced n_0 is just

$$n_0 = ne^{\frac{t}{\tau}},$$

where t is the time elapsed since production. So, the nucleosynthesis yield of the mother nucleus M_0 (in $M_\odot$) follows from F simply as:

$$M_0 = 3.12 \times 10^{-12} \cdot \frac{F}{d^2} \cdot \frac{\tau}{m} \cdot \frac{1}{B_m B_d} e^{\frac{t}{\tau}} \tag{1}$$

where F is in photons cm^{-2}s^{-1}, d is in parsecs, τ is in years, m is the molecular weight of the daughter, B_m is the branching ratio of the mother-to-daughter decay and B_d is the branching ratio of the observed gamma-ray in the de-excitation of the daughter.

Some conditions deserve note: for a nucleus to be useful for gamma-ray astronomy, the gamma-ray it emits in its decay must escape from the often-dense environment in which the species was formed. From mean free path arguments, a few days are necessary for a nova envelope, say, to become transparent to gamma-rays [Car96]; therefore, this timescale forms a rough lower bound on the lifetime of a radioactive species that can be observed through its gamma-ray signature. As well, the intensity of gamma-rays detected from very long-lived radioisotopes (relative to the occurrence rate of events which create those isotopes) may consist of the superposition of the emission from several (possibly different) nucleosynthesis events distributed in both time and space. In this case, a ‘steady-state’ abundance of this isotope is extracted (i.e. the exponential factor in eq. (1)

is not included). Complications arise because these contributing sources may be at different distances along the line-of-sight; the 3-D spatial distribution of the sources must be found to interpret the observed flux *F* (see section C).

Given these caveats, gamma-ray line observers have identified important and/or promising candidates for searches: some of these are included in table I.

Table I: Isotopes from which observable γ-rays of astrophysical importance are expected.

Isotope	$t_{½}$	Decay Chain	principal γ-ray energies (keV)	Lines observed?
^{7}Be	53 d	$^{7}\mathrm{Be}\,(\beta^{+}\nu)\,^{7}\mathrm{Li}^{*}$	478	No; expected from novae [Her04]
^{22}Na	2.6 y	$^{22}\mathrm{Na}\,(\beta^{+}\nu)\,^{22}\mathrm{Ne}^{*}$	1275	No; expected from novae [Her04]
^{26g}Al	7.2x10^{5} y	$^{26g}\mathrm{Al}\,(\beta^{+}\nu)\,^{26}\mathrm{Mg}^{*}$	1809	Yes [e.g. Die03, Pra96]
^{44}Ti	60 y	$^{44}\mathrm{Ti}\,(\beta^{+}\nu)\,^{44}\mathrm{Sc}^{*}\,(\beta^{+}\nu)\,^{44}\mathrm{Ca}^{*}$	1157, 78, 68	Yes [Iyu94, Sch00, Vin01]
^{56}Ni	6.1 d	$^{56}\mathrm{Ni}\,(\beta^{+}\nu)\,^{56}\mathrm{Co}^{*}\,(\beta^{+}\nu)\,^{56}\mathrm{Fe}^{*}$	847, 1238, 812, 158	Yes [e.g. Mor95, Mah88]
^{57}Ni	36 h	$^{57}\mathrm{Ni}\,(\beta^{+}\nu)\,^{57}\mathrm{Co}^{*}\,(\beta^{+}\nu)\,^{57}\mathrm{Fe}^{*}$	1378, 122	Yes [Kur92]
^{60}Fe	1.5x10^{6} y	$^{60}\mathrm{Fe}\,(\beta^{-}\overline{\nu})\,^{60}\mathrm{Co}^{*}\,(\beta^{-}\overline{\nu})\,^{60}\mathrm{Ni}^{*}$	59, 1173, 1332	Yes [Smi04a, Smi04b, Har05]

Observation of the 1.809 MeV gamma-ray from the decay of the ground state of ^{26}Al helped establish the field of gamma-ray line astronomy. This gamma-ray is certainly the most widely and precisely observed out of the candidates in table I (see fig. 5); we discuss this further in the next section.

C. Observations and Sources of ^{26g}Al

When discussing ^{26}Al, a distinction must be made between the ground state ($t_{1/2}$ = 7.2 x 10^5 y, $J^\pi = 5^+$) and a relatively long-lived metastable state at E_x = 228 keV ($t_{1/2}$ = 6.3 s, $J^\pi = 0^+$). (Hereafter, the ground state will be denoted as ^{26g}Al, the metastable state as ^{26m}Al, and the general nucleus as simply ^{26}Al.) Figure 4 shows the ^{26}Al decay chain. The ground state beta-decays to the E_x = 1.809 MeV and E_x = 2.938 MeV states in ^{26}Mg, leading to a 1.809 MeV gamma-ray in 99.7% of all decays. The metastable state decays directly (100%) to the ground state of ^{26}Mg; *no gamma-ray results from the decay of ^{26m}Al!*

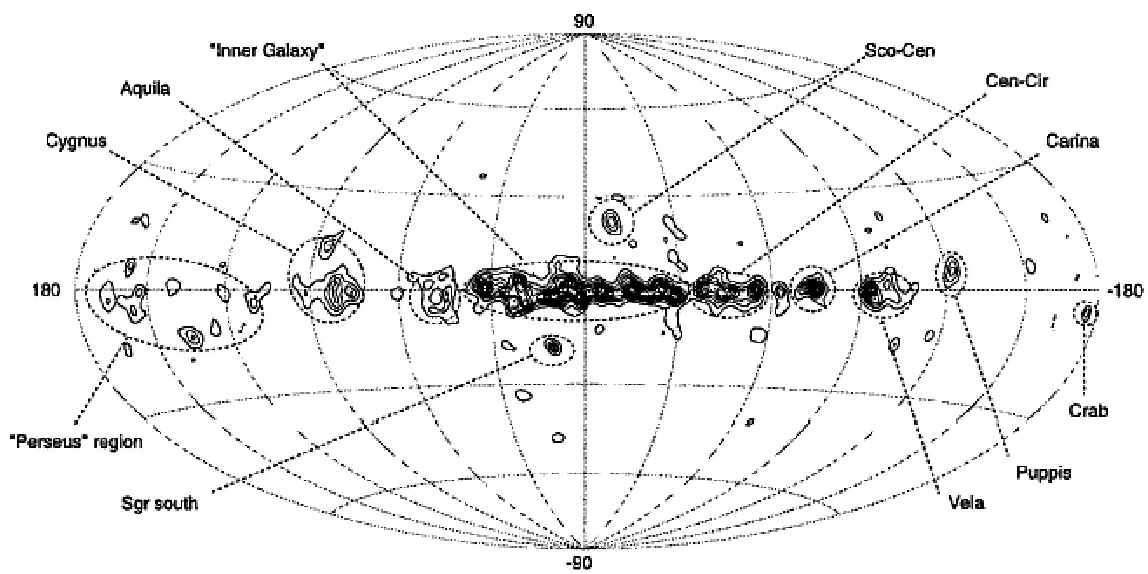

Figure 5: The 1.809 MeV all-sky map, as taken by the COMPTEL instrument on NASA's Compton Gamma-Ray Observatory. This image is based on 3.5 years of observations [Obe96]. Different regions of the Galaxy are labeled; contours indicate relative intensity. (See also [Plu01] for the COMPTEL map with 9 years of data.)

As we noted above, gamma-ray line measurements allow for comparisons between model predictions and observations. Since the 1.809 MeV beta-delayed gamma-ray line from the decay of ^{26g}Al is the most thoroughly examined, its intensity and distribution within the Galaxy provides one of the more robust constraints on nucleosynthesis models. Reproducing this abundance with a single model (or several models accounting for several different nucleosynthesis sites) would give much confidence in other abundance predictions of those models. Therefore, it is vital that the uncertainties in the nuclear reaction rates leading to the production of ^{26g}Al in various astrophysical sites are at least as small as the uncertainties in the gamma-ray observations. In discussing the nuclear physics (see Chapter II), we will concentrate on nucleosynthesis in novae on ONeMg white dwarfs and emphasize the particular uncertainties that the present work will address: the rates of the ^{25}Al(p,γ)^{26}Si and ^{26g}Al(p,γ)^{27}Si reactions.

Even before the 1.809 MeV gamma-ray had been observed, the presence of ^{26g}Al had been inferred (at least in the vicinity of our solar system) from measurements of its stable ^{26}Mg daughter in meteoric inclusions (e.g. [Lee76]). Figure 6 shows the correlation of the ^{26}Mg/^{24}Mg ratio to the ^{27}Al/^{24}Mg ratio as found from studies of inclusions in the Allende meteorite. As this meteorite is thought to have formed with the solar system, ~4.5 billion years ago, the correlation is interpreted as evidence that the excess ^{26}Mg arose from the *in-situ* decay of ^{26g}Al incorporated into these grains [Was82]. (The average present solar system ratio of ^{26}Mg/^{24}Mg is about 0.14.) Most of the data in fig. 6 is consistent with a ^{26g}Al/^{27}Al ratio of 5.5 x 10^{-5} at the time of formation of the meteorite.

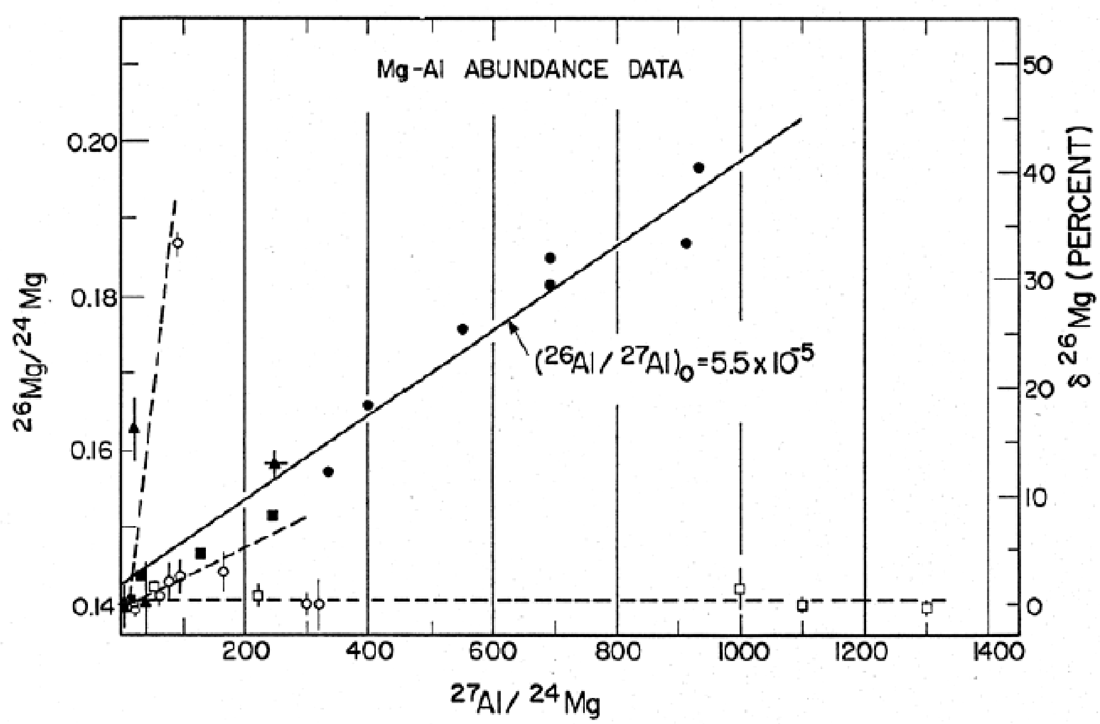

Figure 6: Compilation of $^{26}Mg/^{24}Mg$ and $^{27}Al/^{24}Mg$ measurements from the meteoritic studies of [Lee76, Lee77] (closed squares), [Lor77] (triangles), [Bra78] (closed circles), [Esa78] (open circles) and [Lee79] (open squares). Figure from [Cha82].

The inhomogeneous distribution of ^{26g}Al in the pre-solar nebula that is implied may have been the result of an explosive event that enriched the local ISM only a few million years before the solar condensation (i.e. before any large-scale mixing of its ejecta could occur). Indeed, this event may have *triggered* the formation of the solar system.

NASA's High Energy Astrophysics Observatory-3 (HEAO-3) satellite was the first to make astrophysical observations of the 1.809 MeV gamma-ray from the decay of ^{26g}Al [Mah82]; since then, multiple balloon and satellite-based instruments have reported positive measurements of this characteristic gamma-ray (see [Pra96] for a review). Recent results include the full-sky mapping of the line in the Galaxy by the COMPTEL instrument on NASA's Compton Gamma-Ray Observatory (CGRO) satellite [Obe96, Plu01] (see fig. 5), as well as high-resolution investigations of the shape of the line by NASA's Gamma-Ray Imaging Spectrometer (GRIS) balloon experiment [Nay96], NASA's Reuven Ramaty High Energy Solar Spectroscopic Imager (RHESSI) satellite [Smi03], and the SPI instrument aboard ESA's INTErnational Gamma-Ray Astrophysics Laboratory (INTEGRAL) satellite [Die03, Die06]. Details of the environment in which ^{26g}Al decayed can be inferred from the (Doppler-broadened) width of the line [Kre03]. A new study has interpreted their 1.809 MeV line-shape measurements to show that ^{26g}Al source regions co-rotate with the Galaxy, firmly establishing the Galactic origin of the observed ^{26g}Al gamma-rays [Die06].

Because ^{26g}Al is long-lived, only the steady-state mass of ^{26g}Al in the Galaxy can be found from gamma-ray observations. Recall from above that the 3-D spatial distribution of the 1.809 MeV sources is therefore required to obtain M_0 from the observed flux F (see eq. (1)). If one adopts a suitable 'tracer' for the ^{26g}Al emission, one may obtain this information. Diehl et al. (2006), in the analysis of INTEGRAL data, depend principally upon an observed correlation between free-free emission maps (radiation from free electrons accelerated by ionized atoms) and the 1.809 MeV emission map. Models for the Galactic distribution of free-free emission have been developed [Tay93, Cor02]; when they exploit the correlation, then, they find [Die06]

$$M(^{26g}Al) = (2.8 \pm 0.8)\ M_{\odot}.$$

Knodlseder (1999), in the analysis of COMPTEL data, also depends on this correlation between free-free and 1.809 MeV emission; he finds [Kno99]

$$M(^{26g}Al) = (3.1 \pm 0.9)\ M_{\odot}.$$

The question now arises as to where these ~ 3 $M_{\odot}$ of ^{26g}Al are produced in the Galaxy. Nucleosynthesis model calculations can determine the amount of ^{26g}Al arising from different astrophysical phenomena, assuming that both the environmental conditions (e.g. temperature, density, mixing of material) *and* the relevant nuclear reaction rates are known. Large uncertainties in the former continue to be an issue; as well, many reaction rates are still uncertain by orders of magnitude (e.g. [Ang99], [Ili01]). Nevertheless, calculations are made in the hope of identifying the most serious uncertainties involved in the interpretation of the results. The convergence of models using different assumptions for the environments and different theoretical calculations for the unknown nuclear physics may also help determine to which uncertainties the calculations are most sensitive.

Wolf-Rayet stars: These may contribute ~1 $M_\odot$ of ^{26g}Al to the steady-state abundance through their winds [Pal05, Mey97]. Uncertainties in the mass-loss rate, mixing mechanism and, to a lesser degree, the nuclear physics (e.g. the ^{26g}Al(p,γ)^{27}Si rate) could affect this value by a factor of ~2 - 3 [Mey97].

AGB stars: Some models show these stars to be a relatively feeble source of ^{26}Al, contributing ~ 0.1 $M_\odot$ of ^{26g}Al [Mow00] to the steady state abundance; others show that these could be major sources [Baz93]. The treatment of convection in the models, as well as uncertainties in some key nuclear reaction rates (primarily ^{26g}Al(p,γ)^{27}Si) seems to give rise to the differences in the models [Bus99].

Core-collapse Supernovae (CCSN): Type II supernovae may be responsible for all of the ^{26g}Al in the galaxy, contributing ~2 $M_\odot$ [Tim95] to the steady-state abundance. As well, Type Ib and Ic supernovae may be similarly prolific sources [Hig04]. (Type Ib and Ic supernova are thought to originate from core-collapse scenarios like Type II; however, they lack hydrogen lines in their spectra. This may be due to mass transfer of the progenitor star's hydrogen envelope to a binary companion.) The uncertainty in the Galactic core-collapse supernova rate (1-3 per century) may change the contribution of these explosions by a factor of ~3.

The nuclear reaction rates adopted in the models also play a striking role, as was highlighted in the recent controversy over the ratio of ^{60}Fe to ^{26g}Al produced in CCSN (see below).

Novae: Novae on CO white dwarfs are thought to produce negligible amounts of ^{26}Al, if any [Jos98]. Calculations of the ^{26g}Al enrichment to the ISM from novae on ONeMg white dwarfs vary widely. Jose et al. (1997) predict a contribution of 0.1 - 0.4 $M_{\odot}$ [Jos97] to the steady-state abundance; however, this may change by a factor of ~2 because of uncertainties in the ^{25}Al(p,γ)^{26}Si and ^{26g}Al(p,γ)^{27}Si reaction rates [Jos99, Coc95]. The unknown lower limit on the mass of ONeMg white dwarfs may also affect this value by a factor of ~2 - 3 [Jos98]. Finally, uncertainty in both the total ejected mass from a nova and the fraction of novae that take place on ONeMg white dwarfs (though to be ~1/3 [Gil03]) could allow ONeMg novae to be important sources of ^{26g}Al.

Massive stars are considered by many to be the most likely origin of the majority of the ^{26g}Al in the Galaxy; the calculations mentioned above lend some support to this view. Further support arises from the irregular distribution of the 1.809 MeV emission in the COMPTEL map (fig. 5): since novae and low mass AGB stars may produce say, an order of magnitude less ^{26g}Al than core-collapse supernovae or Wolf-Rayet stars, many more of the former would be necessary to explain the observed flux. This would result in a much smoother flux distribution than observed [Pra96]. The observed correlation between free-free and 1.809 MeV emission mentioned earlier suggests a similar conclusion: free-free emission traces the distribution of ionized gas in the ISM, and massive stars are likely the dominant sources of this ionization [Abb82].

Recent observations with the RHESSI and INTEGRAL satellites of the 1.173 and 1.332 MeV gamma-ray lines from the decay of ^{60}Fe have generated more debate as to the origin of ^{26g}Al. Both ^{60}Fe ($t_{1/2}$ = 1.5 x 10^6 y) and ^{26g}Al ($t_{1/2}$ = 7.2 x 10^5 y) are expected to be produced in CCSN; moreover, their similar half-lives relative to the ~100 year occurrence rate of these supernovae mean that both will be present in steady-state abundances in the ISM. Nucleosynthesis models could therefore be used to calculate the expected ^{60}Fe/^{26g}Al ratio in CCSN for comparison with an observed ratio, to test whether or not the majority of ^{26g}Al is created in CCSN. (No other Galactic source is expected to create significant quantities of ^{60}Fe [Pra04].) Prantzos (2004) compiled and interpreted the ^{60}Fe/^{26g}Al ratio calculations of several models [Woo95, Tim95, Rau02, Lim03]; fig. 7 shows these, as well as the ratios as observed throughout the Galaxy by RHESSI [Smi04a, Smi04b] and INTEGRAL [Har05b]. The newer models use improved stellar physics and updated reaction rates relative to the older ones; as can be seen from fig. 7, the observations are in clear disagreement with the predictions of these newer models. If the newer models are to be believed, then, the observations imply that the Galactic abundance of ^{26g}Al is much larger than that which could be created from CCSN. Another source of ^{26g}Al (with a much lower ^{60}Fe/^{26g}Al ratio) seems to be required: Wolf-Rayet stars, AGB stars and novae could all be candidates. (A discussion at a recent conference indicated that this issue had been resolved, and that the problem had been rooted in the mistaken use of several out-of-date reaction rates in the newer CCSN models [NIC9]. If

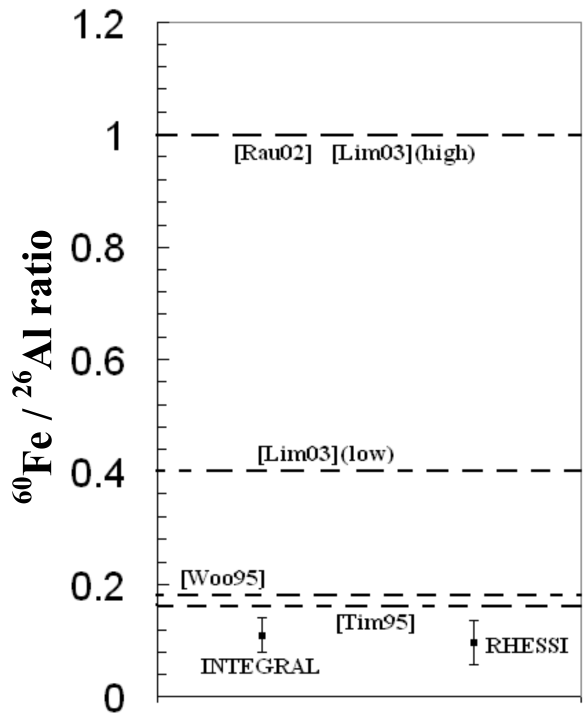

Figure 7: Galactic observations of the $^{60}Fe\,/\,^{26g}Al$ ratio compared to model calculations for production of these species in core-collapse supernovae. (The models of [Lim03] considered both "high" and "low" explosion energies.) Figure is based on the results of [Pra04]. The disagreement between the observations and the model predictions may be due to the use of out-of-date reaction rates – see text.

anything, then, this controversy helped to highlight the impact that nuclear reaction rates may have on the nucleosynthesis yields of the models.)

We note that uncertainty in the rate of the ^{25}Al(p,γ)^{26}Si reaction may lead to unexpected model-dependent changes in nucleosynthesis calculations of ^{26}Al. Runkle et al. (2001) find that when the abundance of ^{26}Si becomes sufficiently large in hydrogen-rich environments with T $\gtrsim$ 0.4 GK, models may need to consider the gamma-transitions linking the ground state and isomer of ^{26}Al [Run01]. Since most models treat ^{26g}Al and

^{26m}Al as essentially ‘separate nuclei’, evidence for an increase in the ^{25}Al(p,γ)^{26}Si rate may require revision of the models and their predictions.

Finally, we comment briefly on recent analyses of pre-solar SiC grains from primitive meteorites (e.g. [Ama01a - c]) with ^{26g}Al/^{27}Al ratios (inferred from large ^{26}Mg/^{24}Mg ratios relative to solar) ranging from 10^{-4} to 0.6 - compare fig. 6. Given the large range in model calculations of the ^{26}Al/^{27}Al ratio (e.g. 0.01 - 0.6 in novae [Jos04]), it is difficult to constrain the origins of these different grains. Again, improvements in our understanding of the nucleosynthesis of ^{26}Al in different astrophysical sites are necessary.

II. THE NUCLEOSYNTHESIS OF ^{26g}Al in ONeMg NOVAE

A. **The MgAl cycle**

Thermonuclear runaways (TNRs) on the surface of ONeMg white dwarfs commence producing ^{26}Al mainly through reactions with the isotopes of Mg – see fig. 8. This series of (p,γ) reactions and beta-decays is termed the MgAl cycle because of the ^{27}Al(p,α)^{24}Mg reaction that can return processed material back to a Mg isotope. It is important to note that at the temperatures associated with novae (T ~ 0.1 – 0.4 GK), thermal equilibrium is severely hindered between the ground and metastable states of ^{26}Al by the large spin difference (ΔJ = 5). They can effectively be treated as two separate isotopes when considering nucleosynthesis mechanisms in this environment [War80, Run01]. Since the beta-decay of ^{26m}Al does not result in a 1.809 MeV gamma-ray (see fig. 4), to interpret the 1.809 MeV gamma-ray observations in the context of novae we must understand the competition between the reaction sequences involved that do and do *not* lead to the emission of this gamma-ray. As the nucleus ^{26}Si beta-decays exclusively to ^{26m}Al through a superallowed transition, one key question is whether the ^{25}Al(p,γ)^{26}Si rate is faster in novae than the ^{25}Al beta-decay ($t_{1/2}$ = 7.2 s). If the ^{25}Al(p,γ)^{26}Si rate is faster, then the flow of matter from ^{24}Mg will bypass the production of ^{26g}Al, producing ^{26m}Al instead, and the 1.809 MeV gamma-ray intensity from novae will be reduced. Another reaction of obvious importance is ^{26g}Al(p,γ)^{27}Si, which destroys ^{26g}Al directly. Quite simply, the faster this rate is, the less ^{26g}Al is produced, and the 1.809 MeV gamma-ray intensity from these novae is again reduced.

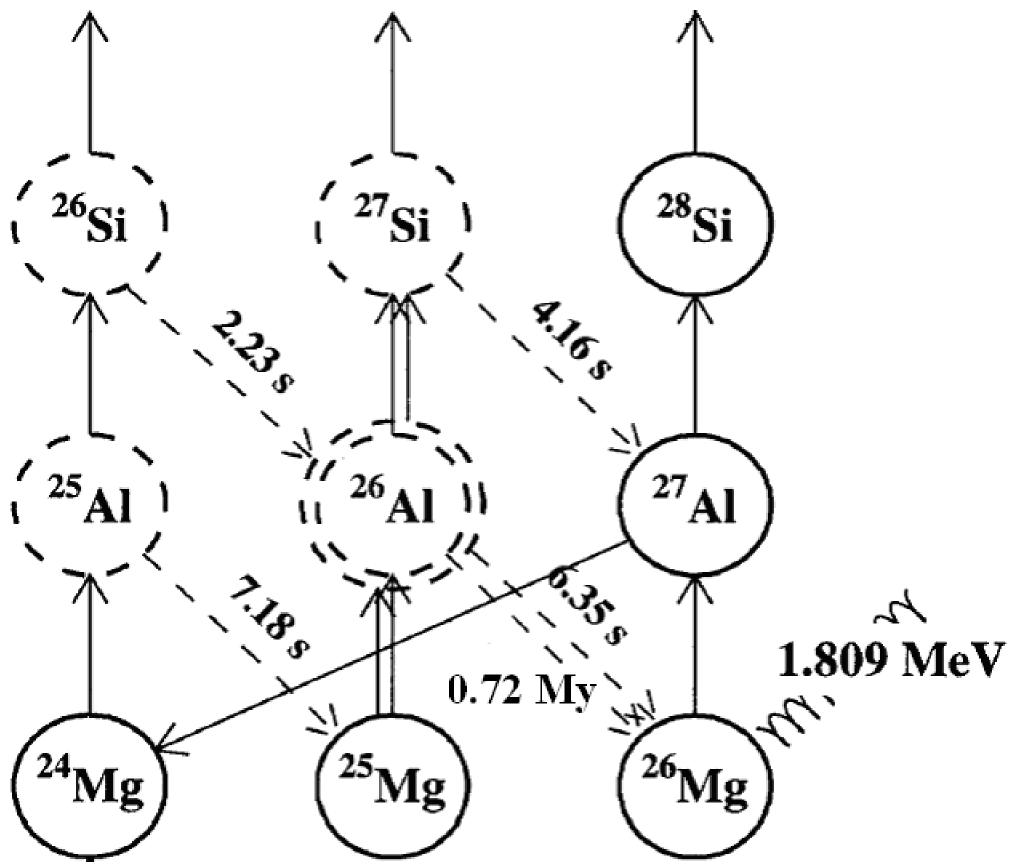

Figure 8: the MgAl cycle of nuclear reactions. Note the ground and isomeric states of ^{26}Al, which beta-decay with half-lives of 0.72 My and 6.35 s, respectively. Only in the decay of the ground-state of ^{26}Al is the 1.809 MeV gamma-ray emitted. Figure from [Jos99].

The uncertainties in the rates of the ^{25}Al(p,γ)^{26}Si and ^{26g}Al(p,γ)^{27}Si reactions are presently the largest contributors to the uncertainty in the amount of ^{26g}Al produced in nova nucleosynthesis models [Coc95, Jos99, Ili02].

B. **Reaction Rate Formalism**

Reaction rates have components due to both direct and resonant reaction mechanisms. The former type proceeds at all projectile energies, with a cross-section varying smoothly with energy; the latter type occurs when the energy of the projectile corresponds to the energy of an excited state in the compound nucleus. When the latter condition is fulfilled, the resonant component will be dominant. Calculations have shown that for both the ^{25}Al(p,γ)^{26}Si [Ili96] and ^{26g}Al(p,γ)^{27}Si [Cha93, Buc84] reactions, the direct-capture components are negligible at nova temperatures. Therefore, we do not discuss this reaction mechanism further here; however, see e.g. [Rol73, Rol88].

The resonant component of the reaction rate $<\sigma\upsilon>$ at temperature T, per particle pair, is given as [Rol88]

$$< \sigma\upsilon >= \left(\frac{2\pi}{\mu kT}\right)^{3/2} \hbar^2 \sum_i (\omega\gamma)_i \exp\left(\frac{-(E_{R,i}^{CM})}{kT}\right), \tag{2}$$

where the resonance strength *(ωγ)* is defined as

$$(\omega\gamma)_i = \frac{2J_i+1}{(2J_1+1)(2J_2+1)}\left(\frac{\Gamma_p\Gamma_\gamma}{\Gamma}\right)_i . \quad (3)$$

The sum in eq. (2) allows for the contributions of all the resonant states through which the reaction may proceed at the temperature of interest. Each resonance is labeled by spin J, resonance energy E_R^{CM}, and partial and total widths. For our purposes, the partial widths will be proton Γ_p and gamma Γ_γ partial widths, with $\Gamma_p + \Gamma_\gamma = \Gamma$. The spins J_1 and J_2 are those of the projectile and target, and μ is the reduced mass of the projectile-target system. For a resonance in a particular reaction, the resonance energy in the center-of-mass frame, E_R^{CM}, may be related to the excitation energy E_x of that state in the compound nucleus through $E_R^{CM} = E_x - Q$, where Q is the difference between the masses of the reactants and products in the reaction. Equation (2) is valid only if these resonant states are narrow ($\Gamma << E_R^{CM}$) and isolated ($E_{x,i} - E_{x,j} >> \Gamma_i$), which will be the case here. It should be noted that because of the exponential dependence of the rate on the resonance energy, any uncertainties in the resonance energies, excitation energies, or masses of the reactants and products may have a large effect on the rate.

Both direct and indirect experimental studies may be used to determine the E_R^{CM} and $(\omega\gamma)$ of concern for a particular reaction. A direct study of say, ^{26g}Al(p,γ)^{27}Si would involve an excitation function to determine the resonance energies E_R^{CM} [Buc84, Vog89]; explicitly, in normal kinematics, the cross-section of this reaction would be measured as a function of the energy of protons bombarding a (radioactive) ^{26g}Al target. (Inverse kinematics would have a ^{26g}Al beam bombarding a hydrogen target – see Chapter IV.) Large spikes in the cross-section correspond to values of E_R^{CM}. The resonance strengths

$(\omega\gamma)$ can be found by measuring thick-target yield curves for the resonances – see fig. 9. The maximum yield Y_{max} is proportional to the resonance strength [Rol88] through

$$Y_{\max} = \frac{\lambda^2}{2}(\omega\gamma)\frac{M+m}{M\varepsilon}, \tag{4}$$

where λ is the de Broglie wavelength in the center-of-mass frame, M and m are target and projectile masses, respectively, and ε is the stopping cross-section of the projectile in the target.

Indirect studies of the $^{26g}Al(p,\gamma)^{27}Si$ reaction rate involve transfer reactions (such as $^{28}Si(^3He,\alpha)^{27}Si$) to identify the excitation energies E_x of states in ^{27}Si. The Q-value of the $^{26g}Al(p,\gamma)^{27}Si$ reaction (that is, the *masses* of ^{26}Al, p, and ^{27}Si) would then be required to convert E_x to E_R^{CM}. Parameters comprising *$(\omega\gamma)$* –see eq. (3) – can also be found through indirect means. Reactions such as $^{27}Al(^3He,t)\,^{27}Si^*(p)^{26}Al$ may be studied to find proton branching ratios *(Γ_p / Γ)* for the states in ^{27}Si populated in the (^{3}He,t) reaction [Lew05]. As well, distorted-wave Born approximation (DWBA) calculations may be used in conjunction with transfer-reaction data measured as a function of scattering angle to find the spins J_i of the ^{27}Si states of interest. These DWBA fits may also determine Γ_p if the reaction studied involves the same nucleon transfer as the reaction desired (i.e. a (^{3}He,d) study to indirectly examine a (p,γ) reaction [Vog96]– a proton is transferred in both cases).

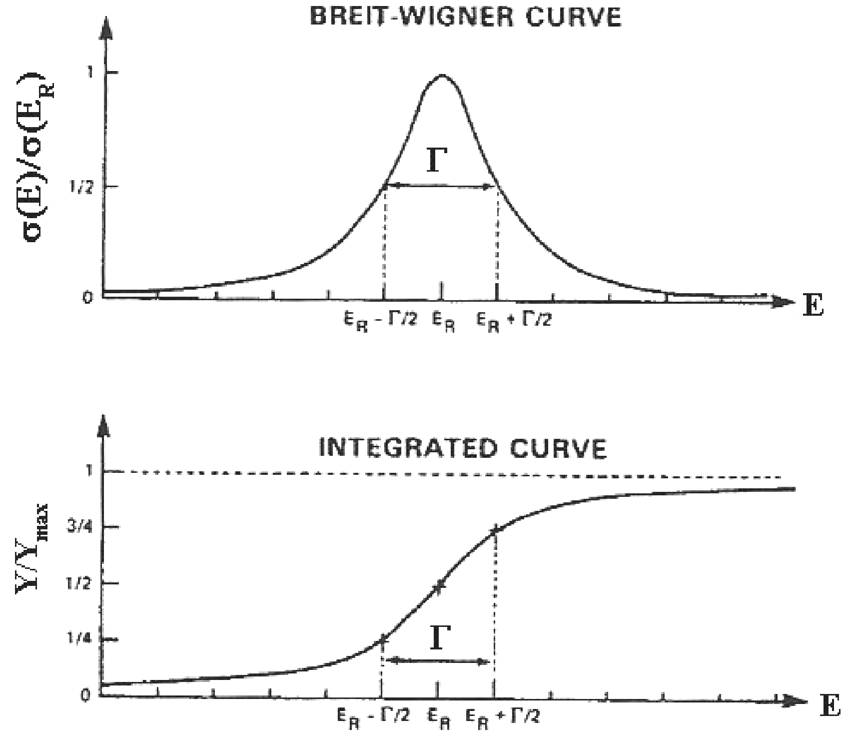

Figure 9: (top) For a thin target, the reaction yield of a narrow resonance follows the Breit-Wigner curve, with a maximum at the resonance energy E_R and a FWHM of Γ. (bottom) For a thick target, the reaction yield follows a curve resulting from the integration of the Breit-Wigner curve. Figure from [Rol88].

One may identify a rough 'energy region of interest' $E_0 \pm \Delta/2$ in a nucleus Y (given a reaction X+a → Y+ γ) within which nuclear structure information should be known to allow an accurate reaction rate calculation in an environment of temperature *T*. This is given as [Rol88]:

$$E_0 = 1.22(Z_1^2 Z_2^2 \mu T_6^2)^{1/3} \quad \text{keV}$$

and

$$\frac{\Delta}{2} = 0.375(Z_1^2 Z_2^2 \mu T_6^5)^{1/6} \quad \text{keV,} \tag{5}$$

where Z_1, Z_2 are the atomic numbers of the projectile and target, μ is the reduced mass in amu, and T_6 is the temperature in millions of K. Note that the value of E_0 is given relative to the Q-value of the reaction.

C. The ^{25}Al(p,γ)^{26}Si Reaction

Figure 10 shows the level structure of ^{26}Si, along with the energy region of interest $E_0 \pm \Delta/2$ (see eq. (5)) for the ^{25}Al(p,γ)^{26}Si reaction in ONeMg novae conditions (T = 0.1 - 0.4 GK). We see that resonances within about 500 keV of the 5.518 MeV Q-value (as calculated from [Aud03] – this is also known as the ^{25}Al + p threshold) will be the most important for calculating the reaction rate.

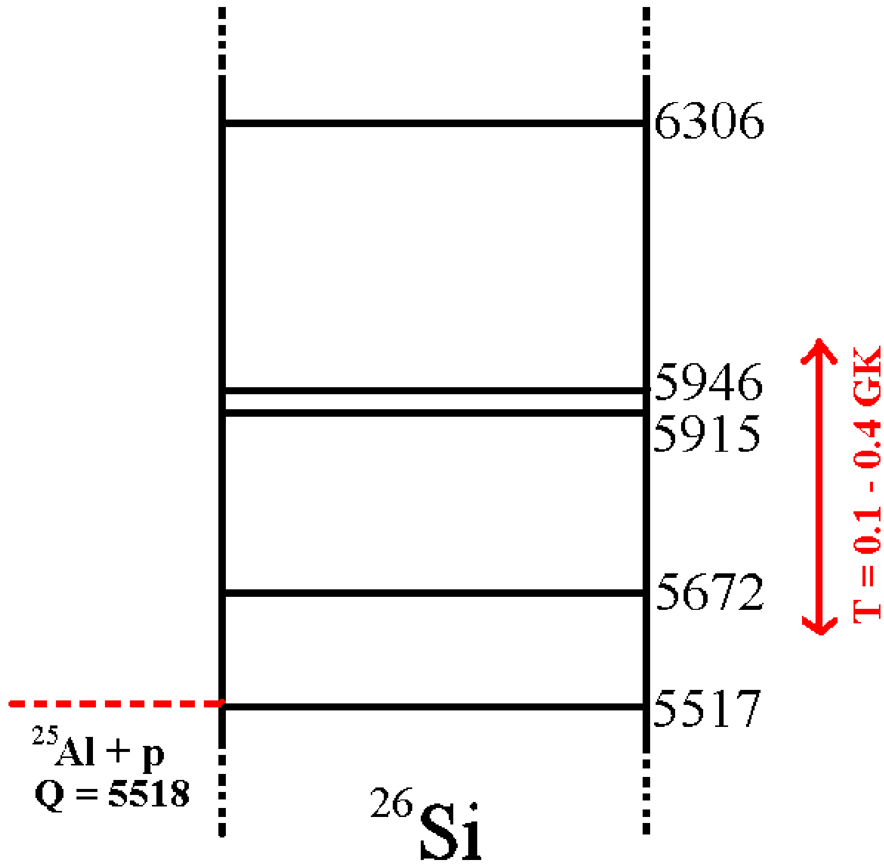

Figure 10: The level structure of ^{26}Si above the ^{25}Al + p threshold. The energy region of importance at nova temperatures is indicated (see eq. (5)). The Q-value of the ^{25}Al(p,γ)^{26}Si reaction is from [Aud03], and the excitation energies are weighted averages of the results from [Cag02], [Bar02] and [Par04].

Because an ^{25}Al ($t_{1/2}$ = 7.2 s) target is not feasible and a sufficiently intense ^{25}Al beam (> 10^9 ions/s) has not yet been produced at the world's radioactive beams facilities, a direct study of the ^{25}Al(p,γ)^{26}Si reaction has not been made (though a proposal has been accepted for a study at TRIUMF-ISAC once a ^{25}Al beam becomes available [Che01]). Much has been learned from indirect studies, however – see table II.

From comparison with the level structure of its much-studied stable "mirror" nucleus ^{26}Mg (with the same number of total nucleons as ^{26}Si, but interchanged proton and neutron numbers), Iliadis et al. (1996) predicted several levels in ^{26}Si within the energy range of interest for novae that had yet to be observed [End90]– including two unnatural-parity states of spin-parity 1^+ and 3^+. According to their calculations based on ^{26}Mg, they found that these two unnatural-parity states should be the strongest contributors to the ^{25}Al(p,γ) rate at nova temperatures [Ili96]. They also noted how the insufficient energy resolution (ΔE = 140 - 200 keV) of previous studies [Pad72, Boh82, Alf86] led to a possible unresolved 0^+, 4^+ doublet at E_x = 5.940(25) MeV that could be the second strongest contributors to the rate. In addition, for those states that had been observed, many had unknown spin-parity assignments or large (~30 keV) uncertainties in their excitation energies. These issues prompted several groups [Bar02, Cag02, Par04] to make new measurements of ^{26}Si above the proton threshold using the ^{28}Si(p,t)^{26}Si, ^{29}Si(^{3}He, ^{6}He) ^{26}Si and ^{24}Mg(^{3}He,n)^{26}Si reactions, respectively. Bardayan et al. (2002) observed two states in the relevant energy region for ^{25}Al(p,γ) at nova temperatures: at E_x = 5.515(5) MeV and 5.916(2) MeV. Through DWBA angular distribution calculations they determined the spins and parities of these as 4^+ and 0^+ respectively. Caggiano et al.

(2002) observed the 4^+ state of Bardayan et al. (at E_x = 5.526(8) MeV) as well as two other states at E_x = 5.678(8) and 5.945(8) MeV, which they argued to be the missing 1^+ and 3^+ states, respectively. (Note that two-nucleon transfer studies favor the population of *natural-parity* states in ^{26}Si because of angular momentum and parity conservation; the (^{3}He,^{6}He) reaction should be less selective.) Based on their measured resonance energies, Caggiano et al. confirmed that the unnatural-parity states should dominate the ^{25}Al(p,γ)^{26}Si rate at nova temperatures. Parpottas et al. (2004) generally confirm the excitation energies measured by Bardayan et al. and Caggiano et al. but disagree with their spin-parity assignments. (This group assigned spin-parity to their observed states by comparing their measured differential cross-sections with Hauser-Feshbach calculations.) Consequently, they also disagree in the identification of the dominant states for the ^{25}Al(p,γ)^{26}Si rate in novae. Thomas et al. (2004) find a 3^+ state at E_x = 5.929(5) MeV in ^{26}Si through a beta-decay study; it is unclear if this corresponds to the E_x = 5.916 or 5.945 MeV state (or yet another state) [Tho04].

Prior to these 'modern' measurements, the ^{25}Al(p,γ)^{26}Si reaction rate had been calculated based on shell-model results and mirror nucleus information; these determinations were estimated to be uncertain by 3 - 4 orders of magnitude [Ili96, Ili01, Coc95]. This error in the rate, when used in models of nova nucleosynthesis, led to a factor of ~2 [Jos99] or ~5 [Coc95] change in the amount of ^{26}Al produced. Although the new experimental information improves the models significantly, the rates may still be taken to be uncertain by 1 - 2 orders of magnitude due to the lack of any experimental information on the resonance strengths.

Table II: summary of known experimental information relevant for the $^{25}Al(p,\gamma)^{26}Si$ reaction in ONeMg novae. The excitation energy region in ^{26}Si is listed in MeV from the $^{25}Al + p$ threshold at E_x = 5.518 MeV [Aud03] to E_x = 6.1 MeV.

[End90] E_x	J^π	[Bar02] E_x	J^π	[Cag02] E_x	J^π [1]	[Par04] E_x	J^π	[Tho04] E_x	J^π
5.562(28)		5.515(5)	4+	5.526(8)	4+	5.515(4)	4+		
				5.678(8)	1+	5.670(4)	1+		
		5.916(2)	0+			5.912(4)	3+		
								5.929(5)	3+
5.940(25)	0+			5.945(8)	3+	5.946(4)	0+		

[1] Assignments are based on the shell model calculations and mirror nucleus considerations of [Ili96], as well as the results of [Bar02].

In addition to the proposal accepted for a direct measurement of the $^{25}Al(p,\gamma)^{26}Si$ reaction in inverse kinematics [Che01], another proposal has been accepted at TRIUMF to produce a ^{26}Al target through implantation of ^{26}Al ions in a carbon foil. This target would then be used to measure proton branching ratios Γ_p/Γ from ^{26}Si excited states via the $^{26}Al(^3He,t)^{26}Si^*(p)^{25}Al$ reaction [Dei05]. With complementary measurements or calculations of the total widths Γ of the states of concern in ^{26}Si, the resonance strengths could be found (see eq. (3)) and the $^{25}Al(p,\gamma)^{26}Si$ rate determined.

A source of uncertainty that also needs to be considered here lies in the Q-value of the $^{25}Al(p,\gamma)^{26}Si$ reaction. The importance of the nuclear masses in determining rates was emphasized recently in the direct study of the $^{21}Na(p,\gamma)^{22}Mg$ reaction [Bis03a,b]. Bishop et al. (2003) found a disagreement of 6.3 keV between their measured resonance energy (i.e. E_R^{CM}) and that calculated using E_x from indirect studies (i.e. transfer reactions) and the Q-value of the reaction. This issue was eventually resolved through new measurements of E_x [Sew05, Jew05] and the mass of ^{22}Mg [Sav04, Muk04, Har03]. Indeed, it was found that the mass of ^{22}Mg changed by about 3 keV – over twice the error listed in the mass evaluation [Aud03]. In the case of ^{25}Al(p,γ)^{26}Si, we require the E_x of states in ^{26}Si as well as the masses of ^{25}Al, p, and ^{26}Si. According to the latest atomic mass evaluation [Aud03], the proton mass is known to 0.1 eV, ^{25}Al to 0.5 keV and ^{26}Si to 3 keV. Because of the exponential dependence of the reaction rate on Q, and the fact that the recommended mass value is based upon only one measurement [Har74], we have made a new measurement of the ^{26}Si mass (see Chapter III, and [Par05] as well). Our measurement will also aid in determining the resonance energy regions to be examined in the future direct study of the ^{25}Al(p,γ)^{26}Si reaction.

D. The ^{26g}Al(p,γ)^{27}Si Reaction

Figure 11 shows the level structure of ^{27}Si, along with the energy region of interest $E_0 \pm \Delta/2$ (see eq. (5)) for the ^{26g}Al(p,γ)^{27}Si reaction in ONeMg novae conditions (T = 0.1 - 0.4 GK). Resonances within 500 keV of the 7.463 MeV Q-value [Aud03] (or ^{26g}Al + p threshold) will be the most important for determining the reaction rate in novae.

The ^{26g}Al(p,γ)^{27}Si reaction has been studied both directly and indirectly. Table III summarizes the known experimental information about the ^{26g}Al(p,γ)^{27}Si reaction, as is relevant to nova burning. Buchmann et al. (1984) –the first group to explore the level structure of ^{27}Si above the ^{26g}Al + p threshold– measured an excitation function using protons bombarding a ^{26g}Al target, and found 7 resonances within E_R^{CM} = 250 - 900 keV

(E_x = 7.7 – 8.4 MeV). They also used the thick-target method to find the strengths of these resonances [Buc84]. Schmalbrock et al. (1986) in an examination of ^{27}Si level structure from E_x = 4.1 – 8.4 MeV via the ^{28}Si(^{3}He,α)^{27}Si reaction, found 18 states between E_x = 7.464 and E_x = 8.4 MeV [Sch86]; only two of these had been seen by Buchmann et al. These measurements were largely confirmed by Wang et al. (1989), who studied both the ^{27}Al(^{3}He,t)^{27}Si and ^{28}Si(^{3}He,α)^{27}Si reactions [Wan89]. Vogelaar (1989), in a direct study of this reaction with a ^{26}Al target, observed 14 states from E_R^{CM} = 188 – 900 keV (E_x = 7.65 – 8.36 MeV) in an excitation function, and also obtained strengths for these [Vog89]. They also measured the ^{26g}Al(^{3}He,d)^{27}Si reaction in an attempt to extract Γ_p for the states at E_x = 7.592, 7.652, and 7.741 MeV via DWBA analysis [Vog96]. Lewis (2005) observed 37 states between E_x = 7.83 and 9.52 MeV in a study of the ^{27}Al(^{3}He,t)^{27}Si reaction. She also observed proton decays from ^{27}Si excited states to the ground, E_x = 228 keV and E_x = 416 keV states of ^{26}Al and so was able to extract the corresponding branching ratios Γ_p/Γ.

Using the available experimental information, as well as shell-model calculations [Cha93] for those low energy resonances without measured strengths, the rate of the ^{26g}Al(p,γ)^{27}Si reaction has been calculated [Cha93, Coc95, Ang99]. This rate is thought to be uncertain by as much as 2 orders of magnitude at nova temperatures [Ang99] largely because of uncertainty as to what strength to use for the E_R^{CM} = 188 keV (E_x = 7.651 MeV) resonance (uncertainties on the lower-lying resonances have significantly less influence [Coc95, Jos99, Ili02]). The single measurement of this strength came from

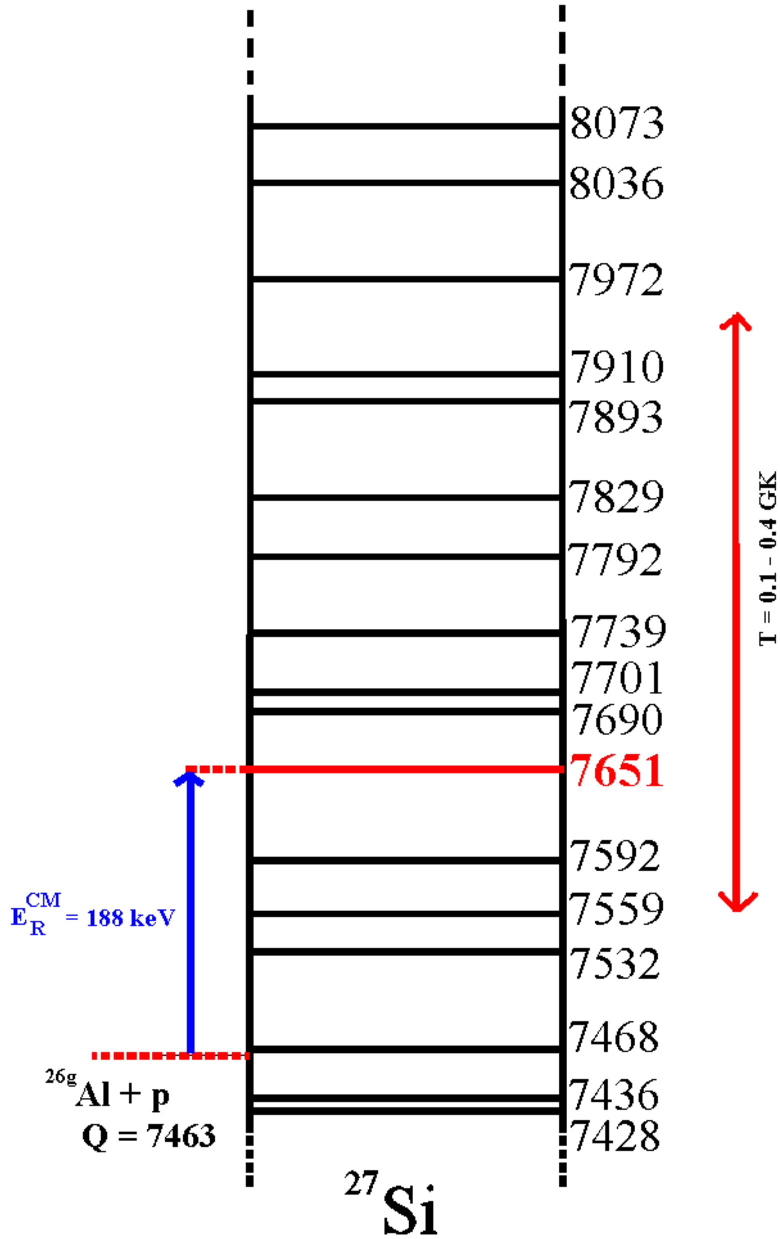

Figure 11: The level structure of ^{27}Si above the ^{26g}Al + p threshold. The energy region of importance at nova temperatures is indicated (see eq. (5)). The Q-value of the ^{26g}Al(p,γ)^{27}Si reaction is from [Aud03], and the excitation energies are weighted averages of the results from [Buc84], [Sch86], [Wan89], [Vog89], and [Lew05].

Table III: summary of known experimental information relevant for the $^{26g}Al(p,\gamma)^{27}Si$ reaction rate in ONeMg novae. The excitation energy region in ^{27}Si is listed in MeV from the $^{26g}Al + p$ threshold [Aud03] at $E_x = 7.463$ MeV to $E_x = 8.0$ MeV. The resonance strengths are in meV. Resonance energies in [Buc84] and [Vog89] have been converted from E_p to E_x using masses from [Aud03].

	[Buc84]		[Sch86]	[Wan89]	[Vog89]		[Vog96]		[Lew05]	
E_R^{CM} (keV)	E_x ; J^π	$\omega\gamma$	E_x	E_x	E_x	$\omega\gamma$	E_x	$\omega\gamma$ [b]	E_x ; J^π	Γ_p/Γ (%)
5			7.465(5)	7.470(4)						
69			7.530(5)	7.533(3)		$<2\times10^{-10}$				
96			(7.563)	(7.557(3))		$<2\times10^{-7}$				
129			7.596(4)	7.589(3)		$<2\times10^{-5}$	7.592	$<6 \times 10^{-6}$		
188			7.654(5)	7.651(3)	7.651(1)	0.042(7) [a]	7.652	<0.29		
227				(7.690(3))		<0.008 [a]				
238			7.703(3)	7.702(3)	7.700(1)	0.008(4) [a]				
276	7.7389(9) $(7/2\text{-}11/2)^+$	3.8(10)	7.742(3)	7.741(3)	7.7387(6)	2.3(3) [a]	7.741	<19		
303			(7.766)							
329			7.796(4)	7.789(3)						
366	7.825(3) $(7/2\text{-}11/2)^+$	65(18)	7.837(4)	7.832(3)	7.8292(6)	61(7) [a]			7.830(4) $(9/2,11/2)^+$	18(12)
407			(7.870)							
430				7.893(4)						
447			7.909(4)	7.913(3)					7.907(4)	
510			7.974(5)	7.971(3)					7.973(8)	

[a] These strengths have been renormalized from the values reported in [Vog89]. See Chapter IV, C, viii.
[b] Upper limits based on l = 0 transfer in DWBA analysis.

the PhD studies of Vogelaar (1989), who found $\omega\gamma = 55 \pm 9$ μeV. However, because most of Vogelaar's results were not published, there is disagreement in the literature as to whether or not to use the results. For example, the reaction rate compilation of [Ang99] instead adopts lower and upper limits (9.9×10^{-3} and 290 μeV, respectively) based on the published (^{3}He,d) work of Vogelaar [Vog96]. The effect of uncertainty in this strength on the ^{26}Al yield of novae is seen in the nucleosynthesis model calculations of [Jos99]: scaling the Vogelaar (1989) measurement of the strength ($\omega\gamma = 55 \pm 9$ μeV) by even 1/3 leads to an increase by a factor of ~2 in the ^{26}Al yield. (Note that Vogelaar (1989) states that some of his results –including the strength of the E_R^{CM} = 188 keV resonance– were normalized to the strength of a resonance in ^{27}Al(p,γ)^{28}Si. Since this latter strength has changed, we have appropriately renormalized his affected results. See table III and Chapter IV, C, viii.)

Given the sensitivity of the ^{26}Al nova yield to this resonance strength, along with the fact that there has only been one measurement [Vog89], we have re-measured the strength of the (nominally) E_R^{CM} = 188 keV resonance in ^{27}Si. In Chapter IV (see also [Rui06]), we describe the results of our direct study with a ^{26g}Al beam, using the thick-target yield method to obtain the resonance strength.

III. THE MASS OF ^{26}Si

We have measured the ^{26}Si mass for three reasons:

1. A direct study of the ^{25}Al(p,γ)^{26}Si reaction has not yet been made; the energy regions to be examined in the future study [Che01] will depend upon the excitation energies of states in ^{26}Si found through indirect experiments, as well as the Q-value of the reaction (and so the masses of ^{25}Al, p, and ^{26}Si).
2. In the absence of results from a direct study, current calculations of the ^{25}Al(p,γ)^{26}Si rate depend exponentially upon the masses of the involved nuclei.
3. The current recommended mass of ^{26}Si is based upon only one measurement [Har74, Aud03], and is uncertain by ± 3 keV.

Given the importance of the ^{25}Al(p,γ)^{26}Si rate in calculations of the ^{26}Al yield from ONeMg novae (see Chapter I, C), a new examination of the ^{26}Si mass was warranted.

A. **Technique**

A 33 MeV proton beam was accelerated by the tandem at Yale University's A.W. Wright Nuclear Structure Laboratory (WNSL) and then used to bombard a natural SiO target. Reaction products were momentum-analyzed in an Enge split-pole spectrograph [Spe67]. Using a position-sensitive gas-filled ionization drift chamber at the focal plane of the spectrograph (calibrated with (p,t) and (p,d) reactions during the experimental run), we determined the momenta of tritons corresponding to the ground state of ^{26}Si from the ^{28}Si(p,t)^{26}Si reaction. On the basis of the well-known masses of ^{28}Si, p and t, the mass of ^{26}Si could then be calculated through [Kra88]

$$\begin{aligned} Q_0 &= m_{28} + m_p - m_{26} - m_t \\ &= E_t\left(1 + \frac{m_t}{m_{26}}\right) - E_p\left(1 - \frac{m_p}{m_{26}}\right) - 2\sqrt{\left(\frac{m_p m_t}{m_{26}^2} E_p E_t\right)}\cos\theta, \end{aligned} \tag{6}$$

where θ is the scattering angle; m_t, m_p, m_{26}, m_{28} are the masses of the triton, proton, ^{26}Si, ^{28}Si respectively; E_p, E_t are the energies of the proton beam and the triton; and Q_0 is the ground state Q-value of the ^{28}Si(p,t)^{26}Si reaction.

For technical reasons (see section B) as well as to reduce systematic error from uncertainty in E_p and θ, we measured the Q_0 of the ^{28}Si(p,t)^{26}Si reaction relative to the Q_0 of the ^{16}O(p,t)^{14}O reaction. To provide confidence in the method, we also determined the mass of ^{22}Mg using the same technique and compared that result with two recent high-precision Penning trap measurements of this mass [Sav04, Muk04] (see section D). (As discussed in Chapter II, C, the mass of ^{22}Mg was an issue in the interpretation of the results from a study of the ^{21}Na(p,γ)^{22}Mg reaction [Bis03a, Bis03b].)

B. **Experimental Setup**

i. Beam and Targets

Figure 12 shows the layout of WNSL. In the ion source, TiH_2 powder was sputtered with Cs ions to produce H- ions. These were then accelerated to the +16.5 MV tandem terminal, fully stripped of electrons by a carbon foil, and further accelerated back to ground potential. The energy of the now-H+ beam was 16.5 MV**e* + 16.5 MV**e* = 33 MeV, where *e* is the electron charge.

An analyzing magnet with field *B* follows the accelerator, bending the beam of charge *q*, mass *m* and energy *E* through a central bending radius ρ = 1.79 m according to

$$\rho = \frac{p}{qB} = \frac{\sqrt{2mE}}{qB}, \tag{7}$$

and through a ± 0.5 mm aperture. This ensures both the energy and purity of the beam; the former has been calibrated using the well-known ^{12}C + p elastic scattering resonance at E_p = 14.231 MeV [Ove69] and is thought to be accurate to ~10^{-4}. The energy spread of the beam was ΔE ~ 10 keV, and we ran at currents of about 20 nA.

The proton beam energy was decided upon by considering the thresholds for the ^{28}Si(p,t)^{26}Si$_{g.s.}$ and ^{24}Mg(p,t)^{22}Mg$_{g.s.}$ reactions (E_p > 22 MeV) as well as the kinematics necessary for desired relative positions of triton groups from the ^{28}Si(p,t), ^{22}Mg(p,t), ^{12}C(p,t) and ^{16}O(p,t) reactions. With regard to the latter, we arranged for the

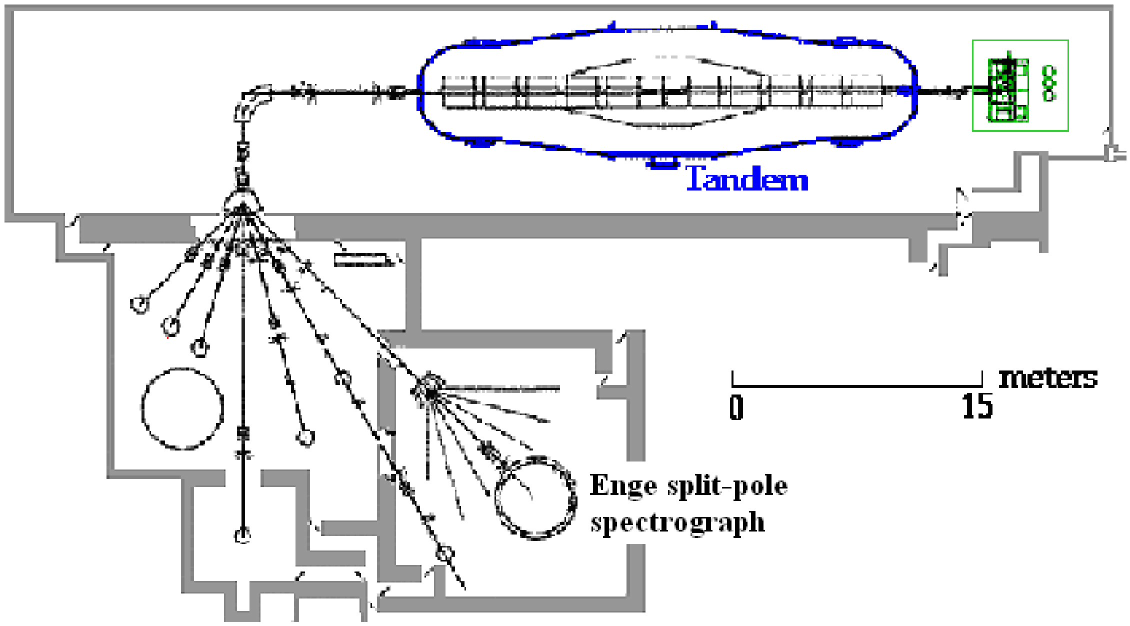

Figure 12: Layout of the Wright Nuclear Structure Laboratory at Yale University.

$^{16}O(p,t)^{14}O_{g.s.}$ triton group to be ‘close’ in momentum to the triton groups corresponding to the ground states of ^{26}Si and ^{22}Mg to allow as localized a calibration as possible of our focal plane detector for this relative measurement. Major contaminant triton groups flanking the desired triton groups provide a quick consistency check of the focal plane calibration, and having the triton groups corresponding to first excited states of ^{22}Mg and ^{26}Si on the focal plane allows a secondary determination of the masses. An optimal configuration of triton groups was found for E_p = 33 MeV. This energy also allowed a reasonable focal plane calibration with the $^{25}Mg(p,d)^{24}Mg$ and $^{27}Al(p,d)^{26}Al$ reactions – see figs. 13 and 14.

For out (p,t) measurements, we used a 65 $\mu g/cm^2$ natural SiO target with a gold flash and a 67 $\mu g/cm^2$ ^{24}MgO target on a 15 $\mu g/cm^2$ natural carbon backing. These thicknesses were determined to 10% through measurements with an alpha source.

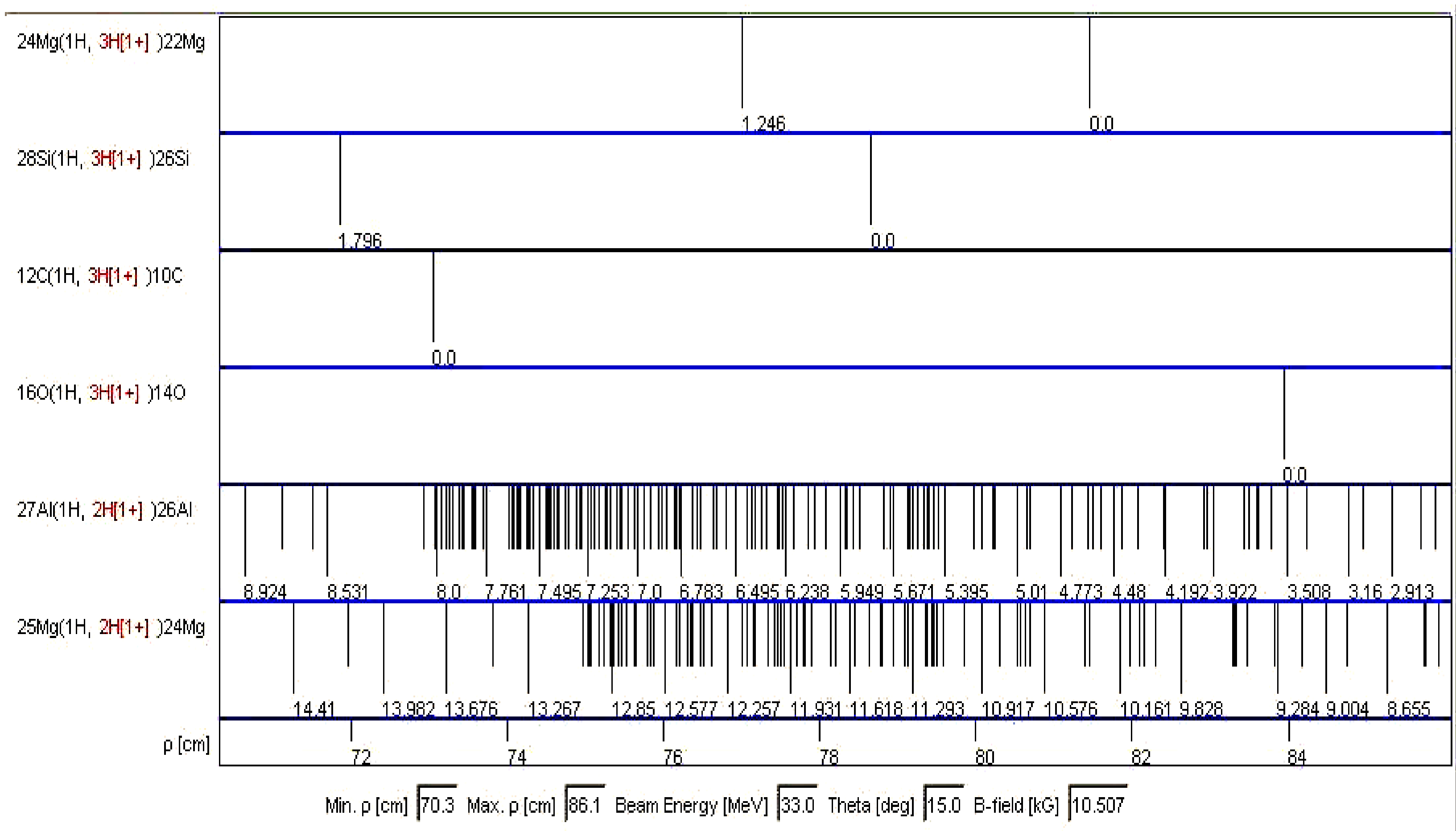

Figure 13: The expected positions of tritons from the $^{24}Mg(p,t)^{22}Mg$, $^{28}Si(p,t)^{26}Si$, $^{12}C(p,t)^{10}C$ and $^{16}O(p,t)^{14}O$ reactions and deuterons from the $^{25}Mg(p,d)^{24}Mg$ and $^{27}Al(p,d)^{26}Al$ reactions for $B = 10.507$ kG, $\theta_{lab} = 15^{\circ}$ and $E_p = 33$ MeV.

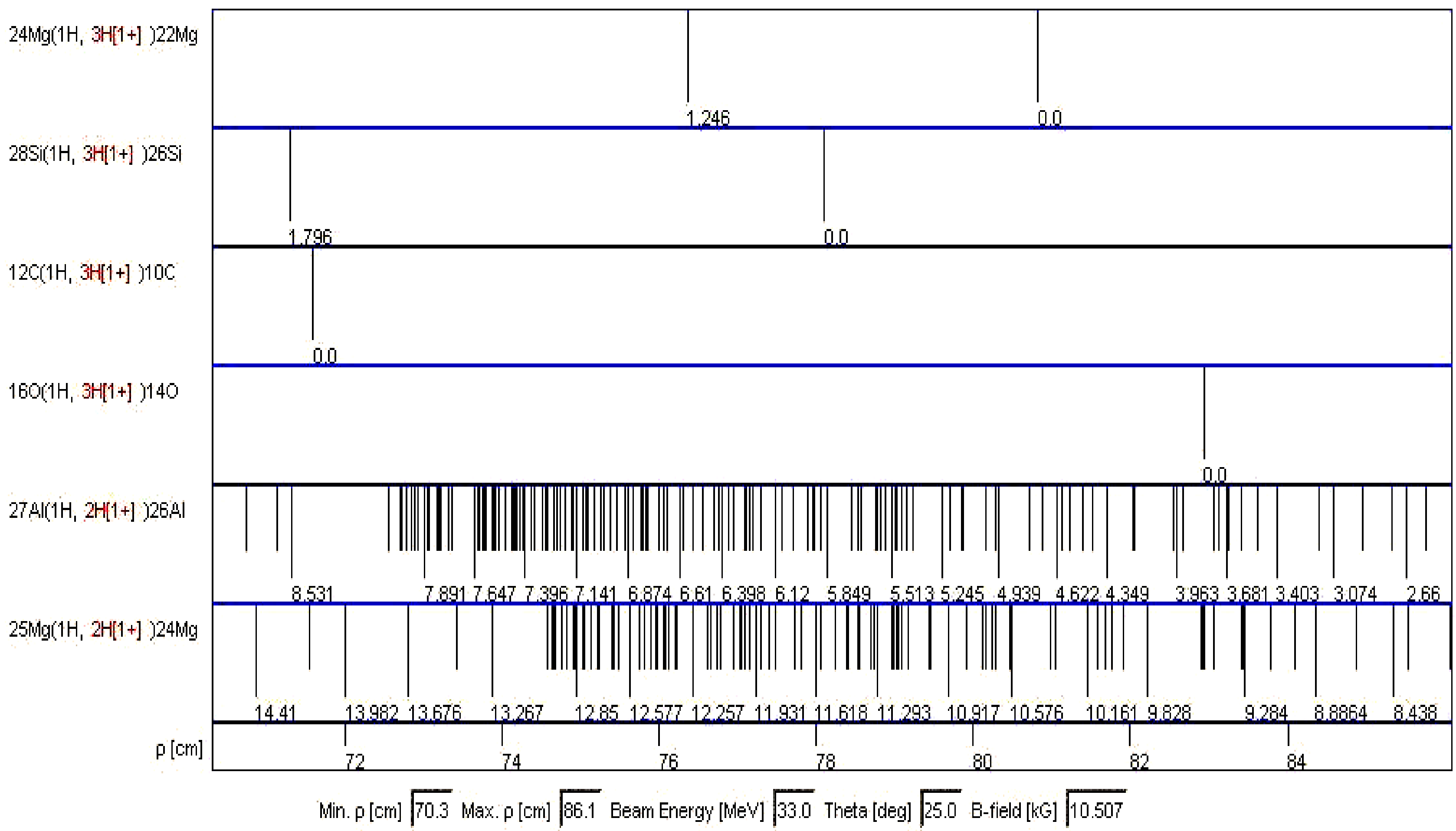

Figure 14: The expected positions of tritons from the $^{24}Mg(p,t)^{22}Mg$, $^{28}Si(p,t)^{26}Si$, $^{12}C(p,t)^{10}C$ and $^{16}O(p,t)^{14}O$ reactions and deuterons from the $^{25}Mg(p,d)^{24}Mg$ and $^{27}Al(p,d)^{26}Al$ reactions for B = 10.507 kG, $\theta_{lab} = 25^{\circ}$ and $E_p = 33$ MeV.

In addition, we used a 360 $\mu g / cm^2$ enriched ^{25}MgO target and a 140 $\mu g / cm^2$ Al target for momentum calibration of the focal plane with the ^{25}Mg(p,d)^{24}Mg and ^{27}Al(p,d) ^{26}Al reactions. We note that both (p,t) measurements (along with the (p,d) measurements) were made in the same experimental run, with unchanged beam energy, scattering angle (for each of the two angles employed) and magnetic field of the spectrograph. Hence, the same momentum calibration could be used to determine the Q_0 value of both the ^{28}Si(p,t)^{26}Si and ^{24}Mg(p,t)^{22}Mg reactions.

ii. Enge Split-Pole Spectrograph

Figure 15 shows the Enge split-pole spectrograph, which disperses reaction products according to their momenta (eq. (7)) for detection at its focal plane. As designed by Enge [Spe67], this instrument has two sets of pole pieces ("split-pole") surrounded by a single coil. The location of the pieces within the coil and their shaping are chosen to accomplish approximate vertical focusing over a wide range of momentum while maintaining good horizontal focusing up to second-order (i.e. x/θ^2 and $x/\varphi^2 \sim 0$, where θ and φ refer to angles in the plane of and normal to the plane of the particle trajectory in the spectrograph, respectively); the design allows for good collecting power without sacrificing resolution [Spe67]. (Third-order aberrations x/θ^3 remain, but can be corrected for by measuring the angle of particles exiting the spectrograph: see e.g. [Lew05].) The spectrograph can accept all reaction products with momenta satisfying 51.1 cm < ρ < 92.0 cm (see eq. (7)).

The maximum solid angle acceptance of the spectrograph is about 12.8 msr (± 80 mrad horizontal and ± 40 mrad vertical). For our experiment, we desired good energy resolution and rate was not an issue (the entire measurement was easily completed in a week), so we chose $\Delta\theta = \pm 10$ mrad and $\Delta\varphi = \pm 40$ mrad for a nominal solid angle

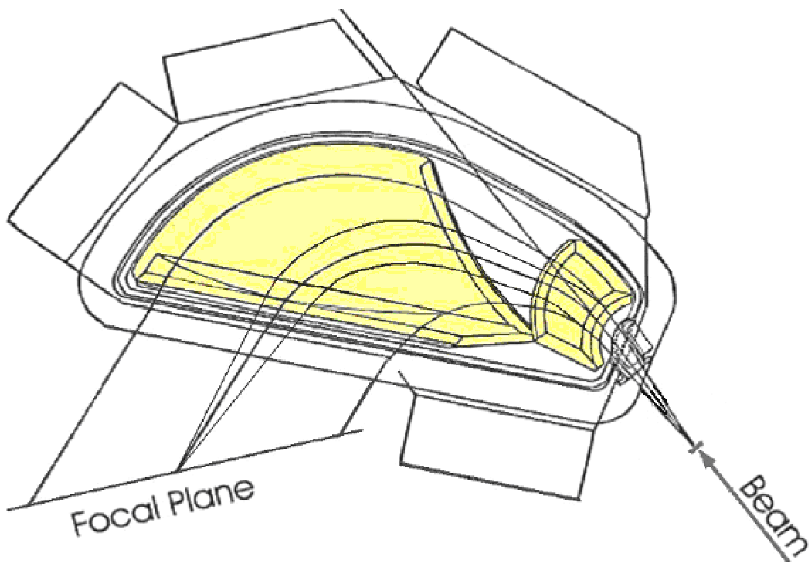

Figure 15: diagram of the Enge split-pole spectrograph. Trajectories of particles emerging from the target at different angles and with different energies are shown.

acceptance of 1.6 msr. The magnifications of the beam spot in the horizontal and vertical directions are 0.39 and 2.9, respectively. This spot is minimized by tuning through a 2 mm diameter collimator at the target position into a Faraday cup.

The $^{28}Si(p,t)$ and $^{24}Mg(p,t)$ reactions (as well as the (p,d) calibration reactions) were measured at $\theta_{lab} = 15^\circ$ and 25°, with $B = 10.507$ kG. The scattering angles are fixed by rotating the spectrograph relative to the incoming proton beam and can be set to ~0.1˚.

These B and θ settings were chosen in concert with the beam energy – see the discussion above and figs. 13 and 14.

iii. Focal Plane Detection System

A position-sensitive ionization drift chamber (PIDC) was set at the focal plane of the spectrograph, covering a momentum range of about $70 < \rho < 86$ cm (where ρ is the radius of curvature of each particle's trajectory in the magnetic field of the spectrograph). This detector measures both the position of particle groups along the focal plane and the energy loss ΔE of these particles as they drift across a cathode. A plastic scintillator measures the residual energy E of particles that exit the PIDC. With these measurements of ρ, ΔE and E, the identity of reaction products can be determined quite effectively (see section C).

Figure 16 shows a picture and schematics of the PIDC. The description of the PIDC given here is a summarized and updated version of that presented in [Rou04]. The chamber is a milled-out block of aluminum, 26″x 8.5″x 3″ in length, height and depth. Reaction products bent by the spectrograph enter and exit the detector through 0.25 mil aluminized mylar windows attached to window plates. The volume of the detector is filled with isobutane through gas ports installed in the sides of the chamber. The cathode plate is held at large negative potential, the Frisch grid is grounded, and the three high-voltage wires of each position-sensitive assembly (PSA) are held at large positive

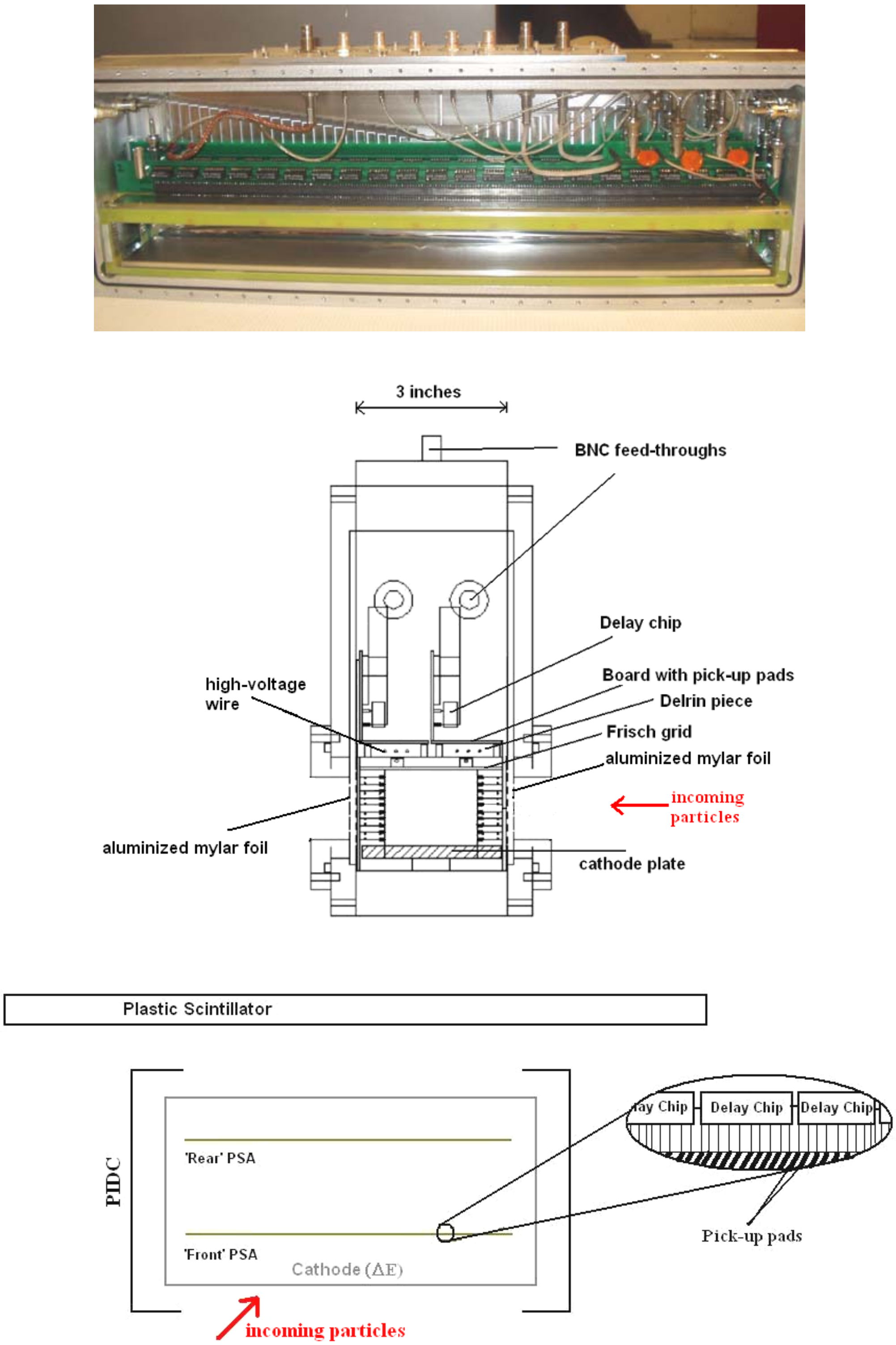

Figure 16: (top) front-view of the interior of the position-sensitive ionization drift chamber. Particles enter the detector into the page. (middle) schematic side-view of the PIDC, to scale. The wires of the field-shaping cage have been removed for clarity. (bottom) simplified schematic top-view of the focal plane detection system (not to scale).

potential. For this experiment, we used 150 torr of isobutane and typical settings for the high-voltage wires and cathode of +1700 V and –700 V, respectively.

The signal from the cathode arises from the drift of electron-ion pairs created as reaction products traverse the detector volume between the Frisch grid and cathode plate [Kno79]. A uniform electric field is produced in this drift region through the use of 10 equally spaced wires surrounding this volume and connected to the cathode and Frisch grid through a resistor chain (each of 10 MΩ). These field-shaping wires (1 mil gold-plated tungsten) run along a rectangular cage composed of frames of G-10 plastic (see fig. 17). The Frisch grid is a frame of G-10 plastic with 1 mil gold-plated tungsten wires (painstakingly) soldered along its long axis to a density of ~10 wires/cm. The cathode is a smooth, uniform 0.25″ thick plate of aluminum that forms the base of the field-shaping cage.

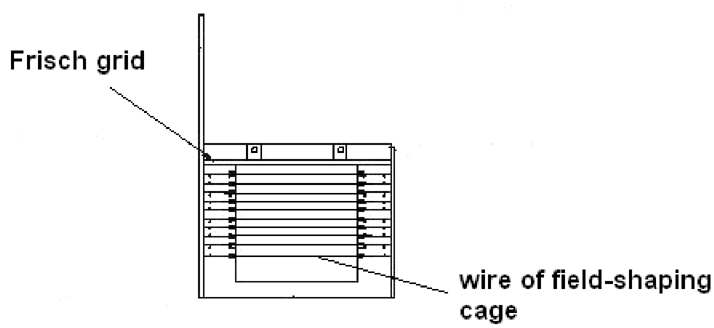

Figure 17: side-view schematic of the field-shaping cage surrounding the drift region in the PIDC. The PSAs sit atop this cage, which in turn, sits atop the cathode plate.

The position of particle groups along the length of the PIDC is found through the delay-line method. Each of the two identical PSAs (see fig. 18) consists of two circuit boards. The board in the plane of the cathode plate has 220 lead-coated copper pick-up pads tilted at 45° on its underside (so that the pads lie along the direction of reaction products). Each pad is 0.09″ wide, 1.4″ long, and separated from its neighbor by 0.01″. Delrin pieces are attached to the undersides of these boards at either end of each PSA; three 'high-voltage' wires (1 mil gold-plated tungsten, separated by 0.25″) are threaded through these pieces, for each assembly. The other board (in the plane parallel to the windows) holds the delay chips. Each assembly has twenty-two 50 ns delay chips (10 taps each, 5 ns/tap, Allen Avionics #LC050Z050B) that are connected to the pick-up pads. The true delays of these chips have been measured to lie between 63 - 65 ns for the chips in the upstream (or 'front') PSA, and 60 - 62 ns for the downstream (or 'rear') PSA.

Electrons drift away from the cathode, through the Frisch grid, and toward the high-voltage wires, where they cause an electron avalanche. The signal from those pick-up pads nearest to the avalanche travels to both ends of the PSAs through the delay lines. The relative delay between the signals from either end of a delay line can then be used with a time-to-amplitude converter (TAC) to deduce the 'front' and 'rear' positions of the reaction products passing through the detector.

The position of the PIDC was set so that the middle wire of the front PSA lay along the focal plane of the spectrograph. Since the momenta of reaction products will depend on their angle of emission from the target -and we use a finite horizontal angular acceptance-

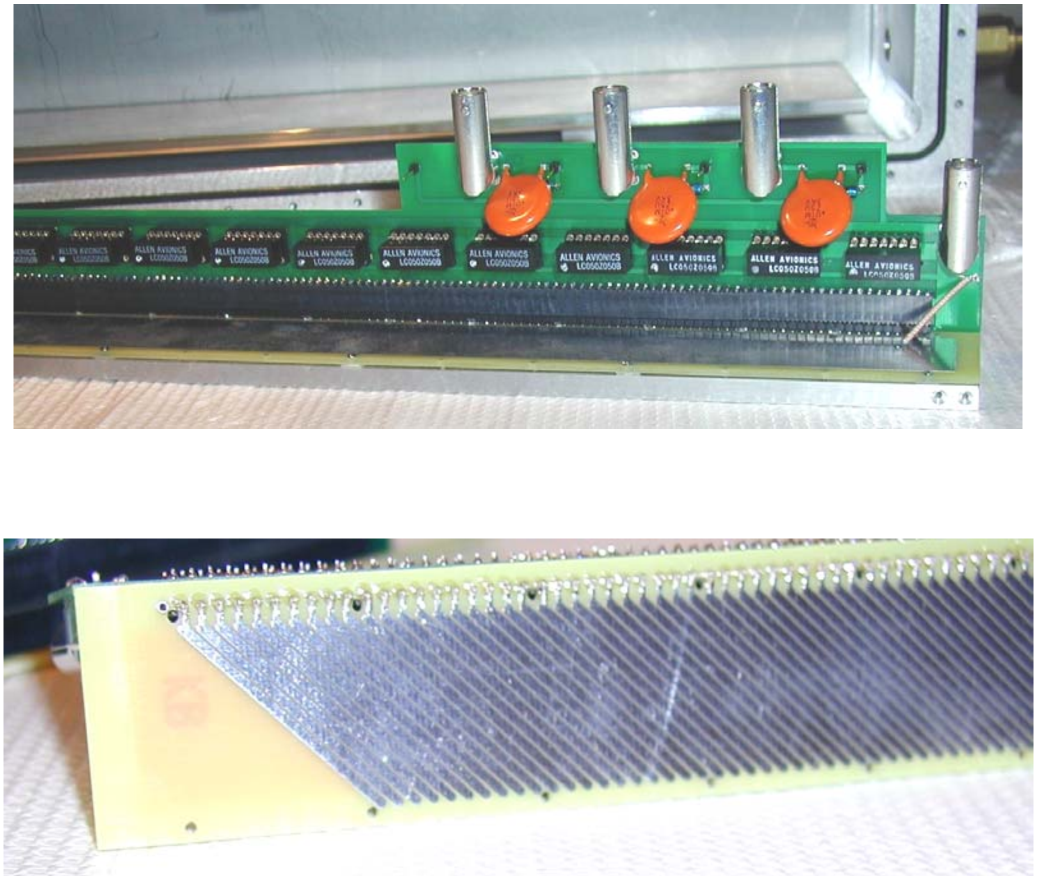

Figure 18: (top) front-view of one of the two position-sensitive assemblies within the PIDC. (bottom) the pick-up pads on the undersides of the PSAs.

the focal plane position effectively shifts for different reactions. Left uncorrected, this kinematic broadening leads to a loss in resolution. To avoid this effect, we measured the 'front' resolution of alpha particles corresponding to the ground states of ^{22}Na and ^{10}B (via the $^{25}Mg(p,\alpha)$ and $^{13}C(p,\alpha)$ reactions, respectively) as a function of the detector position *z*.

We thereby found the dependence of the ideal detector position *z* (in cm) on the kinematic parameter $k \equiv \frac{-1}{p}\frac{dp}{d\theta}$ as prescribed in [Eng79]:

$$z = 56.7k + 55.5. \tag{8}$$

The detector position *z* can be adjusted with an external motorized assembly.

Immediately downstream of the exit window of the PIDC is a plastic scintillator (BC-404, 6.35 mm thick) within which reaction products that pass through the PIDC give a residual energy signal *E*. Light is collected by photomultiplier tubes (PMTs) at each end of the scintillator, and these two signals E_1, E_2 are combined (in software) according to $E = \sqrt{E_1 E_2}$ [Kno79].

iv. Signal Processing

Figure 19 shows a block-diagram of the (NIM-standard) electronics used to process signals from the PIDC (cathode, delay-line signals from the two ends of the front and rear

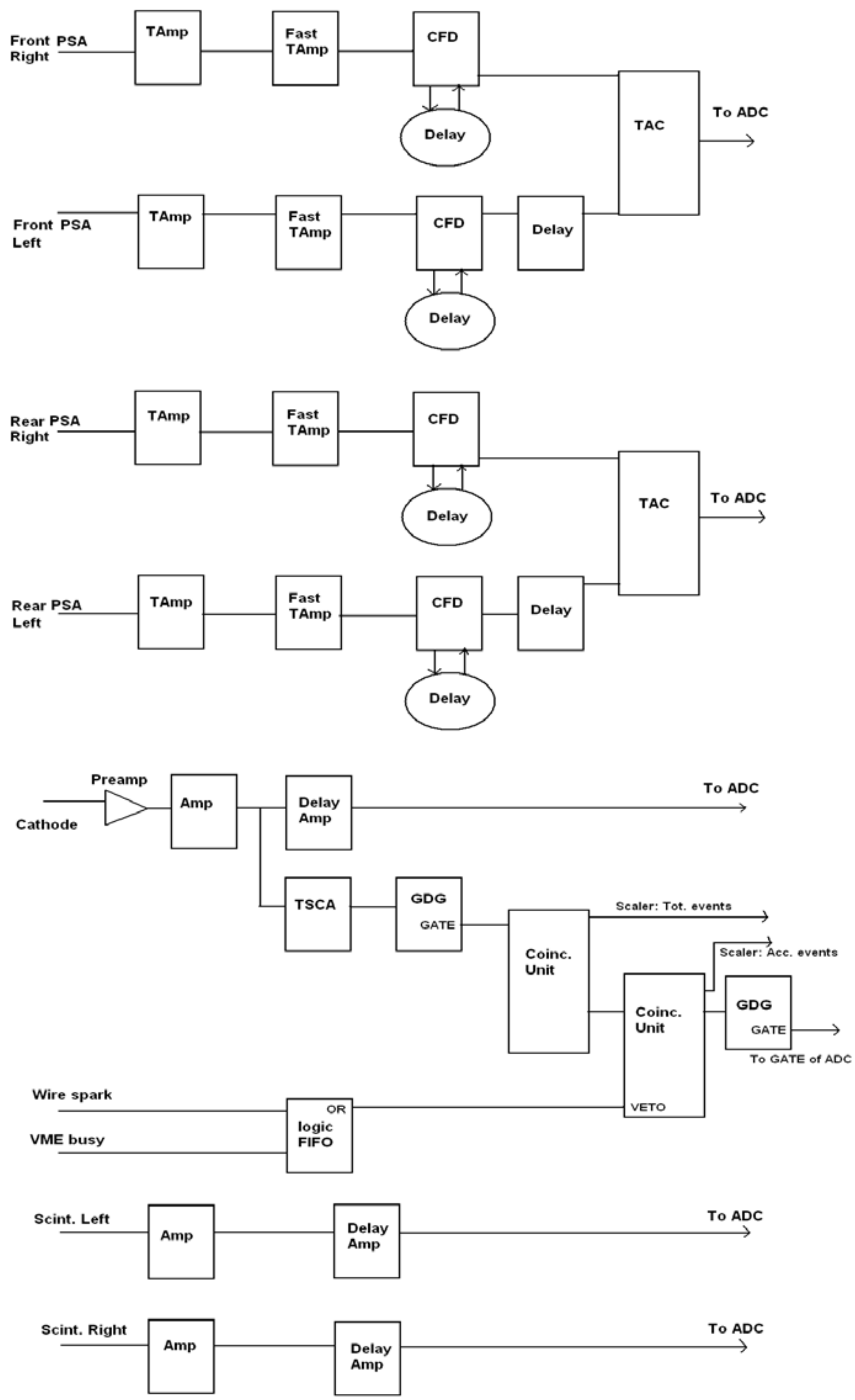

Figure 19: the electronics used in the ^{22}Mg and ^{26}Si mass measurements. Abbreviations: Amp = amplifier, ADC = analog-to-digital converter, FIFO = fan-in/fan-out, GDG = gate-and-delay generator, TAmp = timing amplifier, Preamp = pre-amplifier, CFD = constant-fraction discriminator, TAC = time-to-amplitude converter, PSA = position-sensitive assembly, TSCA = Timing single-channel-analyzer

PSAs) and the scintillator (from the two PMTs at either end). The ADC is a 32-channel VME-6U module (CAEN V785). The cathode signal provided the trigger for our events; we did not require cathode-scintillator coincidences. The various signals in the ADC channels were delayed such that they fell within the gate begun by the cathode signal. A scaler module in the VME crate (16 channels, CAEN V260N) was fed signals to count cathode and scintillator trigger rates, the beam current, total and accepted events (as dictated by the BUSY of the VME computer and/or sparking of the high-voltage wires), and time.

v. Data Acquisition

Data from the ADC buffer is stored in an 8 kB memory buffer on a computer running the Vx-Works operating system. A private Ethernet connects this computer to a PC, and data is shipped between these computers when the memory buffer is filled. The PC runs a Java-based acquisition and display package known as Jam which stores the online event data to a hard drive [JAM, Swa01]. Both online and offline, Jam provides a simple graphical user interface for sorting multi-parameter event-based data into 1-D and 2-D histograms. The sorting method relies on gates drawn by the experimenter to select particle groups of interest; based on these gates, other histograms can then be filled. All histogram and gate information for a particular run can be saved to a file separate from that with the raw data. Jam also interacts with the VME computer to retrieve scaler information during runs, and this information can also be saved.

C. **Results and Analysis**

i. Particle Identification

Protons, deuterons, tritons and alpha particles were all present in our raw data. These groups were separated from each other by drawing 2-D gates in Jam using information from the focal plane detection system: the position of particles along the wire at the focal plane (Front Position), the energy loss of particles as they drifted across the cathode (Cathode), and the residual energy deposited in the scintillator by particles (Scintillator). Applying these gates, a Front Position histogram was filled for each type of particle.

We illustrate this process here for tritons from the (p,t) reaction on the ^{24}MgO+C target at $\theta_{lab} = 15^{\circ}$. Figure 20 shows raw data in a Scintillator vs. Front Position spectrum. Bands corresponding to different particle groups are labeled, and a gate has been drawn around the triton band. We then move to the Cathode vs. Scintillator and Cathode vs. Front Position spectra in figs. 21 and 22, respectively. These figures show both the raw data and the spectra as they look with the application of the Scintillator vs. Front Position gate of fig. 20. With the application of further gates around the tritons in the spectra of figs. 21 and 22, we produce the clean triton Front Position spectrum of fig. 23. The energy resolution, determined using the ^{22}Mg ground-state peak, is 10 keV full width at half-maximum (in both E_t and E_x). (Note that the detector position z had been correctly set for both mass measurements - see eq. (8).)

Using similar methods, we produced Front Position spectra at both θ_{lab} = 15˚ and 25˚ for tritons from the (p,t) reaction on the SiO target and deuterons from the (p,d) reactions on the ^{25}MgO and Al targets (to allow two *independent* calibrations of our focal plane). These are shown in figs. 23, 24, 25 and 26. Compare figs. 23 and 24 with figs. 13 and 14.

ii. <u>Focal Plane Calibration</u>

We used the deuteron spectra from the ^{27}Al(p,d)^{26}Al and ^{25}Mg(p,d)^{24}Mg reactions to perform two independent momentum calibrations of our focal plane, for each of the two scattering angles. Explicitly, polynomial functions of the position *x* along the focal plane were fit to the momenta (or equivalently the magnetic rigidities, $B\rho$) of those deuteron groups corresponding to states in ^{26}Al (2.5 < E_x < 7.3 MeV, with $\Delta E_x = 0.02 - 0.07$ keV [End90]) and states in ^{24}Mg (8.8 < E_x < 13.9 MeV, with $\Delta E_x = 0.08 - 3$ keV [End90]) – see figs. 25 and 26 respectively. Judging by the reduced X^2 parameter, we found that second-degree polynomials (in *x*) gave the best fit to each set of (p,d) data. Figure 27 gives an indication of how good the fits are to the data at 15°: we plot the residuals $\delta = (\rho_{\exp t} - \rho_{fit})$ divided by their 1σ error against the position *x*. This 1σ uncertainty had contributions from both the uncertainty in the excitation energy assigned to a calibration peak [End90] and the uncertainty introduced by the experimental widths of the calibration peaks, with the latter dominating. We see that for both calibrations at 15°, the residuals for the various deuteron groups lie mostly within $\pm 1\sigma$; this result was echoed for the two deuteron calibrations at 25°.

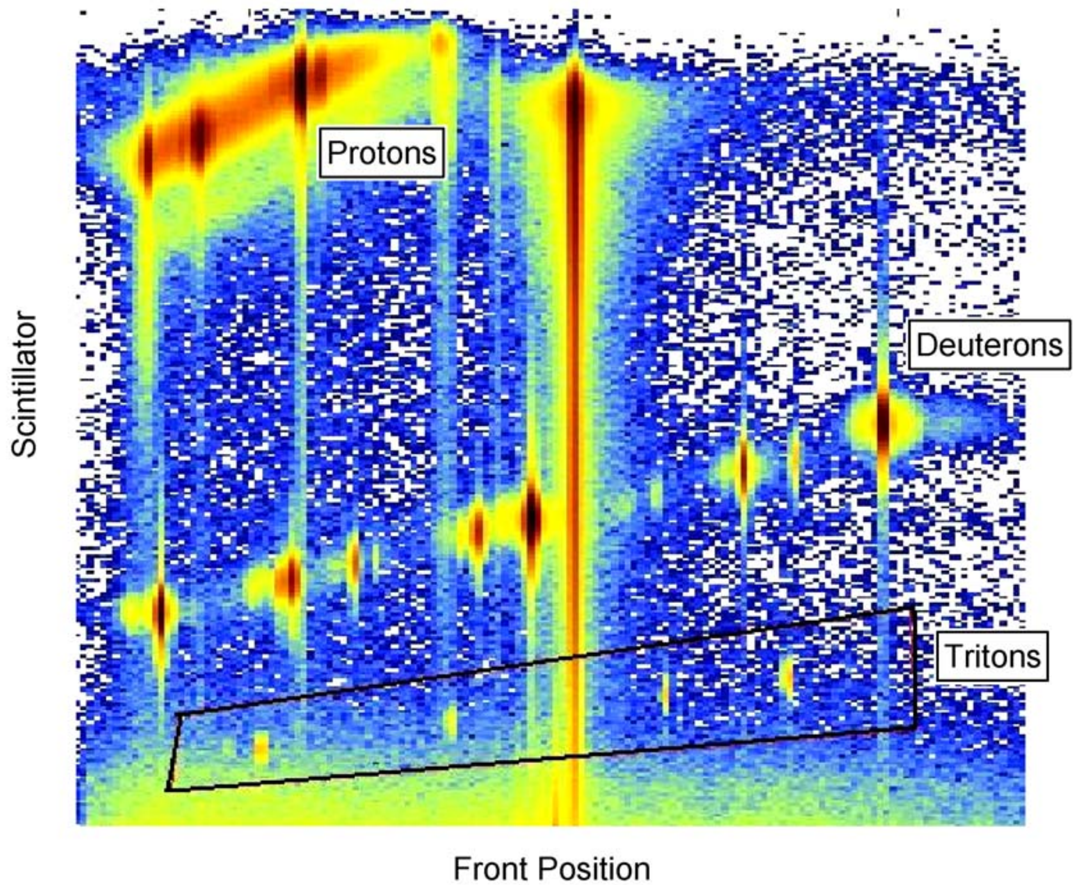

Figure 20: residual energy of particles in the scintillator vs. position along the front wire of the focal plane detector for light products of proton-induced reactions on the ^{24}MgO+C target at θ_{lab} = 15°. Bands corresponding to protons, deuterons and tritons are indicated, as well as the gate used around the triton band. (A group of alpha particles blends into the left side of the deuteron band.) The strong elastic proton groups from ^{12}C(p,p)^{12}C and ^{16}O(p,p)^{16}O overlap to saturate the scintillator signal near the centre of the focal plane.

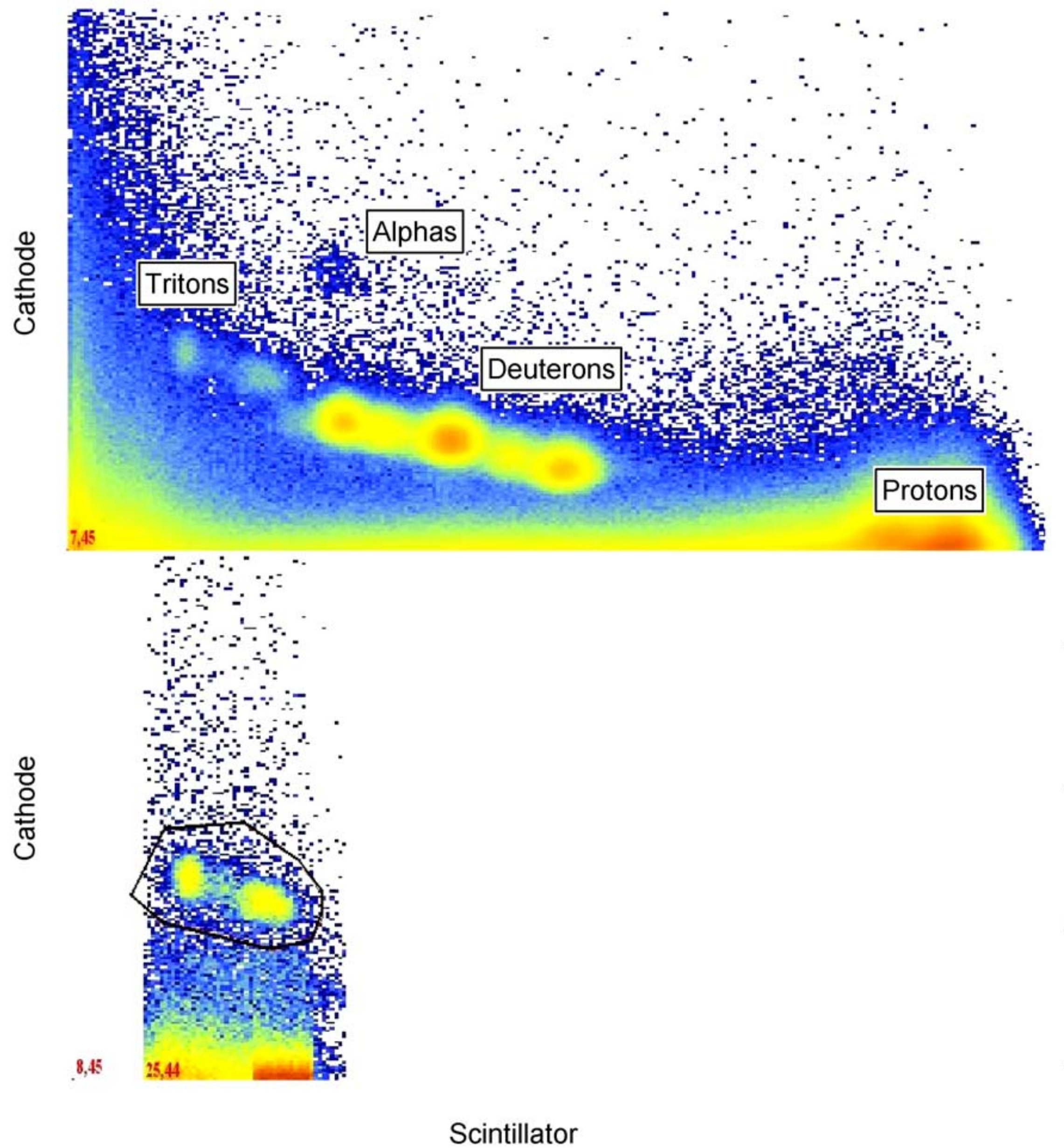

Figure 21: energy loss of particles in the cathode vs. residual energy in the scintillator for light products of proton-induced reactions on the ^{24}MgO+C target at θ_{lab} = 15˚. Groups corresponding to protons, deuterons, tritons and alphas are indicated. (top) raw data, with no gates applied. (bottom) the gate on the triton groups in the scintillator (fig. 20) is incorporated and a further gate to be applied on the triton groups in this spectrum is shown.

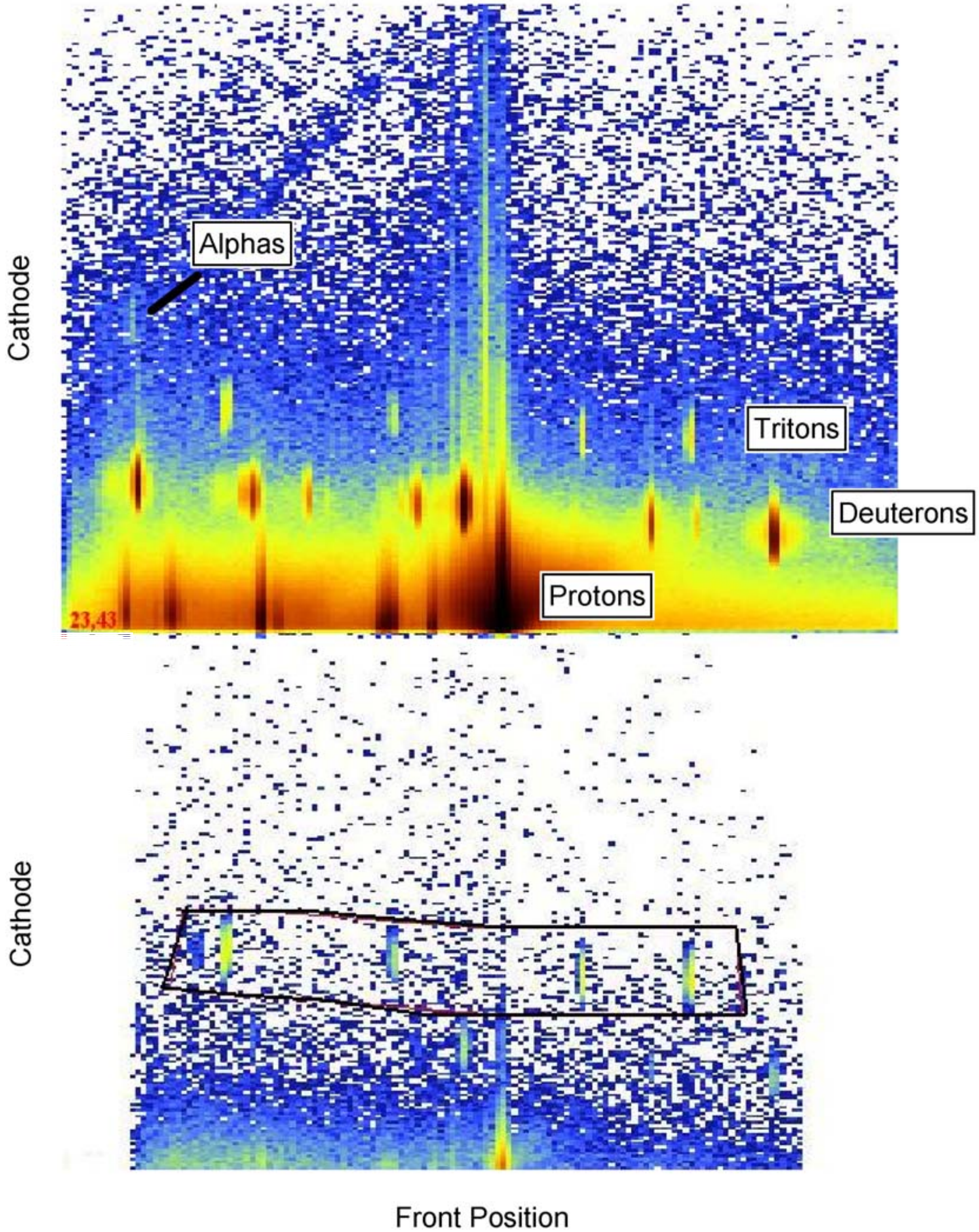

Figure 22: energy loss of particles in the cathode vs. position along the wire at the focal plane of the PIDC for light products of proton-induced reactions on the ^{24}MgO+C target at θ_{lab} = 15˚. Bands corresponding to protons, deuterons and tritons are indicated, as well as an alpha group. (top) raw data, with no gates applied. (bottom) the gate on the triton groups in the scintillator (fig. 20) is incorporated and a further gate to be applied on the triton groups in this spectrum is shown.

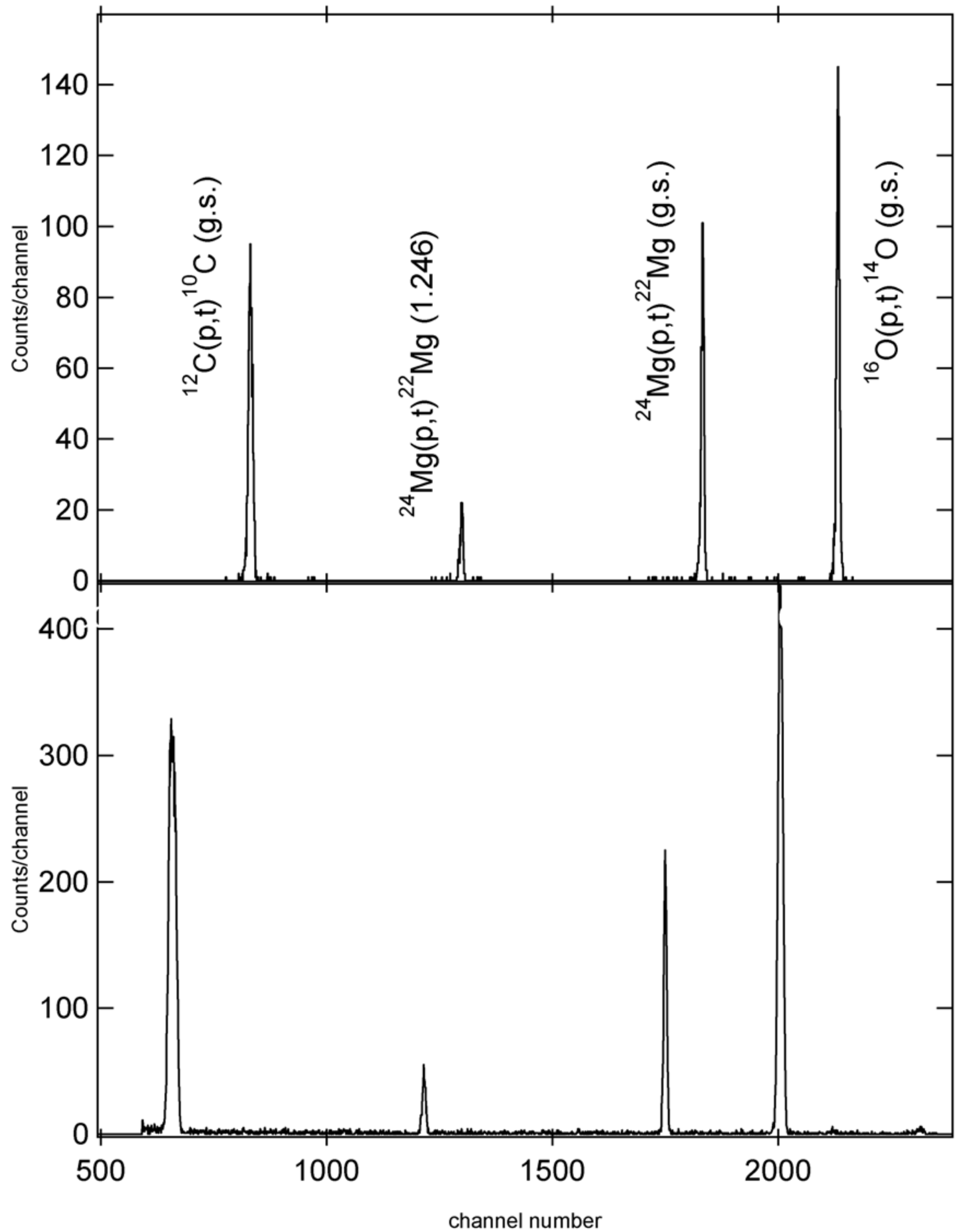

Figure 23: Triton momentum spectra from (p,t) reactions on the ^{24}MgO+C target at at (top) θ = 15° and (bottom) θ = 25°.

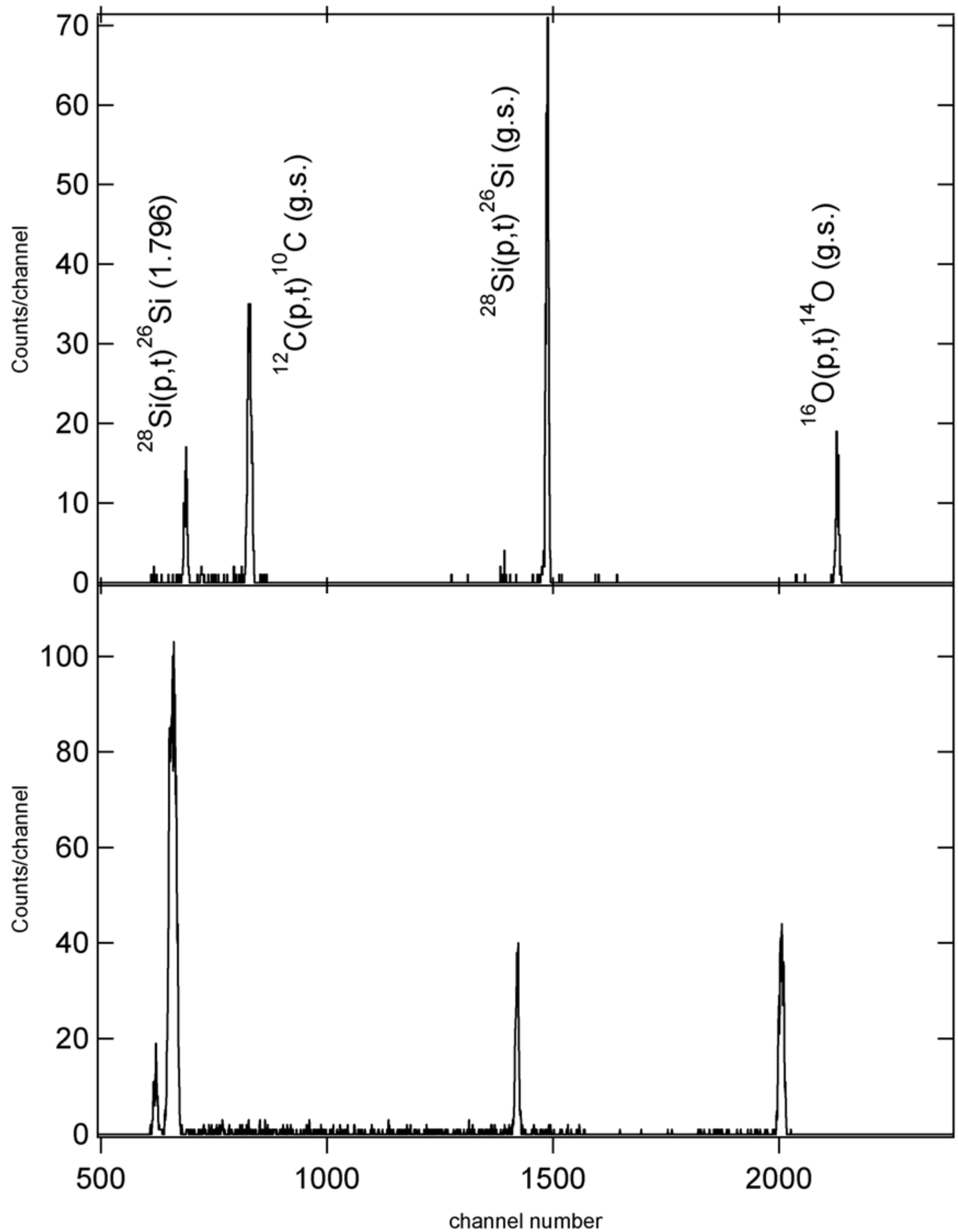

Figure 24: Triton momentum spectra from (p,t) reactions on the SiO target at at (top) $\theta = 15^\circ$ and (bottom) $\theta = 25^\circ$.

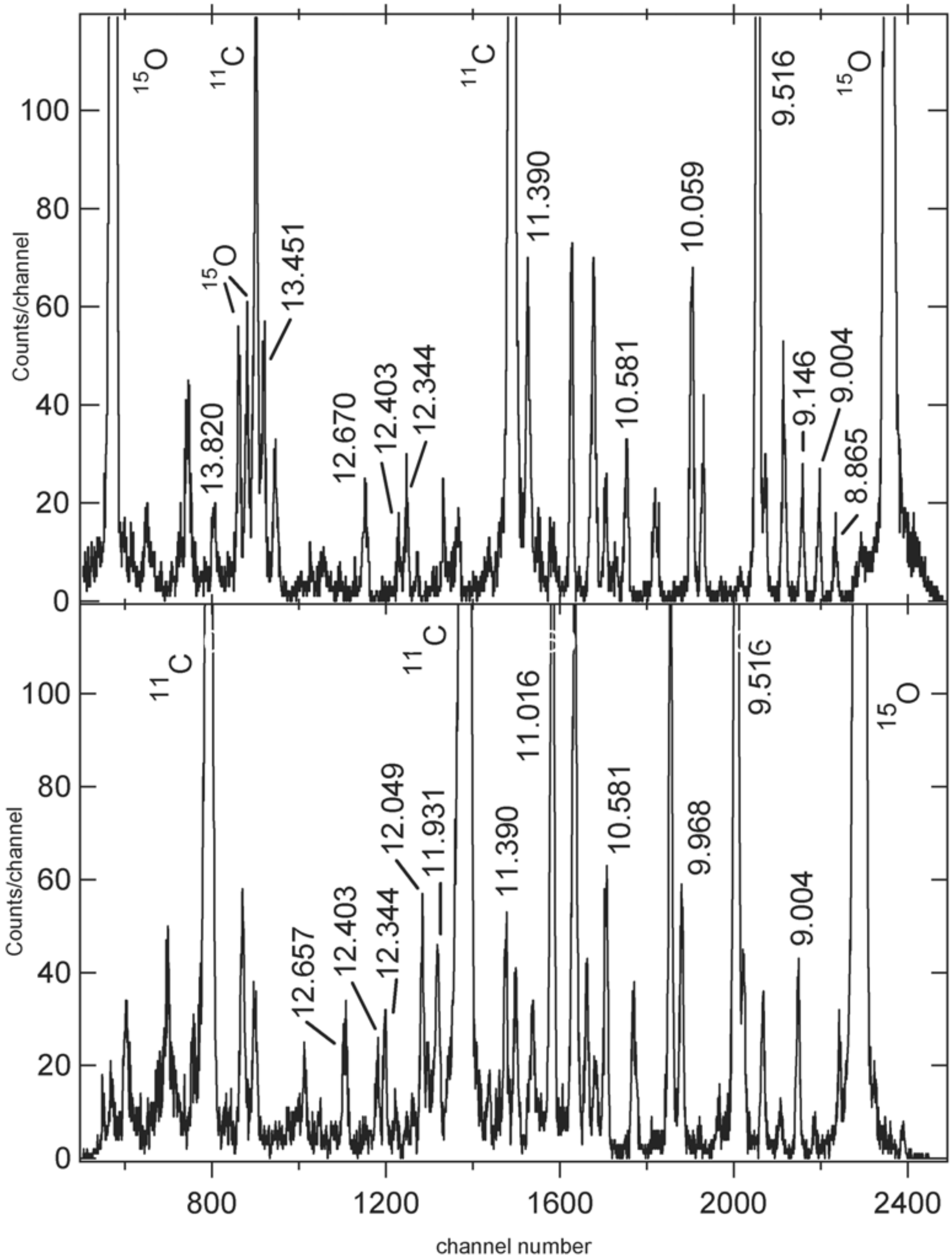

Figure 25: Deuteron momentum spectra from (p,d) reactions on the ^{25}MgO target at (top) θ = 15° and (bottom) θ = 25°. These spectra were used for momentum calibration of the focal plane via the ^{25}Mg(p,d) reaction at their respective angles. Calibration peaks are labeled by their associated E_x (in MeV, from [End90]) in ^{24}Mg. Contaminant peaks from the ^{12}C(p,d)^{11}C and ^{16}O(p,d)^{15}O reactions are also identified here by the appropriate residual nucleus. Peaks used for calibration were chosen based on shape, unambiguity in identification, and known precision of E_x.

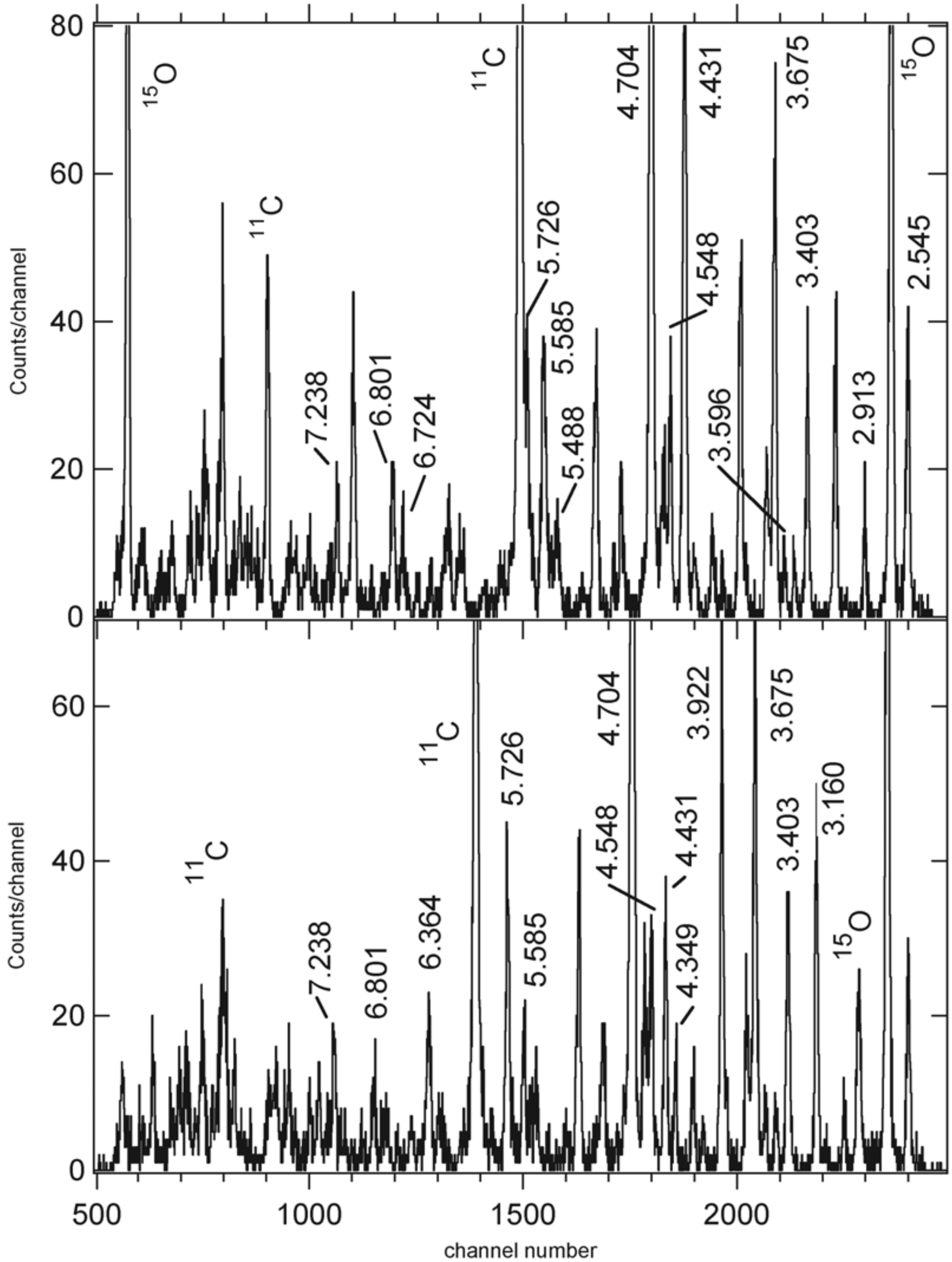

Figure 26: Deuteron momentum spectra from (p,d) reactions on the Al target at (top) θ = 15° and (bottom) θ = 25°. These spectra were used for momentum calibration of the focal plane via the ^{27}Al(p,d) reaction at their respective angles. Calibration peaks are labeled by their associated E_x (in MeV, from [End90]) in ^{26}Al. Contaminant peaks from the ^{12}C(p,d)^{11}C and ^{16}O(p,d)^{15}O reactions are also identified here by the appropriate residual nucleus. Peaks used for calibration were chosen based on shape, unambiguity in identification, and known precision of E_x.

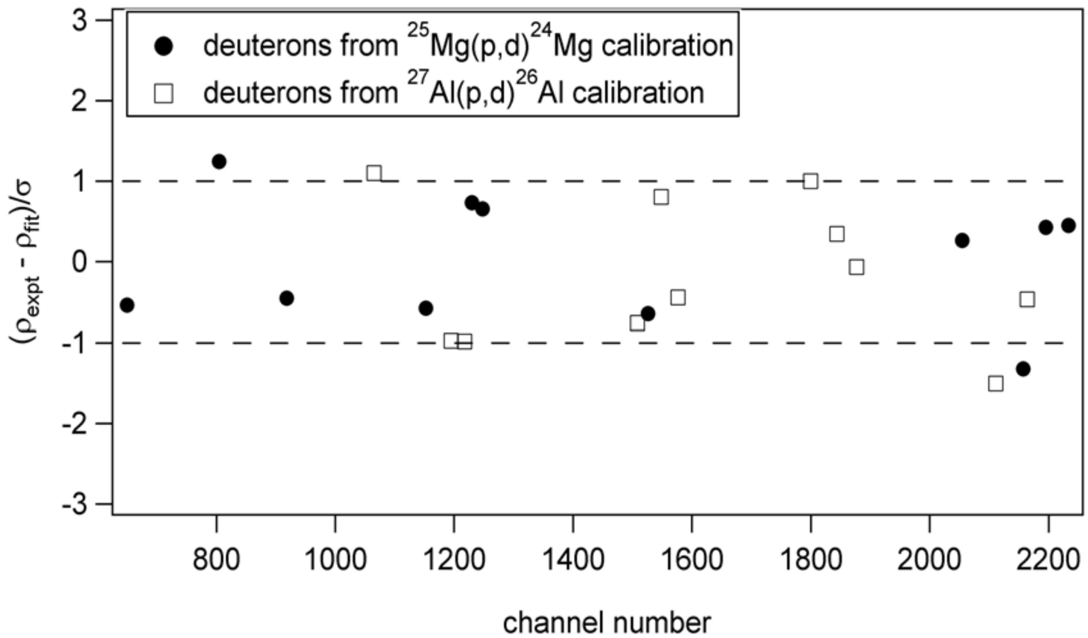

Figure 27. The quantity $\delta = (\rho_{expt} - \rho_{fit})$ represents the residuals from second-degree polynomial fits to the momenta of the deuterons from ^{27}Al(p,d)^{26}Al (open squares) and ^{25}Mg(p,d)^{24}Mg (filled circles). We have divided δ by the 1σ error in this quantity introduced both from the fit parameters, and the peak widths in the deuteron spectra; this is plotted against channel number. The scatter in δ is contained, for the most part, within $\pm 1\sigma$. These fits were to the deuteron spectra at $\theta = 15°$; the residuals from the fits to the deuteron spectra at $\theta = 25°$ were scattered similarly.

To obtain a more precise value for the scattering angle θ, we relied on proton momentum spectra from (p,p') reactions on the ^{24}MgO+C target. At 15°, we observed protons corresponding to several states from ^{24}Mg(p,p')^{24}Mg, ^{16}O(p,p')^{16}O, and ^{12}C(p,p')^{12}C, along with the protons from ^{1}H(p,p)^{1}H elastic scattering. We fit the magnetic rigidities of the observed states in each case with a second-degree polynomial. Since the kinematics of the observed (p,p') reactions are rather different, one can use the difference in $B\rho$ between proton groups from the different reactions to obtain a precise value of θ (assuming the beam energy is known). Using the 4.238 MeV state from the ^{24}Mg(p,p') reaction along with the 4.439 MeV state from the ^{12}C(p,p') reaction, we found $\theta = 14.93(3)$ degrees and $\theta = 25.06(3)$ degrees for the data measured at the nominal lab angles of 15° and 25° respectively (for a beam energy of 33 MeV). In principle, one should be able to improve on the precision of this value by using the ^{12}C(p,p') state along with the ^{1}H(p,p) state (as the kinematics of these two reactions differ even more). However, for the data at 25°, the ^{1}H(p,p) peak merged with a peak from ^{16}O(p,p'); at 15°, we found that the additional uncertainty in determining the centroid of the broad elastic peak from ^{1}H(p,p) led to the same uncertainty in θ as above (along with the same actual angle).

To better determine the beam energy, we relied on our expectation that the shape of the focal plane (namely $\frac{d\rho}{dx}$ and $\frac{d^2\rho}{dx^2}$ for a second degree fit of the magnetic rigidity to position along the focal plane) be consistent among different particle groups. For a given θ, then, one could vary the beam energy used in individual deuteron and triton momentum calibrations until their shapes were consistent. Doing this for each of the two deuteron calibrations (at 15°) in conjunction with a second-degree polynomial fit to triton spectra from ^{25}Mg(p,t)^{23}Mg, we found that $\left|\frac{d\rho}{dx}_{deuteron} - \frac{d\rho}{dx}_{triton}\right|$ was minimized with respect to the beam energy at E_{beam} = 32.994(5) MeV for ^{25}Mg(p,d) and E_{beam} = 32.996(5) MeV for ^{27}Al(p,d). (The values of $\frac{d^2\rho}{dx^2}$ for the three fits were constant and consistent as we varied the beam energy from 32.980 to 33.020 MeV, so we only needed to check the $\frac{d\rho}{dx}$ factors for agreement in the 'shape' of the focal plane between deuterons and tritons.) Repeating this for the deuteron calibrations at 25°, we found beam energies of E_{beam} =

32.996(5) MeV for ^{25}Mg(p,d) and E_{beam} = 32.993(5) MeV for ^{27}Al(p,d). The scattering angle results described above were unchanged when these new beam energies were used in that calculation.

iii. Masses of ^{22}Mg and ^{26}Si

The constant terms in the fits to the deuteron and triton momenta differed. We attribute this effect to imperfections in the constant fraction discriminators (CFDs) used with our focal plane detector. Since our gas-filled detector works in delay-line mode, we detect the position of a particle through an electron avalanche as it moves past a wire (the idealized focal plane) held at high voltage. Protons, deuterons, tritons and alphas entering our detector all lose different amounts of energy in the gas. This may lead an imperfect CFD to trigger on alpha particles a few ns before it would trigger on protons. The end result is that particles of different mass, but the same momentum (or ρ) will register different positions x. This is a small effect (amounting to a difference of 1-2 channels for deuterons and tritons of the same ρ); however, the precision desired for these mass measurements forced us to carefully examine this problem.

Because of this issue, the deuteron calibrations cannot be used to directly determine the absolute magnetic rigidities of the tritons from the ^{24}Mg(p,t) and ^{28}Si(p,t) data. We can, however, make a relative measurement since the *shape* of the focal plane is consistent among deuterons and tritons even if the overall constants in the fits differ. Following this idea, we used each deuteron calibration (at each of the two scattering angles) to determine the magnetic rigidities of the triton peaks corresponding to the ground states of ^{22}Mg, ^{26}Si and ^{14}O. (Recall that the ^{14}O ground state appeared in the spectra from both the ^{24}Mg(p,t) and ^{28}Si(p,t) reactions – see figs. 23 and 24.) Using the beam energy and scattering angle, we then calculated the Q_0 values of ^{24}Mg(p,t)^{22}Mg and ^{28}Si(p,t)^{26}Si relative to that of ^{16}O(p,t)^{14}O. Finally, we assumed the mass table values [Aud03] of ^{24}Mg, ^{28}Si, ^{16}O, ^{14}O, p and t to obtain the mass excesses of ^{22}Mg and ^{26}Si. These are given in table IV, along with their respective statistical and systematic uncertainties.

Table IV: Mass excesses Δ of ^{22}Mg and ^{26}Si from the two independent deuteron calibrations of the focal plane, at each of the two scattering angles. The uncertainties σ_{stat} and σ_{sys} represent statistical error (due to the number of counts in the ^{24}Mg(p,t)^{22}Mg(g.s.) or ^{28}Si(p,t)^{26}Si(g.s.) and ^{16}O(p,t) ^{14}O(g.s.) peaks – see figs. 23 and 24) and systematic error (from varying the beam energy by ± 5 keV, the scattering angle by ± 0.03 degrees, and the target thicknesses by ± 15%).

Calibration	Angle	^{22}Mg Δ (keV)	σ_{stat} (keV)	σ_{sys} (keV)	^{26}Si Δ (keV)	σ_{stat} (keV)	σ_{sys} (keV)
^{25}Mg(p,d)^{24}Mg	15°	-399.4	0.4	0.3	-7138.5	0.6	0.3
	25°	-401.6	0.3	0.4	-7140.6	0.7	0.5
^{27}Al(p,d)^{26}Al	15°	-400.9	0.4	0.3	-7140.2	0.6	0.3
	25°	-399.9	0.3	0.4	-7138.6	0.7	0.5

Given the differences in the results from the calibrations, we extract from our (p,t) data mass excesses for ^{22}Mg and ^{26}Si of -400.5(1.0) keV and -7139.5(1.0) keV, respectively. For comparison, the mass excesses from the 2003 mass evaluation [Aud03] are -397.0(1.3) keV for ^{22}Mg and -7145(3) keV for ^{26}Si.

The triton spectra of figs. 23 and 24 include tritons corresponding to the first excited states of ^{22}Mg and ^{26}Si. In principle, these might be used to make additional mass determinations by making use of the well-known E_x energies of these excited states [End90]. However, the deuteron calibration peaks (at either measured angle) did not encompass the ^{26}Si excited state. This was not an issue for the ^{22}Mg state, and we were able to obtain results for the ^{22}Mg mass consistent with those in table IV – but with about 3x more statistical uncertainty because of the low statistics and irregular shape of these peaks.

D. **Discussion**

As shown in table VI and fig. 28, our result for the mass of ^{22}Mg is in excellent agreement with the re-evaluation of an older determination of the ^{22}Mg mass [Har03], and the recent high-precision Penning trap mass measurements [Sav04, Muk04]. We note that the TRIUMF measurement of E_R for the $E_x = 5.71$ MeV state in ^{22}Mg [Bis03a] requires a measurement of the excitation energy of that state to yield a determination of the ^{22}Mg mass. If one uses the two recent gamma-ray measurements from the $E_x = 5.71$ MeV state of ^{22}Mg (see table V), in conjunction with the E_R measurement, one obtains agreement among all the recent efforts to determine the ^{22}Mg mass.

Table V: γ-ray energy measurements from the $E_x = 5.71$ MeV state in ^{22}Mg.

	γ-ray energy from $E_x = 5.71$ MeV state in ^{22}Mg (keV)
1990 compilation [End90]	5713.9(1.2)
New ANL measurement [Sew05]	5711.0(1.0)
New ORNL measurement [Jew05]	5709.3(3.2)

Table VI: Recent direct and derived determinations of the mass excess (M-A) of ^{22}Mg. Note that in deriving the mass excess of ^{22}Mg from E_R and E_x we have assumed the mass excesses of ^{21}Na and p from [Aud03].

	^{22}Mg mass excess (keV)
2003 mass evaluation [Aud03]	-397.0 (1.3)
Recent re-evaluation of older data [Har74, Har03]	-402 (3)
TRIUMF E_R + E_x of 5.71 MeV state from literature [Bis03a, End90]	-403.4 (1.5)
TRIUMF E_R + recent γ-ray measurement of 5.71 MeV state [Bis03a, Sew05]	-400.5 (1.3)
TRIUMF E_R + recent γ-ray measurement of 5.71 MeV state [Bis03a, Jew05]	-398.8 (3.3)
CPT [Sav04]	-399.73 (67)
ISOLTRAP [Muk04]	-399.92 (27)
Present work	-400.5 (1.0)

With regard to the mass of ^{26}Si: the only measurement used in the 2003 mass evaluation [Aud03] is from [Har74], where the Q_0 value of the ^{28}Si(p,t)^{26}Si reaction was measured as -22009(3) keV. (Measurements prior to this 1974 determination had uncertainties in the ^{26}Si mass of ≥ 13 keV [Har74].) Using this with the current masses of ^{28}Si, p and t [Aud03], the mass excess of ^{26}Si is found to be -7145(3) (which is the value in the 2003 mass evaluation). We note that Hardy and Towner (2005) use a re-calibration of the [Har74] measurement, along with selected earlier measurements to obtain –7145.8(2.9) keV for the mass excess of ^{26}Si [Har05a]. Support for our determination of the ^{26}Si mass excess as -7139.5(1.0) keV is provided by the good agreement of our simultaneous ^{22}Mg mass measurement with the two recent Penning trap results for ^{22}Mg.

To explore the implications of our result on nucleosynthesis in novae, we calculate the resonant reaction rate of ^{25}Al(p,γ)^{26}Si using our ^{26}Si mass compared to that using the 2003 mass evaluation. As discussed in Chapter II, for nova temperatures ($0.1 < T < 0.4$ GK) it is sufficient to consider only those resonances in ^{26}Si with $E_R^{CM} < 500$ keV; table

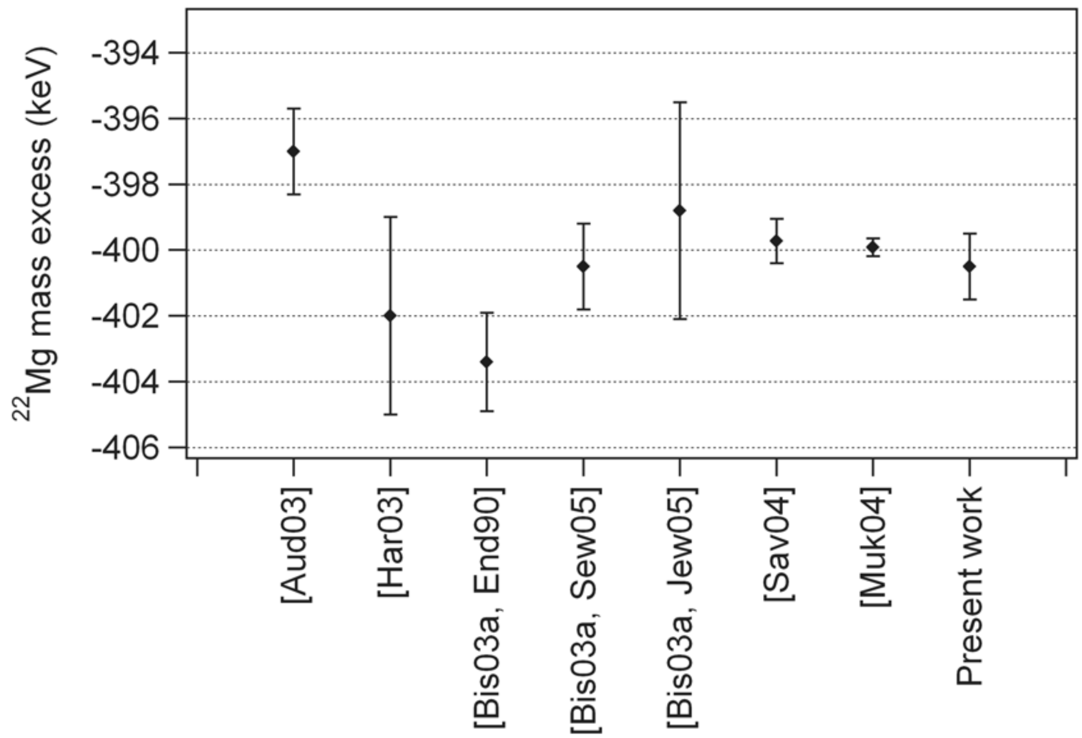

Figure 28. Recent direct and derived determinations of the ^{22}Mg mass excess. See also table VI.

VII lists these resonances and their properties that we used in the rate calculation (see eq. (2)). For the excitation energies E_x of the four resonances in the region of interest, we have used weighted averages of the measurements from [Cag02, Bar02, Par04]; we have chosen the spin-parity assignments of [Cag02, Bar02] for these states. We converted E_x to E_R^{CM} by using both $Q_0^{old} = 5517.7$ keV (the ^{25}Al(p,γ)^{26}Si Q_0 value using [Aud03] for all masses) and $Q_0^{new} = 5512.3$ keV (the Q_0 value using our measurement of the ^{26}Si mass along with [Aud03] for the masses of ^{25}Al and p). The gamma partial widths Γ_γ used are based on shell model calculations and experimental values from ^{26}Mg; they have been taken directly from [Ili96]. Proton partial widths Γ_p in table VII are based on those calculated in [Ili96], but have been modified in proportion to the Gamow factor to account for the changes in E_R^{CM} [Rol88]:

$$\frac{\Gamma_p^{new}(E_R^{CM,new})}{\Gamma_p^{old}(E_R^{CM,old})} = \exp\left(31.29 Z_1 Z_2 \sqrt{\mu}\left(\frac{1}{\sqrt{E_R^{CM,old}}} - \frac{1}{\sqrt{E_R^{CM,new}}}\right)\right)$$

where the energies are in keV, μ is in amu, and Z_1, Z_2 are the atomic numbers of the reactants.

Figure 29 shows the contributions to the resonant rate of ^{25}Al(p,γ)^{26}Si by the 0^+, 1^+ and 3^+ states in ^{26}Si – the 4^+ state is too close to the ^{25}Al + p threshold to be a factor. These calculations are based on our new measurement of the ^{26}Si mass, and use the parameters in table VII. The direct capture (DC) component is also shown; this has been calculated and tabulated in [Ili96].

We see that the unnatural-parity contributions to the total rate dominate at nova temperatures, in agreement with the results of [Cag02] and [Par04]. Figure 29 also gives the ratio of the total resonant rate found using our new ^{26}Si mass, to the total resonant rate found using the 2003 mass evaluation [Aud03] for the ^{26}Si mass. (This ratio is valid for T < 0.4 GK.) For T < 0.04 GK, the resonant rate is reduced significantly by the new ^{26}Si mass; however, we see from fig. 29 that the DC component dominates in this regime. For T > 0.2 GK, we see that the total resonant rate (and hence the total rate since the DC contribution is minor for T > 0.04 GK) is reduced by as much as 30% using our ^{26}Si mass. Additional measurements of ^{26}Si states above the ^{25}Al + p threshold, as well as experimental results for the gamma and proton partial decay widths of these states would help put these indirect rate calculations on firmer ground.

Table VII: Low-energy resonance parameters for $^{25}Al(p,\gamma)^{26}Si$, using our ^{26}Si mass excess of -7139.5 keV. Values for E_x are from a weighted average of the results in [Cag02, Bar02, Par04]; we chose the J^{π} assignments to these states following [Cag02, Bar02]. $E_R^{CM,new}$ was found from E_x assuming our ^{26}Si mass measurement. The partial widths Γ_p^{new} are based on those from [Ili96], but have been modified to take into account the changed resonance energy; Γ_γ are directly from [Ili96].

E_x (keV)	J^{π}	$E_R^{CM,new}$ (keV)	Γ_p^{new} (eV)	Γ_γ (eV)	$\omega\gamma^{new}$ (eV)
5517(3)	4+	4	$\sim 10^{-80}$	.0066	$\sim 10^{-80}$
5672(4)	1+	159	4.5×10^{-9}	0.11	1.1×10^{-9}
5915(2)	0+	403	0.011	.0088	4.1×10^{-4}
5946(4)	3+	434	6.3	.033	1.9×10^{-2}

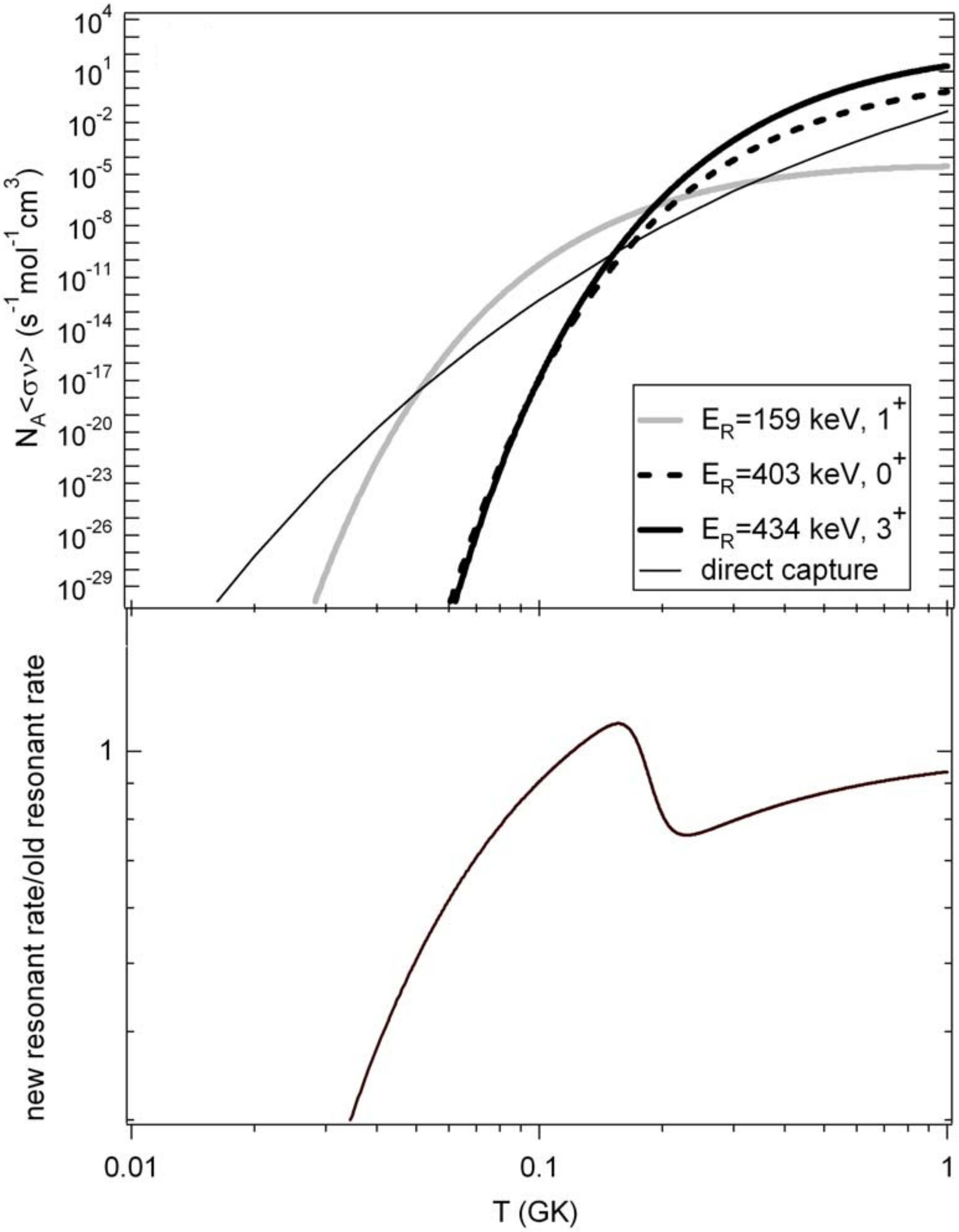

Figure 29: (top) Contributions to the total reaction rate of $^{25}Al(p,\gamma)^{26}Si$ at nova temperatures, assuming our ^{26}Si mass excess of -7139.5 keV. We show the unnatural parity states as the major contributors to the resonant reaction rate at nova temperatures (0.1 < T < 0.4 GK), in agreement with [Cag02, Par04]. Parameters used in the calculations can be found in table VII. The direct capture component is given in [Ili96]. (bottom) The ratio of the total resonant rate assuming our new ^{26}Si mass, to the total resonant rate found using the 2003 mass evaluation for the ^{26}Si mass excess (-7145 keV [Aud03]).

IV. THE E_R^{CM} = 188 keV RESONANCE IN $^{26g}Al(p,\gamma)^{27}Si$

Uncertainty in the strength $\omega\gamma$ of the (nominally) E_R^{CM} = 188 keV resonance in $^{26g}Al(p,\gamma)^{27}Si$ leads to an uncertainty in the $^{26g}Al(p,\gamma)$ rate at nova temperatures of up to 2 orders of magnitude [Ang99]; this in turn, leads to large uncertainty in the amount of ^{26}Al that may be produced in model calculations of nova nucleosynthesis (see Chapters I and II). The single, unpublished, direct study [Vog89] measured $\omega\gamma$ = 55 ± 9 μeV (which we have renormalized to 42 ± 7 μeV – see section C, viii). To further constrain the role of novae to Galactic ^{26g}Al, we have made a new measurement of this resonance strength.

A. **Technique**

To study the $^{26g}Al(p,\gamma)^{27}Si$ reaction, a radioactive ^{26}Al beam was produced and accelerated by the Isotope Separation and ACceleration (ISAC) facility at the TRI-University Meson Facility (TRIUMF) in Vancouver, Canada at energies of ~200 keV/u. This beam impinged upon a windowless H_2 gas target, and the "Detector of Recoils And Gammas Of Nuclear reactions" (DRAGON) was then employed to separate the ^{27}Si reaction products from beam particles that had not undergone a reaction. The strength of the (nominally) E_R^{CM} = 188 keV resonance in $^{26g}Al(p,\gamma)^{27}Si$ was found through the thick-target yield method (eq. (4)); the array of BGO detectors surrounding the gas target also allowed for a measurement of the resonance energy by determining the location of the resonance within the gas target.

B. Experimental Setup

i. The ISAC Facility at TRIUMF

Figure 30 shows the layout of the ISAC facility, which produces radioactive beams via the Isotope Separation OnLine (ISOL) method [Oxo87]. Stable beams are also available from off-line surface-ionization and microwave sources (OLIS).

For our experiment, the TRIUMF cyclotron (not shown) delivered 65 - 70 μA of 500 MeV protons to a SiC target (actually a stack of compressed SiC discs), where spallation reactions produced ^{26}Al (along with many other species). This target (shown in fig. 31) is housed within a tantalum tube, and the assembly is heated to about 2000 °C to enhance the diffusion of products out of the target, and to promote ionization of these species through contact with a rhenium foil lining the ionizer tube (surface ionization).

To improve both ionization efficiency and beam purity, we also employed a laser ionization source (LIS) tuned to selectively ionize ^{26}Al [Koe03, Rau04]. This involved sending three laser beams into the ionizer tube. At 2000 °C, neutral ^{26}Al populates two electronic valence states with roughly similar probabilities; therefore, the ionization scheme used two 12 mW UV lasers to resonantly bring the valence electron of ^{26}Al to an intermediate state, and then a third 6 W, 532 nm laser to non-resonantly remove this electron (see fig. 32). Using this LIS increased the ^{26}Al beam intensity by a factor of ~20 (see fig. 33). We discuss the effects of LIS on beam purity in section C, iv, below.

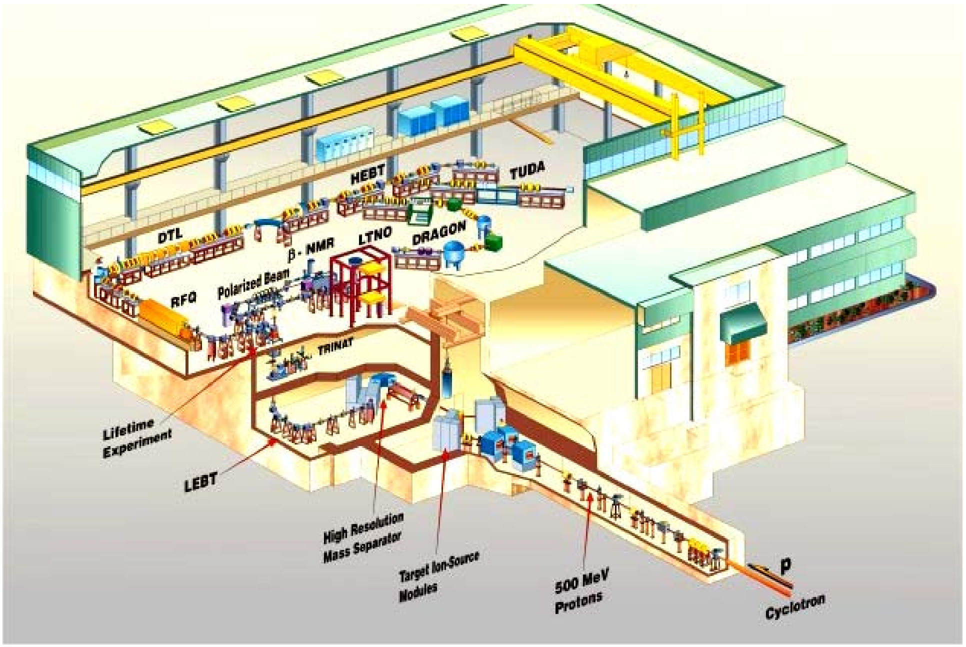

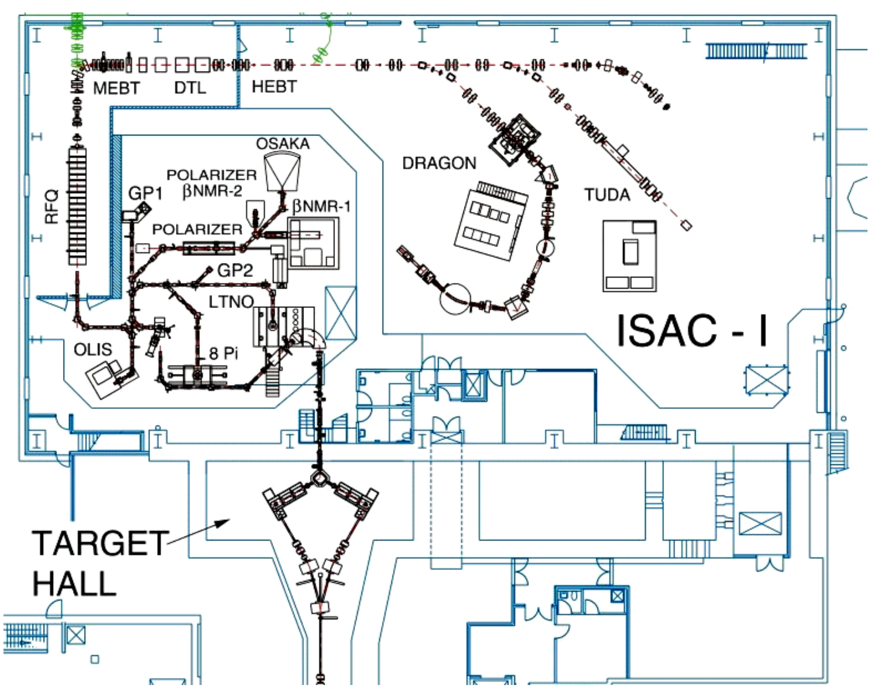

Figure 30: Two views of the ISAC facility and ISAC-I experimental hall at TRIUMF.

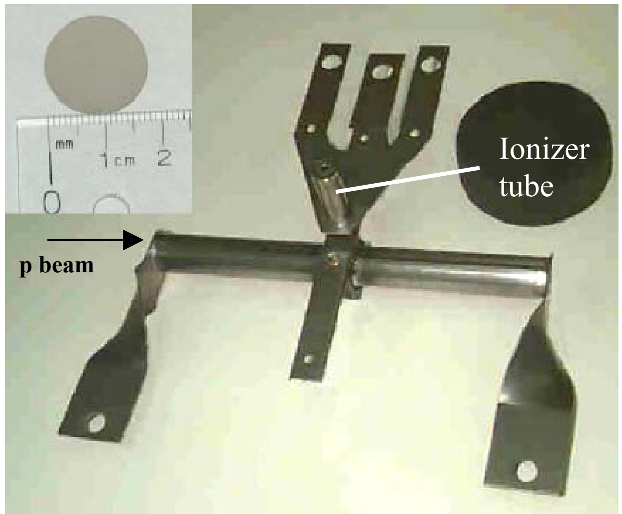

Figure 31: The tantalum target oven and ionizer tube. The inset shows a single compressed SiC target disk. Figure from [Bis03b].

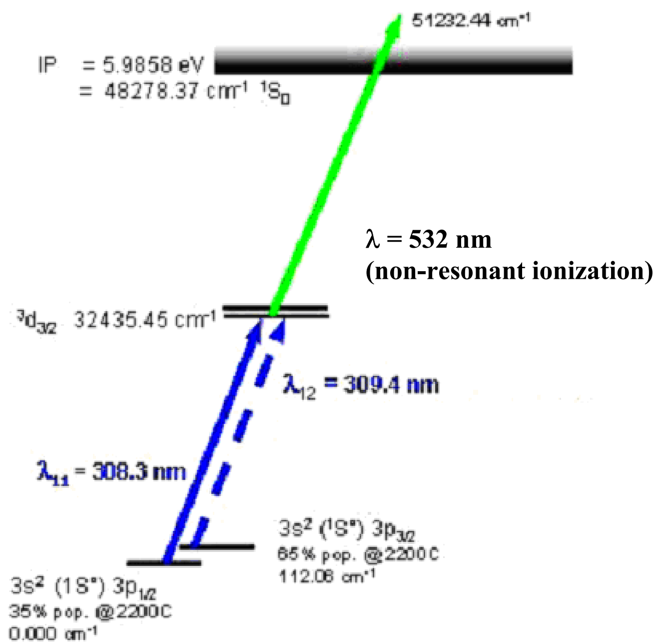

Figure 32: The technique used to ionize ^{26}Al with three laser beams. Figure courtesy of J. Lassen.

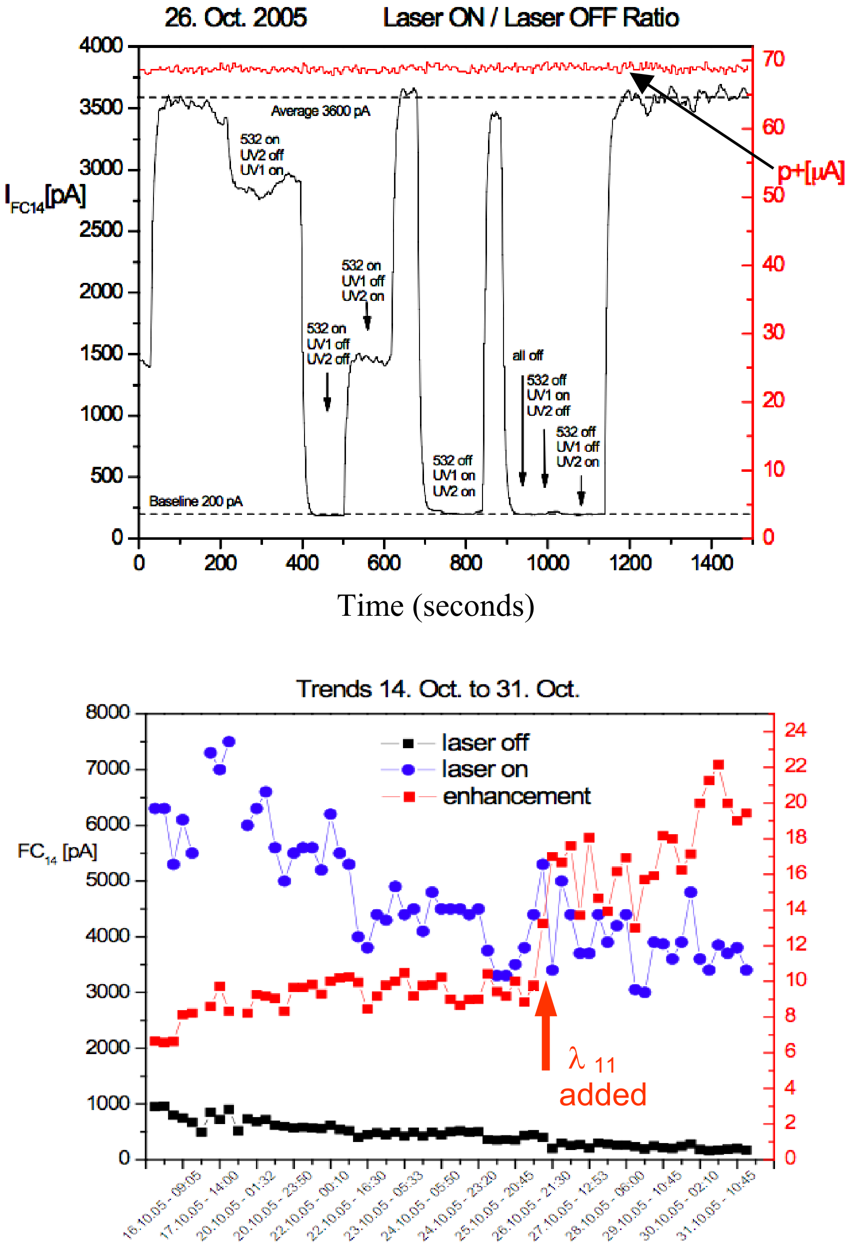

Figure 33: Beam enhancement due to resonant laser ionization. (top) the variation in $^{26g}Al^{1+}$ beam current as some or all of the three lasers are turned on. The beam of protons from the TRIUMF cyclotron is also plotted. (bottom) The beam enhancement factor due to laser ionization as measured throughout the $^{26g}Al(p,\gamma)$ experiment. Note that both of these figures plot $^{26g}Al^{1+}$ beam current as measured at a faraday cup just after the HRMS (FC14); transmission losses reduced the actual beam received by DRAGON. Figures courtesy of J. Lassen.

Ionized products are extracted through the ionizer tube (see fig. 31) held at negative potential. These ions are then sent through a low resolution (*M/ΔM* ~ 400 [Bri97]) pre-separator magnet followed by a high-resolution (*M/ΔM* ~ 5000) mass separator (HRMS) where the species of experimental interest are selected. The principal contaminants to our ^{26g}Al beam were expected to be ^{26}Na ($t_{1/2}$ = 1.07 s), ^{26}Mg (stable) and ^{26}Si ($t_{1/2}$ = 2.23 s), where $M_{26Al}/(M_{26Al} - M_{contaminant})$ = 4526, 6045, and 4779, respectively. (Note that here and throughout we use the tabulated atomic mass values from [Aud03]). We were also concerned about any ^{26m}Al ($t_{1/2}$ = 6.35 s) component to the beam. Since ^{26}Na emits a beta-delayed 1.809 MeV gamma-ray in its decay, we were able to monitor the level of this contaminant by using a high-purity Ge detector pointed at the 'mass slits' of DRAGON (see section B, ii, c). (^{26}Na has an 88% beta-decay branch to the 1.809 MeV state of ^{26}Mg, but the other beta-decay branches all lead to gamma-cascades predominantly through this 1.809 MeV state. The true intensity of the 1.809 MeV gamma-ray due to ^{26}Na beta-decay is 99.1% [End90].) We monitored the ^{26m}Al level by using two NaI detectors at 180˚ relative to each other (also at the 'mass slits') to detect, in coincidence, the 511 keV e^+-e^- annihilation gamma-rays following the positron-decay of ^{26m}Al to the ground state of ^{26}Mg (100%). The ^{26}Mg and ^{26}Si levels in the beam should be much smaller than the ^{26}Na level because of their higher ionization potentials: I = 7.6 eV, 8.2 eV, and 5.1 eV respectively [CRC04]. Since the expression for the surface ionization efficiency [Wil67] involves $e^{(W-I)/kT}$, where W is the work function of the ionizing metal (rhenium for our case, with W = 4.7 eV [CRC04]), the ionization of ^{26}Mg and ^{26}Si should be very much suppressed relative to ^{26}Na.

After exiting the HRMS, the beam is brought up into the ISAC-I experimental hall at 2 keV/u and injected into a 35 MHz radio-frequency quadrupole (RFQ) where it is focused and bunched into packets separated in time by 85 ns. Beam leaves the RFQ accelerator at 150 keV/u and passes through a 10 μg/cm^2 carbon foil that strips electrons from the ions, resulting in the population of several different charge states. We found that 6^+ was the charge state of highest probability for our ^{26g}Al beam. Two magnetic benders are used to remove ions of other charge states; the remaining beam is then sent to a drift-tube linear accelerator where a beam of energy fully variable from 150 – 1500 keV/u can be produced and sent to the DRAGON gas target station. The resonance of interest in ^{27}Si had been measured at E_R^{CM} = 188 keV [Vog89] (E_{26Al} = 194 keV/u); based on this and the expected ~12 keV/u beam energy loss in the 6 torr, 12.3 cm windowless H_2 gas target ([SRIM], but see also eq. (19)), we chose E_{26gAl} ~ 200 keV/u so as to place the resonance roughly in the centre of the target (we accepted E_{26gAl} = 201.0 keV/u). Our results at this beam energy, namely, that the resonance appeared roughly 3 cm downstream of the centre of the gas target, prompted us to make a measurement with E_{26gAl} = 196.8 keV/u as well (to centre the resonance). We also ran off-resonance with E_{26gAl} = 225.7 keV/u.

ii. DRAGON

Figure 34 is a schematic of the DRAGON recoil mass separator, designed to measure low energy proton and alpha capture reactions in inverse kinematics. We discuss the four main components (windowless gas target, gamma detector array, electromagnetic

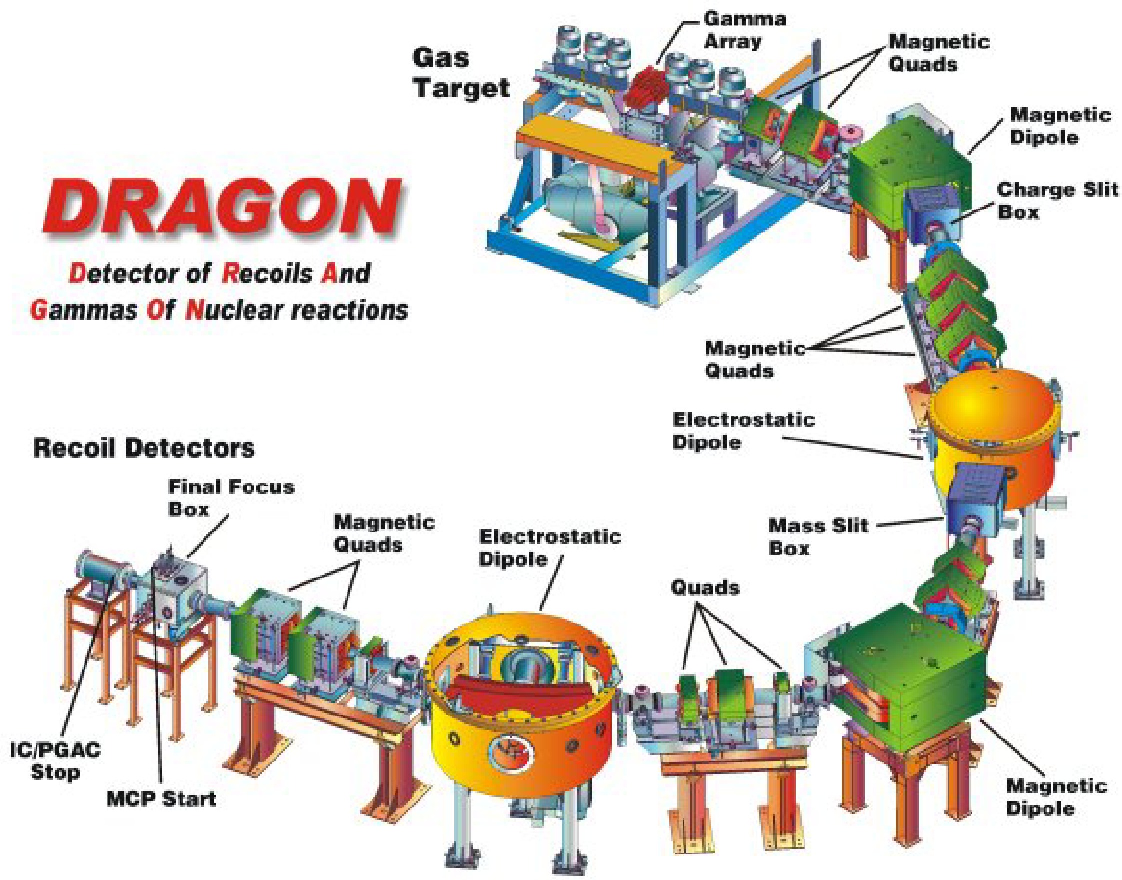

Figure 34: the DRAGON recoil mass separator. The distance along the beam axis from the centre of the gas target to the final focus is 20.4 m.

separator, final focal-plane detection system) in brief here; DRAGON has been described extensively elsewhere [Hut03, Bis03b, Eng03, Eng05, Gig04, Lam04, Wre03a].

a. *Windowless gas target*

The DRAGON windowless gas target is an aluminum cell with its entrance aperture (d = 6 mm) separated from the exit aperture (d = 8 mm) by a distance of 11 cm – see fig. 35. The exit aperture is larger than the entrance to accommodate the forward cone of half-angle $\theta_{1/2}$ within which the trajectories of the recoil nuclei lie (due to momentum conservation):

$$\theta_{1/2} = \arctan\left(\frac{E_\gamma / c}{\sqrt{2 m_{beam} E_{beam}}}\right), \tag{8}$$

where $\theta_{1/2}$ is the lab angle for a radiative-capture recoil, E_γ is the gamma-ray energy and m_{beam}, E_{beam} are the mass and energy of the beam particle, respectively. The exit aperture and downstream pumping tubes (see fig. 35) were designed to allow all recoils satisfying $\theta_{1/2} < 20$ mrad (but see also [Eng03]). For our case, even if we were to consider (incorrectly) $E_\gamma = 7.651$ MeV (the full excitation energy of the state of interest in ^{27}Si), $\theta_{1/2}$ is still only 15.5 mrad. (This state in ^{27}Si is expected to decay primarily through a cascade of three gamma-rays [Vog89] – see fig. 36.) Even accounting for the momentum spread in the beam particles and energy straggling in the target, the solid-angle acceptance should not be an issue (see section C, vii). The entrance aperture and upstream pumping tubes are tapered to conform to the expected beam convergence ($\theta_{1/2}$

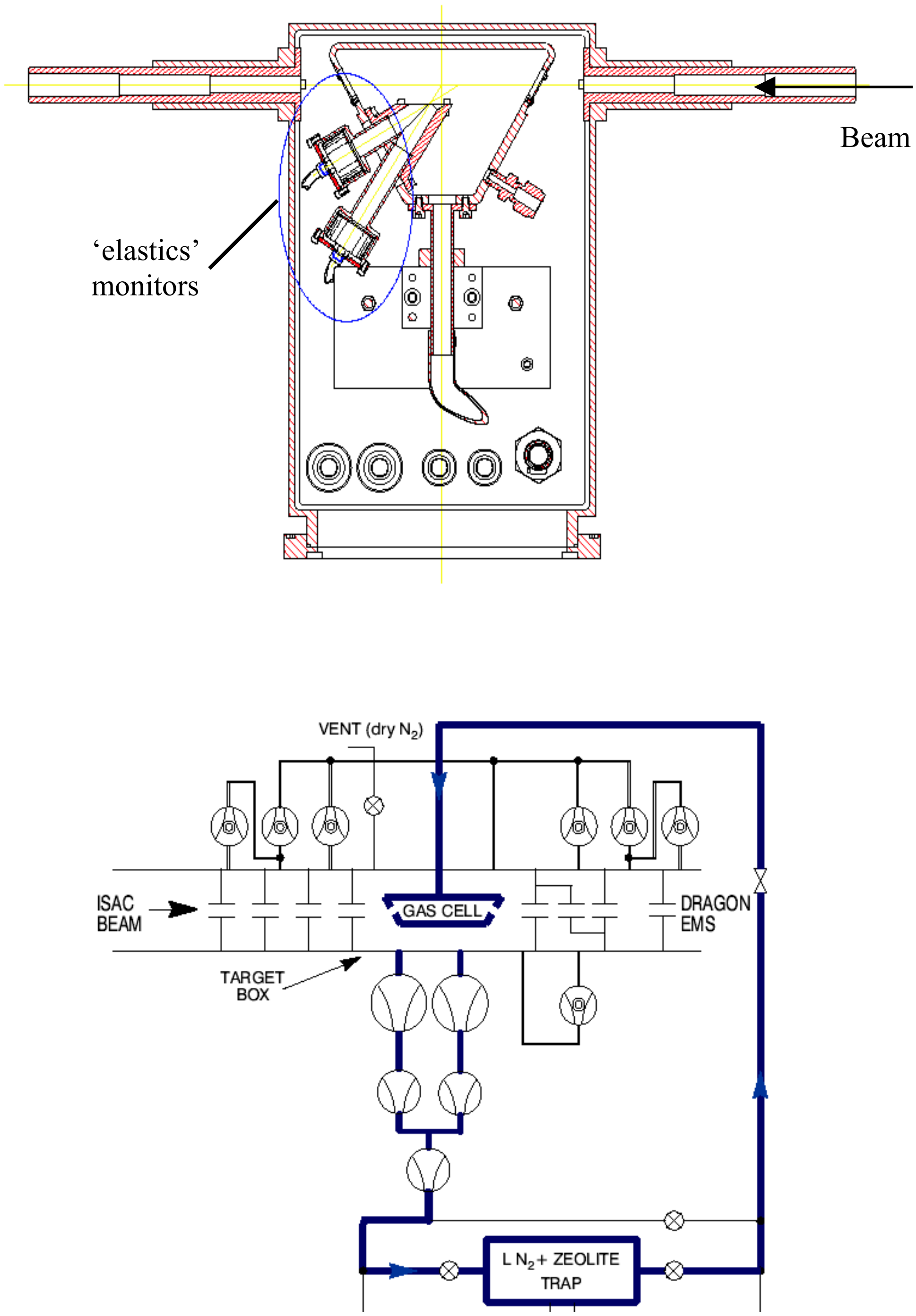

Figure 35: the DRAGON windowless gas target and gas recirculation system. The distance between the apertures of the gas cell is 11.05 cm. Figures from [Bis03b].

$\lesssim$ 5 mrad). Note that both target apertures are tilted at 30° relative to vertical so that jets of gas exiting the apertures are not emitted directly into the tubes of the differential pumping system. With ^{26g}Al beam, we ran with a 6 torr H_2 gas target, stable to better than ± 0.1 torr during the experiment. The target temperature was steady at 300 ± 1 K.

The gas cell is contained within a rectangular pumping box, which is connected to large Roots blowers as in fig. 35. Gas leaving the target cell is cleaned with a zeolite trap at LN_2 temperature and recirculated back to the cell. Turbomolecular pumps are also used with chambers upstream and downstream of the gas cell pumping box, achieving pressures of ~10^{-6} torr at the ends of the pumping system. Since the pressure outside the gas cell is not zero, the effective length of the gas target may be expected to be somewhat larger than the geometric 11 cm length. Indeed, this effective length L_{eff} has been found to be [Eng03, Hut03]

$$L_{eff} = 12.3 \pm 0.4 \text{ cm}. \tag{9}$$

In fig. 35, two detectors are indicated within the gas cell, at 30° and 57° relative to the beam direction. These are 150 mm^2 silicon detectors that are collimated to view the interaction of beam with gas near the central region of the target cell. Since the gas target pressure was monitored separately, the elastic scattering rate measured by these detectors is proportional to the beam current; and we used the monitor at 30° (‘SB0’ or the ‘elastics monitor’) as the primary measure of integrated beam current during the experiment (see section C, iv).

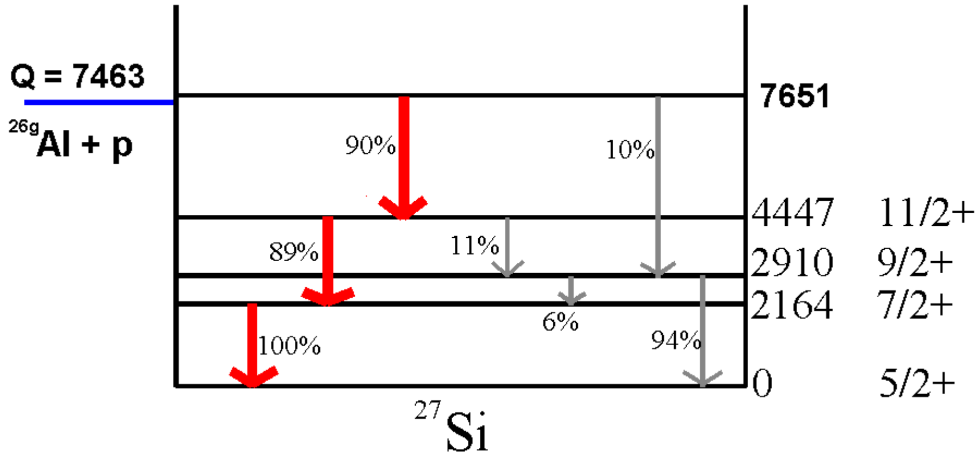

Figure 36: Gamma-decay scheme of the 'E_R^{CM} = 188 keV' proton-capture resonance in ^{27}Si as found by [Vog89]. Energies are in keV.

b. *Gamma detector array*

Figure 37 depicts the array of 30 bismuth-germanium oxide (BGO) crystals that surrounds the gas target. These detect the gamma-rays arising from reactions within the target and add to DRAGON's beam suppression if one requires coincidences between gamma-ray detection in this array and recoil detection at the final focal-plane of the electromagnetic separator. The gamma detector array also allows for a measurement of the resonance energy if one examines the spatial distribution of BGO detectors triggered by reaction-related gamma-rays – see section C, iii.

The array has solid angle coverage of about 90%, and the ensemble-averaged energy resolution has been measured with the 6.13 MeV gamma-ray from a ^{244}Cm/^{13}C source as ~7 % FWHM [Gig04]. This gamma-ray is also used for energy calibration of the BGO detectors. The efficiency of the array for a particular experiment is determined through simulation with GEANT3 [GEA]. The uncertainty in the simulation was found through measuring the efficiency of the BGO array with calibrated sources and comparing this with the simulated efficiency [Gig04]; this gave a relative uncertainty of 10.3% in the simulated efficiency for the entire array.

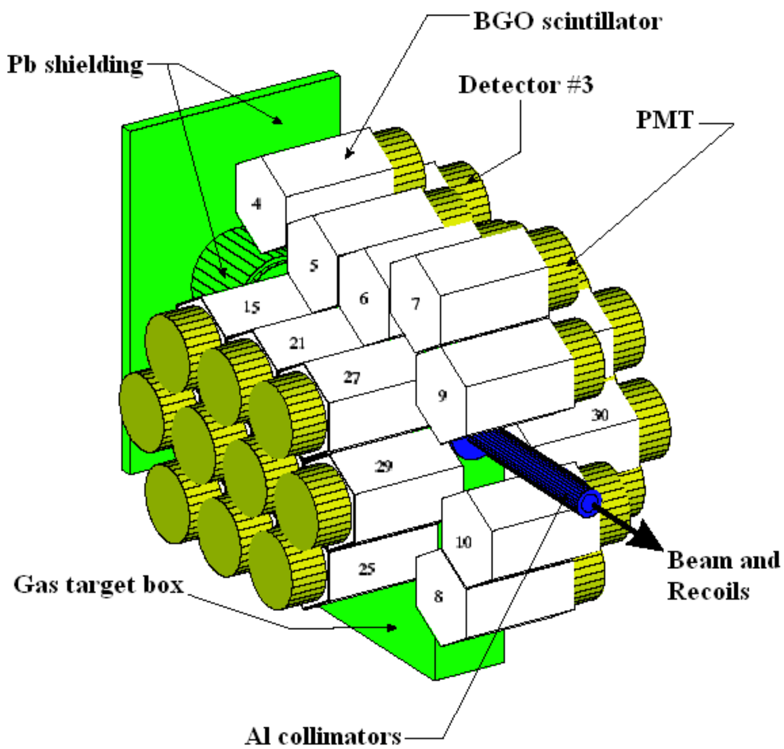

Figure 37: the array of 30 BGO detectors surrounding the gas target.

c. *Electromagnetic Separator*

From momentum conservation, we may find the spread in momentum and energy of the recoil nucleus (p_r, E_r) relative to that of the beam (p_b, E_b) for a radiative-capture reaction:

$$
\begin{aligned}
p_r &= p_b \pm p_\gamma = \sqrt{2m_bE_b}\left(1 \pm \frac{E_\gamma / c}{\sqrt{2m_bE_b}}\right) \\
E_r &\approx \frac{m_b}{m_r}E_b\left(1 \pm \frac{2E_\gamma / c}{\sqrt{2m_bE_b}}\right).
\end{aligned}
\tag{10}
$$

For this experiment, if we take the ^{26g}Al beam energy as ~ 5 MeV and set $E_\gamma = E_x = 7.65$ MeV, we find the momentum and energy spread of ^{27}Si recoils is only ± 1.5% and ± 3.0% of beam momentum and energy respectively. Since both beam and recoils will exit the gas target (in a variety of charge states), the electromagnetic separator (EMS) must provide a high degree of beam suppression to allow an accurate yield measurement. Separation was obtained through a magnetic dipole (MD1) and electric dipole (ED1) – see fig. 34. Each of these units was followed by a set of moveable slits immediately downstream, at horizontal focus locations. The first set of slits is termed the 'charge' slits as the most populated recoil charge state is selected here, given the mv/q dispersion from MD1. The second set of slits is termed the 'mass' slits as the recoil mass (actually the recoil velocity) can be selected using the mv^2/q dispersion from ED1 (as q is now known). The second stage of DRAGON repeats the configuration of the first stage; a set of 'final' slits is available for further beam rejection at the focus following ED2. The mass resolution for the entire separator is $M/\Delta M \sim 600$, and for the first stage only (up to the mass slits) we have $M/\Delta M \sim 150$ [Hut03]. These are modest, but acceptable given the mass difference $M/\Delta M \sim 26$ between ^{26}Al and ^{27}Si. To avoid losing any ^{27}Si recoils in our measurement, the final slits were operated with a wide opening; the second stage of DRAGON acted only to transport ions from the mass slits to the detectors after the final focus. The procedure for tuning the EMS is described on the DRAGON website [DRA].

Beam transmission between a faraday cup located just after the charge slits (FCCH), and another located just after the final slits (FCF), is routinely better than 99%. We note that the A/q of a beam (or conversely, the settings of the electromagnetic elements) may be checked while tuning with the relation

$$\frac{A}{q} = \frac{(24.1)B^2}{V} \tag{11}$$

where V is the ED1 voltage in kV, and B is the MD1 field in kG. Deviations from eq. (11) are expected to be < 1% in A/q. The EMS was tuned for $^{27}Si^{4+}$ recoils. Since the yield of the reaction clearly depends on the recoil charge-state chosen, we later (see section C, vi) measured a charge-state distribution (CSD) using a ^{28}Si beam.

The detectors monitoring beam contamination (mentioned in section B, i) were positioned about the mass slits, external to the actual beamline – see fig. 38. The high-purity Ge detector, pointed at the mass slits to monitor the ^{26}Na component of the beam, was calibrated in energy and efficiency using ^{22}Na ($t_{1/2}$ = 2.6 y, E_γ = 1275 keV), ^{60}Co ($t_{1/2}$ = 5.3 y, E_γ = 1173, 1332 keV), and ^{88}Y ($t_{1/2}$ = 107 d, E_γ = 898, 1836 keV) sources mounted in succession at the mass slits. The absolute efficiency of this detector, after compensating for attenuation in air and the chamber housing the mass slits, was found to be

$$\eta_{Ge} = (1.22 \pm 0.10) \times 10^{-5} \tag{12}$$

for $E_\gamma = 1836$ keV (η_{Ge} is a photopeak efficiency). The two NaI detectors, oriented at 180° relative to each other about a 'horn' protruding above the mass slits box, monitored the ^{26m}Al level in the beam. The absolute efficiency for 511 keV gamma-rays in coincidence (taking into account the solid angle coverage of the 'horn') was found to be

$$\eta_{NaI} = (6.07 \pm 0.06) \times 10^{-6} \tag{13}$$

using a calibrated ^{22}Na source placed into the interior of the horn.

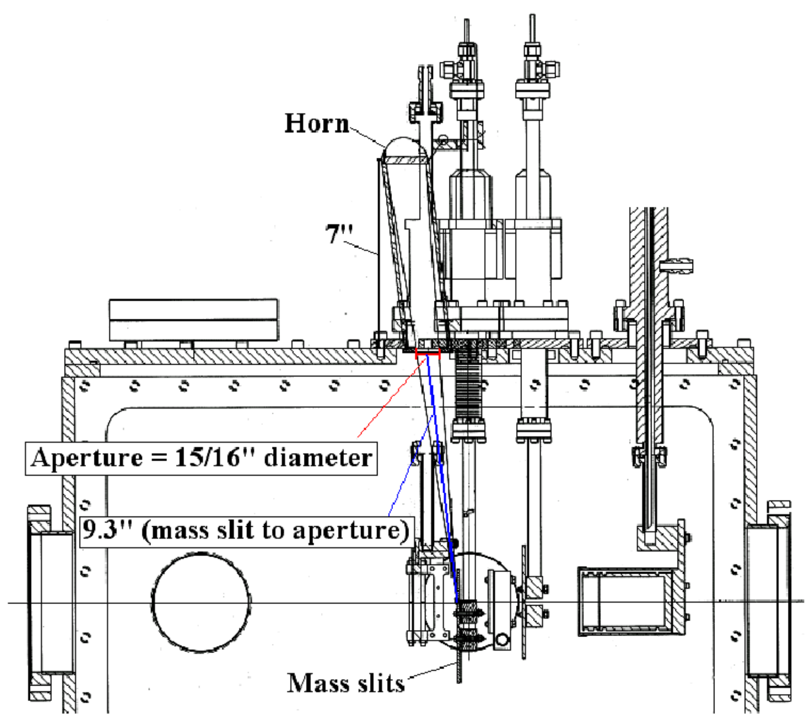

Figure 38: the DRAGON mass slits chamber. The Ge detector (located external to the chamber) was pointed at the mass slits, while the two NaI detectors were positioned about the 'horn' and oriented at 180° to each other.

The energy *E/A* of the ^{26}Al beam delivered to DRAGON was measured using MD1, according to:

$$\frac{E}{A} = \kappa\left(\frac{qB}{A}\right)^2, \tag{14}$$

where *q* is the chosen charge-state of the beam (in units of *e*) and *B* is the magnetic field of MD1 in Gauss. The value of κ has been determined through the measurement of narrow resonance reactions using stable beams [Eng05]:

$$\kappa = (4.819 \pm 0.003)\times 10^{-4} \quad \text{keV/amu/(Gauss/amu)}^2.$$

Basically, *E/A* was calculated with eq. (14) by adjusting *B* to centre the beam horizontally at the charge slits (narrowed to a width of 2 mm from the operational width of 15 mm) following MD1. For a single energy measurement, the uncertainty will depend on κ as well as the beam tune and the range in *B* that allows a 'centered' beam; the method is accurate to ~0.2% [Eng03].

d. *End Detectors*

A double-sided silicon strip detector (DSSSD) was mounted about 65 cm downstream of the final focus of the EMS for detection of the ^{27}Si recoils. Composed of two orthogonal layers of 16 strips each (see fig. 39), this detector provided energy, timing and position information (the upstream or 'front' strips were vertically oriented, and the downstream or ‘back’ strips were horizontally oriented). Each individual strip was 3 mm wide, 5 cm long and separated from its neighbouring strips by ~110 μm of insulating SiO_2. The energy resolution is expected to be ~ 1 % [Wre03b]. For this experiment, we used DSSSD #2069-22, which has a 251 μm-thick active layer and is rated at -60 V bias. This (brand-new) DSSSD was calibrated prior to the experiment (assuming a dead layer of 0.4 μm) with a ^{241}Am^{239}Pu^{244}Cm alpha source (E_α = 5.485 MeV, 5.157 MeV, and 5.805 MeV respectively). A hybrid thermoelectric (Peltier)/liquid system to cool the DSSSD has been developed in the hope of improving the energy resolution by reducing the contribution of thermal noise [Cal73]. Initial tests have not shown a significant improvement in resolution after cooling the detector to -10 °C [Wre03a]. However, cooling has been shown to allow radiation-damaged detectors to operate normally again, since leakage current is a strong function of the temperature of the detector [Lin99, Wre03a]. (Here we classify a DSSSD as ‘radiation-damaged’ if it cannot hold full

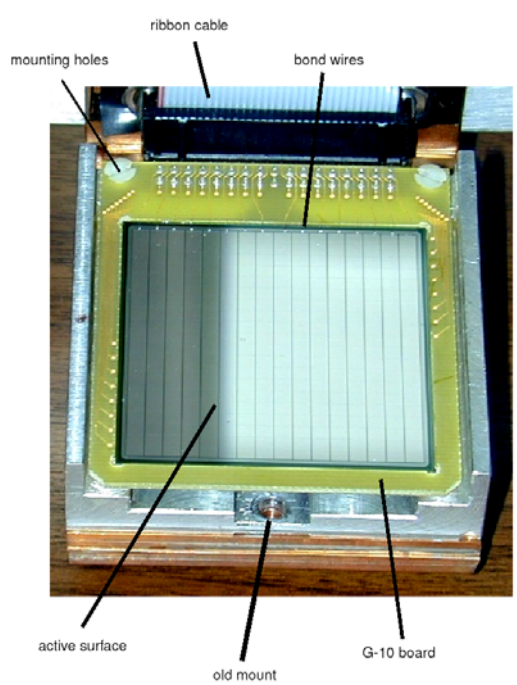

Figure 39: a double-sided silicon strip detector (DSSSD). Figure from [Wre03a].

depletion bias without exceeding a leakage current of ~ 2 μA at room temperature.) Indeed, midway through the ^{26g}Al(p,γ) experiment we noticed that the leakage current of the DSSSD (held at room temperature) had jumped to ~ 1 μA from ~ 100 nA at a bias of -120 V. We then ran with the detector cooled to -10 °C, at which the leakage current dropped to ~ 50 nA. The efficiency of the DSSSD should be ~100%; however, charged particles entering the detector through the interstrip insulator material will induce a reduced pulse height [Yor87]. It was found through alpha tests that 96.15 +/- 0.10 % of all alpha particles bombarding a DSSSD should appear at full pulse height [Wre03b]. A recent re-measurement of this effect for the front strips of the DSSSD used in this experiment [Pea06] found that 97 ± 1% of all alpha particles appeared at full pulse-height:

$$\eta_{DSSSD} = 97 \pm 1 \ \%. \tag{15}$$

A microchannel plate (MCP) detection system was mounted immediately downstream of the final slits to allow a local time-of-flight (TOF) measurement between it and the DSSSD for additional beam suppression [Lam04]. As shown in fig. 40, beam ions impinging upon a 20 μg/cm^2 carbon foil knock out electrons, which are then deflected by wire grids and detected by the MCP planes; the incident heavy ions continue downstream to the DSSSD. We operated the grids at ± 2100 V, and the MCP at +3000 - 3150 V. Higher MCP bias, with an expected improvement in efficiency, could not be attained without serious noise-related sparking of the system. This could perhaps be remedied by improving the vacuum (~ 1.2 x 10^{-6} torr) in the detector box.

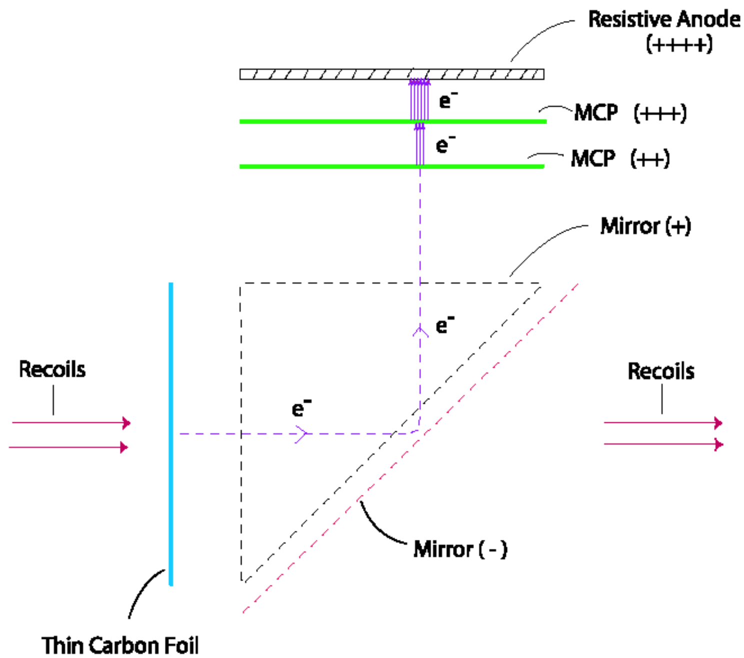

Figure 40: schematic of the microchannel plate (MCP) detection system. Heavy ions impinge upon a thin foil, ejecting electrons. These electrons are then deflected to the MCP for detection, and the heavy ions continue on their original trajectory. Figure from [Lam04].

A gas-filled ionization chamber (IC) is available for use with DRAGON, though it was not used for the ^{26}Al(p,γ)^{27}Si experiment (except for the charge state distribution measurement – see section C, vi). The IC and the chamber housing the DSSSD occupy the same physical space along the beam axis. When the IC is desired, the DSSSD box is slid out of the beam axis, and the IC is moved into the former position of the DSSSD box. As shown in fig. 41, the IC provides a ΔE-E measurement through signals from two successive anodes (the gas pressure is adjusted to ensure this condition, and the third anode is used only to check that this condition is fulfilled). A Frisch grid screens the anodes from the gas volume to prevent induced charges. Isobutane at ~20 torr is used to fill the IC, and a thin mylar or SiN foil is used for the entrance window. A detailed description of this detector can be found in [Oul07].

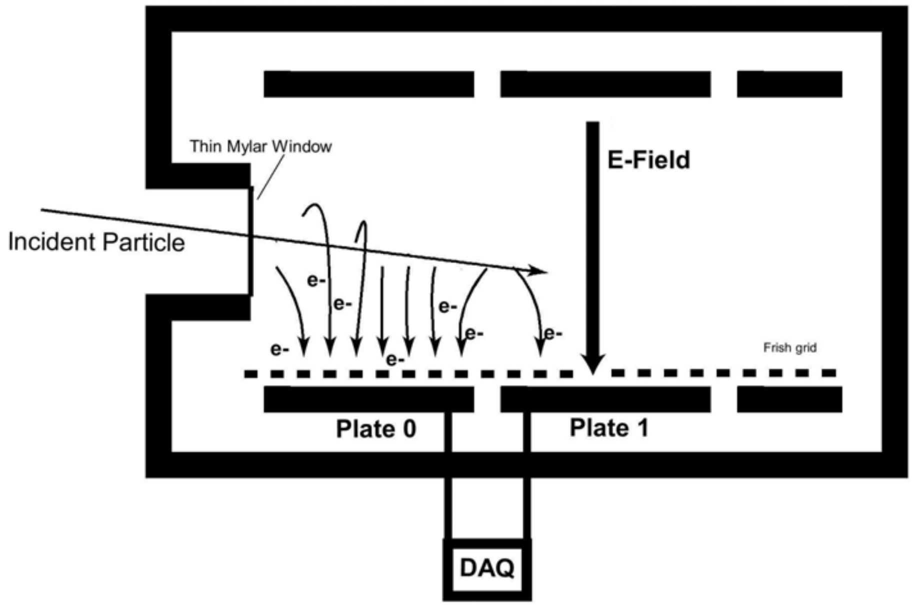

Figure 41: schematic of the DRAGON ionization chamber. Figure courtesy of C. Ouelett.

e. *Iris*

To reduce background in the BGO detectors from beam contaminants (e.g., gamma-rays from the decay of ^{26}Na) we installed an adjustable iris-type aperture (Edmund Optics 53911, see fig. 42) upstream of the gas target to skim off any beam halo. The diameter of the iris can be adjusted without breaking vacuum through the use of a single knob external to the beamline. The diameter is variable from 2.3 mm to 19 mm, where 1 full turn of the knob changes the diameter by about 0.5 mm. The entire iris is also adjustable in x and y by ± 5 mm. Each of the 14 stainless-steel leaves is 60 μm thick [Tol06]: thin enough to avoid significant slit-edge scattering of any intercepted beam. It is located 25 cm upstream of the gas target cell, but downstream of a faraday cup (FC4) traditionally used to monitor the beam received into the gas target (see fig. 43). The opening of the iris relative to the size of the beam spot can be monitored through the use of a CCD camera looking into the gas target through the alignment port of MD1. Throughout this experiment, the iris was operated at diameters of 4 - 5 mm and centered on the gas cell entrance window. ISAC operators had tuned the ^{26g}Al beam to DRAGON to give ~ 95% transmission between FC4 and FC1 with the iris wide open, without gas in the target. We measured transmission between FC4 and FC1 as 91% with the iris at a diameter of 4 mm (also without gas in the target).

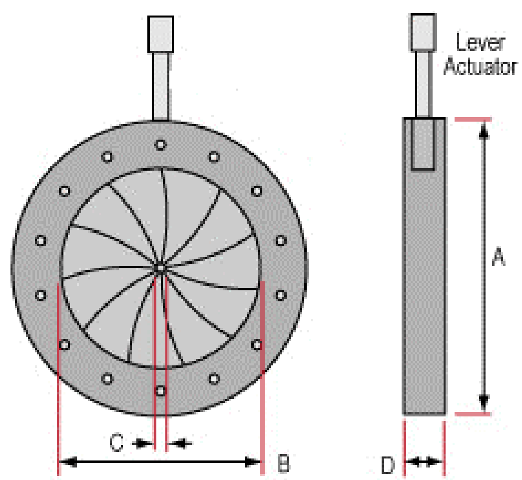

Figure 42: schematic of the aperture of adjustable diameter ('iris') installed upstream of the DRAGON gas target. Figure from Edmond Optics [Edm].

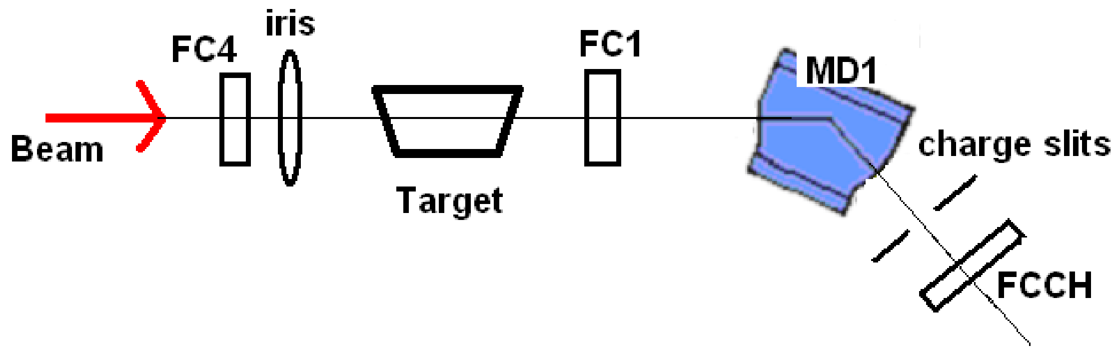

Figure 43: The relative locations of the iris and faraday cups FC4, FC1 and FCCH within DRAGON. Figure is not to scale.

f. *Data Acquisition Electronics and Software*

Figure 44 shows a schematic of the electronics through which signals from the 30 gamma-ray detectors and the heavy-ion detectors (16x2 DSSSD strips) are processed - all of these signals are separately amplified and discriminated [Bis03b, Eng03, Hut03]. Events in the elastics monitor SB0, NaI detectors, and Ge detector are essentially processed in a similar fashion as the events in the DSSSD. A TAC is used between signals from the MCP and DSSSD (front strips), where the MCP signal is delayed and gives the stop condition. Independent trigger signals are produced from the heavy-ion and gamma-ray detectors and stored in separate memory buffers; coincident events are identified in software as those with gamma-ray and DSSSD triggers (front strips) within 10 μs of each other. As well, scalers counted all events presented to the DSSSD, MCP, SB0, BGO array and contaminant detectors. The data were acquired with the MIDAS [MID] system. Various 1-D and 2-D spectra from the detectors (singles and coincidence) were prepared online using ROOT [ROOT]; event files were available for off-line analysis using either ROOT or NOVA [NOVA].

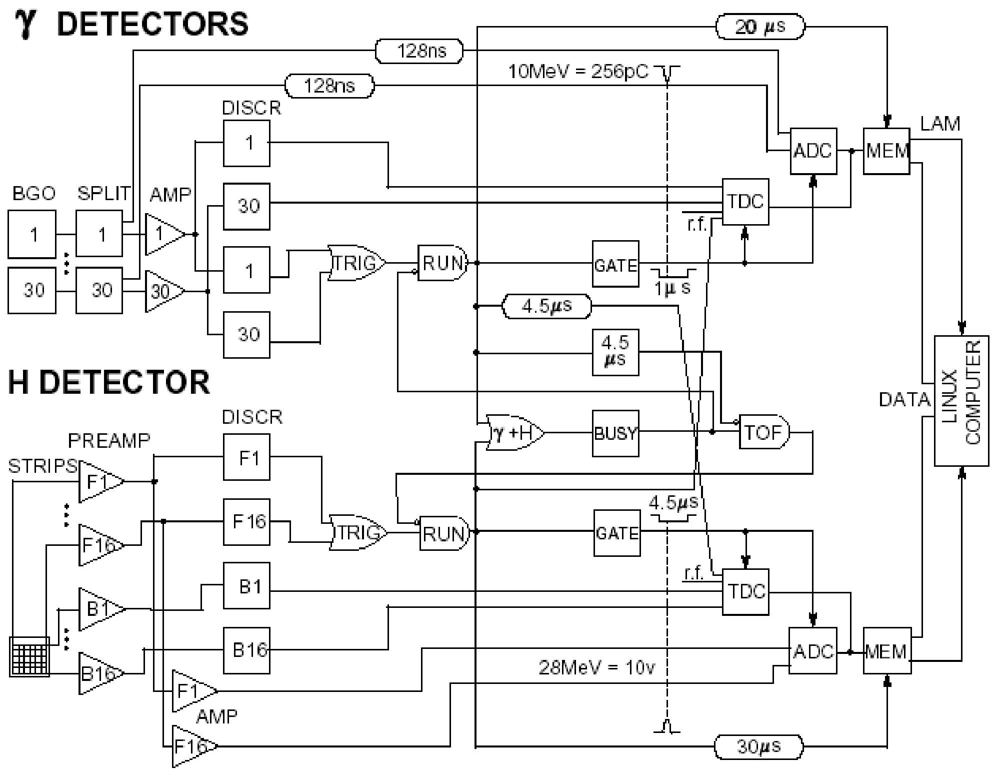

Figure 44: Block diagram of the electronics used to process signals from the 30 BGO detectors (γ detectors) and 16x2 DSSSD strips (H detector). In addition to this, a TAC was used between the MCP and the front strips of the DSSSD. The electronics used with the elastics monitor and contaminant detectors were similar to those used by an H detector. Figure from [Hut03].

C. Results and Analysis

All of the experimental data described in this section were acquired from Oct. 13 – 31, 2005. We note that we had also attempted this same measurement over the period June 18 – July 12, 2005. As a power supply used with the laser ionization system failed less then halfway through that experiment, beam intensities in this prior run were significantly lower than in the October run. Beam contamination was consequently higher as well, triggering more random coincidences. We comment briefly on the June/July measurement in Appendix A.

i. Calibration

Prior to receiving ^{26g}Al beam, we measured the E_R^{CM} = 214 keV (E_{24Mg} = 221 keV/u) resonance in ^{24}Mg(p,γ)^{25}Al (see fig. 45) to determine where to expect ^{27}Si recoils in separator time-of-flight (started by a hit in the BGO array and stopped by a hit in the front strips of the DSSSD), local time-of-flight (started by the DSSSD and stopped by the delayed MCP), and DSSSD energy (as measured in the front strips). The energy and strength of this resonance have recently been measured – see table VIII.

Table VIII: recent measurements of the E_R^{CM} = 214 keV resonance in ^{24}Mg(p,γ)^{25}Al. Note that the [Eng05] measurement was made with DRAGON.

	E_R^{CM} (keV)	$\omega\gamma$ (meV)
[Pow99]	214(1)	12.7(9)
[Eng05]	214.0	10.9(2.0)

The ^{24}Mg beam was produced using the off-line surface ionization source. We chose charge state 5^+ for the beam, and accepted E_{24Mg} = 228.1 keV/u. The gas target contained 4 torr of H_2 gas, and the energy loss of the beam within the target was measured as

$$\varepsilon = 81.7 \pm 0.5 \text{ eV}/10^{15} \text{ atoms/cm}^2 \qquad (16)$$

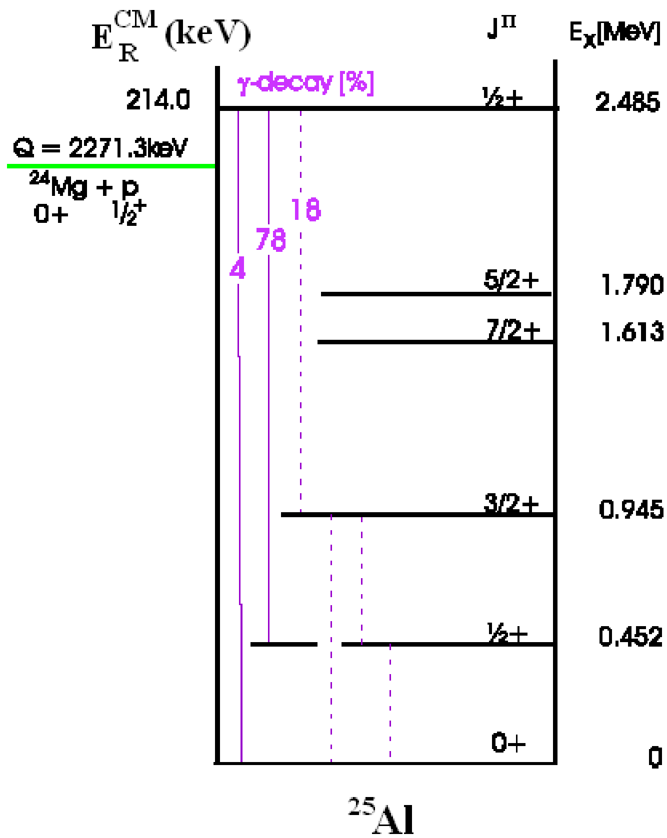

Figure 45: Decay scheme and location of the E_R^{CM} = 214 keV resonance in ^{25}Al from the $^{24}Mg(p,\gamma)$ reaction. The dotted lines in the γ-decay indicate γ-rays with energy below the trigger thresholds on the BGO detectors. Figure from [Eng03].

(or 10.9 keV/u at 4 torr H_2). This is in good agreement with the [Eng05] value of ε = 83.4 ± 3.1 eV/10^{15} atoms/cm^2; our result has better precision as it relied on four individual measurements at different pressures. Following [Eng05], we tuned the EMS for $^{25}Al^{4+}$. The $^{24}Mg^{5+}$ beam current just prior to entering the target (measured with FC4) was typically 13.5 enA (the iris was wide open).

Figure 46 shows a typical coincidence separator TOF spectrum from one of the $^{24}Mg(p,\gamma)^{25}Al$ runs; the recoil peak of 51 events at mean channel 6985 is clear, and background is negligible. Note that 2 channels in the separator TOF spectrum are equal to 1 ns. Figure 46 also shows, for these same 51 events, the energy in MeV as measured in the front strips of the DSSSD, and the local TOF spectrum (with the MCP at +3000 V) respectively.

We intended to determine a strength for the E_R^{CM} = 214 keV resonance in ^{25}Al from our measurements. However, the trigger thresholds on the detectors of the BGO array had mistakenly been set too high (~ 2 MeV), rejecting many of the 2.053 MeV gamma-rays from $^{24}Mg(p,\gamma)$ reactions (see fig. 47). While this effect could be modeled, and the actual BGO array efficiency then simulated in GEANT3, the extent of the threshold effect here would make the extraction of this efficiency unreliable for a precise resonance strength measurement. Based on the measured strengths in table VIII for this ^{25}Al resonance, we believe the thresholds reduced our yield by a factor of ~ 3 - 4, because of a BGO efficiency of only ~ 10 %. In addition, we found that the detectors of the BGO array had been poorly calibrated in energy for the ^{24}Mg runs. This was corrected for the ^{26}Al runs,

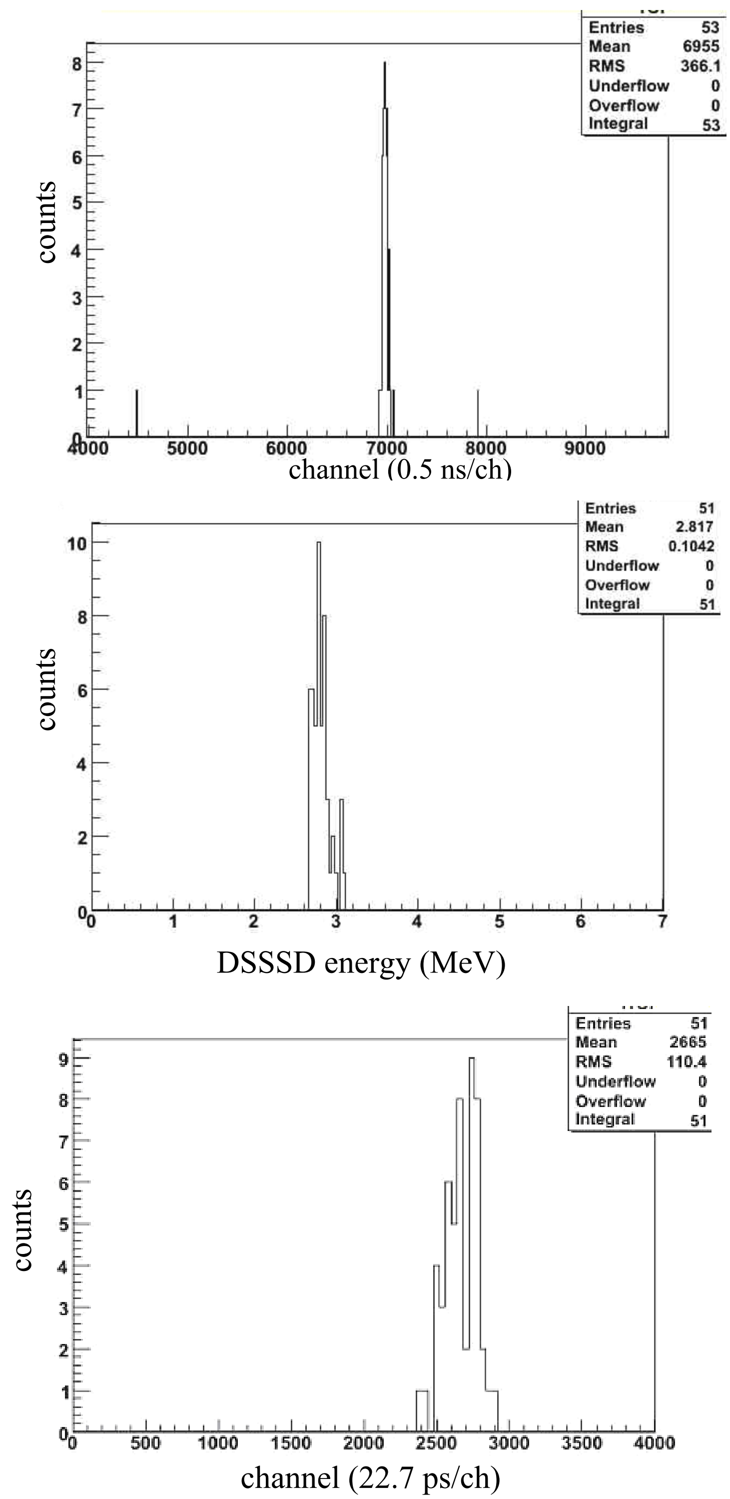

Figure 46: coincidence events from our measurement of the E_R^{CM} = 214 keV resonance in ^{25}Al. (top) separator TOF, no cuts. (middle) DSSSD energy, using a cut around the peak in separator TOF. (bottom) local TOF, using a cut around the peak in separator TOF.

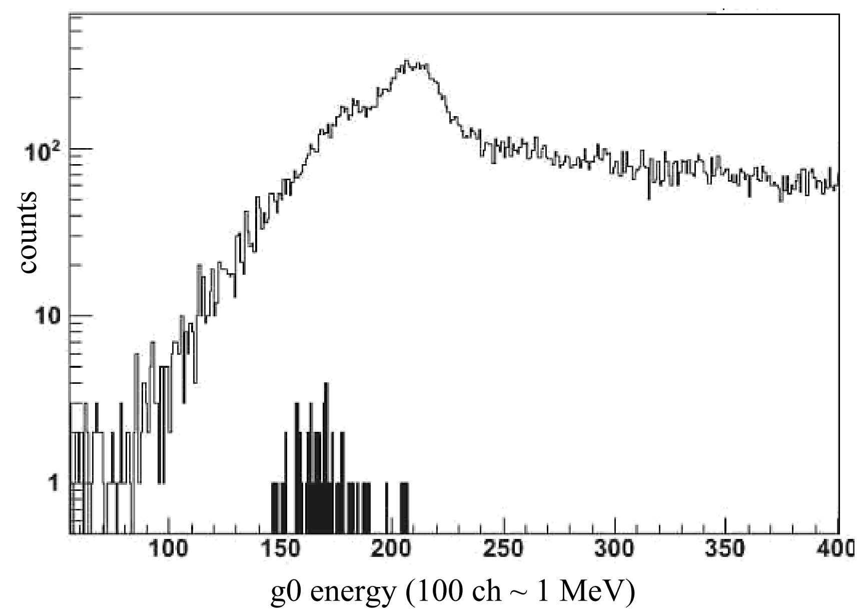

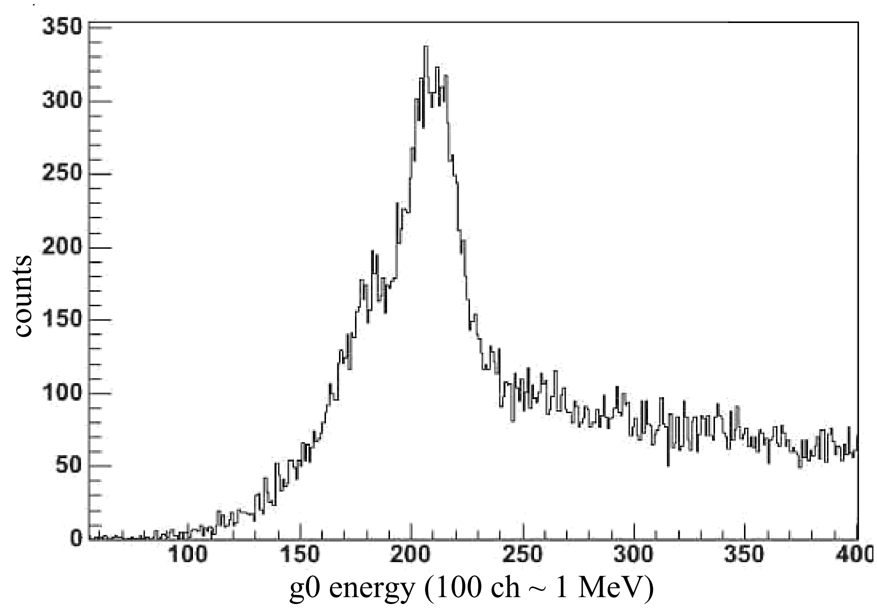

Figure 47: (top) highest-energy gamma-rays (g0) detected from the 51 coincidence recoil events of fig. 46 (shaded). These are superimposed on singles g0 events from the same run. (bottom) The same singles g0 events as in (top), but shown on a linear scale to highlight the location of the 'soft' trigger threshold on the BGO detectors.

but this issue would make extraction of the BGO array efficiency from comparison with GEANT3 simulation all the more difficult for the ^{24}Mg runs.

We can however, make a measurement of the resonance energy using the spatial distribution of BGO detectors about the target. Figure 48 shows the distribution in z (i.e. along the gas target, with $z = 0$ mm corresponding to the target centre) of 'leading gammas' (highest energy gamma-rays measured) from the 51 coincidence events in the separator TOF peak of fig. 46. We see from fig. 46 that background is negligible, so we simply use the mean of this distribution: $z = +2.3 \pm 0.8$ cm. The error in this value was found from the standard distribution of means from 20 GEANT3 simulations with similar statistics as our case here. We note that this error agrees well with the error found from simply using $\sigma_{mean} = \frac{\sigma_{dist}}{\sqrt{N}} = \frac{57\ mm}{\sqrt{51}} = 8\ mm.$ If we then consider the incident beam energy, energy loss in the target, and the target length (along with the associated errors), we find the resonance energy as

$$E_R^{CM} = 214 \pm 1 \text{ keV}, \tag{17}$$

which is in good agreement with [Pow99]. Note that both here and throughout this work we use atomic masses from [Aud03] to six decimal places.

We now calculate the expected separator TOF, DSSSD energy, and local TOF for ^{25}Al and ^{27}Si recoils based on the energy loss in the target (see eqs. (16) and (19)), our

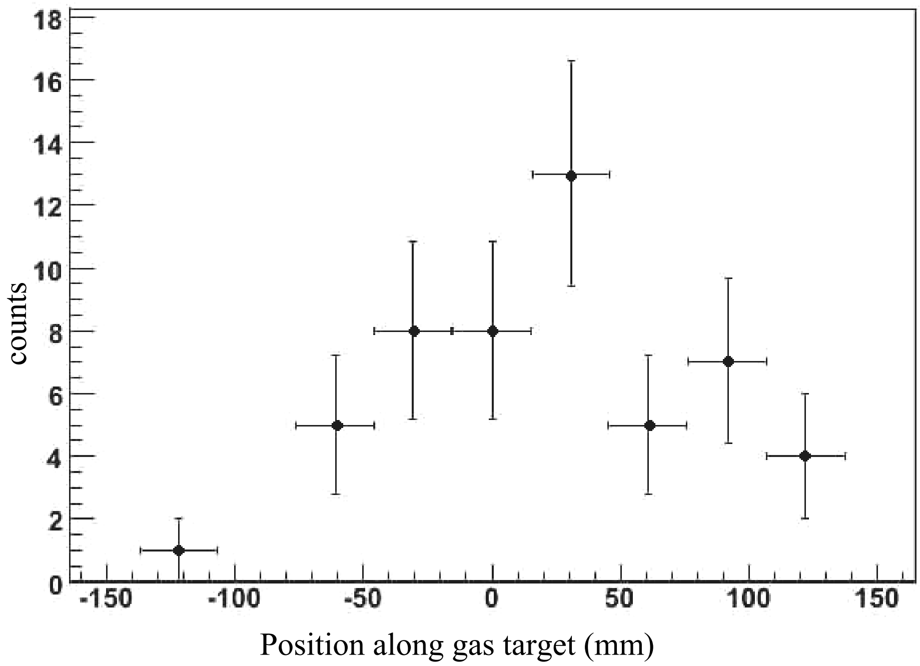

Figure 48: z-distribution of highest-energy gamma-rays ('g0') from the 51 coincidence events of fig. 46. The positions of the BGO detectors are given relative to the centre of the gas target.

measured resonance energies for ^{24}Mg(p,γ) and ^{26g}Al(p,γ) respectively (see eqs. (17) and (20)), the separator length (21.1 m from the centre of the gas target to the DSSSD), the energy loss within the 20 μg/cm^2 carbon foil used with the MCP [SRIM], the distance from the MCP foil to the DSSSD (54 cm), the ~0.4 um dead layer of the DSSSD [Wre03a, SRIM], and the pulse-height defect of the DSSSD. These are summarized in table IX.

Table IX: calculated energies and time-of-flights for recoils and leaky beam from ^{24}Mg(p,γ)^{25}Al and ^{26g}Al(p,γ)^{27}Si reactions.

Beam	E_{beam} (keV/u)	Recoils	Separator TOF (ns)	Local TOF (ns)	E_{DSSSD} (MeV)
^{24}Mg	228	^{25}Al	3400	90	3.47
^{26g}Al	197	^{27}Si	3710	98	3.00
^{26g}Al	201	^{27}Si	3670	97	3.09
Leaky Beam					
^{24}Mg	228	-	-	86	3.69
^{26g}Al	197	-	-	94	3.25
^{26g}Al	201	-	-	93	3.35

To account for the pulse-height defect, we have adopted the model of [Mey02]:

$$\begin{aligned} E_{DSSSD} &= E_{dep} - E_{PHD} = E_{dep} - 10^b E_{dep}^a \\ a &= 0.804 + 0.000113 Z^2 \\ b &= -0.462 - \tfrac{1.625}{Z} \end{aligned} \qquad (18)$$

where Z is the atomic number of the ion bombarding the DSSSD, and E_{dep} is the energy of the ion after losses in the dead-layer of the DSSSD.

From table IX we find that ^{27}Si recoils (for either 201 keV/u or 197 keV/u ^{26g}Al beams) have a separator TOF ~300 ns longer than ^{25}Al, so we should expect ^{27}Si recoils at channel ~7600 based on the observed position of ^{25}Al recoils in fig. 46. Similarly, we expect ^{27}Si recoils at ~2.4 MeV in DSSSD energy, and channel ~2300 in local TOF. (Note that the TAC measuring local TOF uses a stop from the MCP delayed by ~150 ns. As this is longer than the expected MCP-DSSSD flight time for ^{27}Si and ^{25}Al recoils, we expect slower ions to appear at higher channels in the resulting spectrum. We had measured a dispersion relation of 22.7 ps/ch.) Although the origin of unreacted beam (or 'leaky beam') through to the DSSSD may be somewhat complex, calculations like those in table IX may serve as a guide to predict the separation between ^{26g}Al beam and ^{27}Si recoils in time and energy: we expect a separation of ~0.25 MeV and ~200 channels in DSSSD energy and local TOF respectively. (Separator TOF for leaky beam will depend on random background gamma-rays triggering the BGO array, giving a flat distribution for leaky events.)

ii. $^{26g}Al(p,\gamma)^{27}Si$: recoils

Measurements were made with $^{26g}Al^{6+}$ beams of three energies: 201.0 keV/u, 196.8 keV/u and 225.7 keV/u. Note that the 225.7 keV/u beam was used for an off-resonance measurement. The target held 6 torr of H_2 gas, and the EMS was tuned for $^{27}Si^{4+}$ recoils. The energy loss of the beam ε within the target was measured (using MD1) as

E_{26gAl} = 201 keV/u, ε = 15.5 ± 0.7 keV/u = 85 ± 4 eV/10^{15} atoms/cm^2

E_{26gAl} = 197 keV/u, ε = 15.4 ± 0.7 keV/u = 84 ± 4 eV/10^{15} atoms/cm^2 (19)

E_{26gAl} = 226 keV/u, ε = 16.4 ± 0.7 keV/u = 90 ± 4 eV/10^{15} atoms/cm^2.

The uncertainties in eq. (19) arise from taking the uncertainty in an individual energy measurement as ± 0.5 keV/u; we have also considered uncertainties of ± 0.1 torr, ± 1 K and ± 0.4 cm in the pressure, temperature and effective length of the gas target. For comparison, SRIM2003 gives ε = 89 eV/10^{15} atoms/cm^2 for E_{26gAl} = 201 keV/u. The E_R^{CM} = 188 keV resonance corresponds to E_{26gAl} = 194 keV/u.

The beam currents measured just prior to the gas target (FC4) varied from 0.3 – 0.8 particle-nA; fig. 49 gives some indication of the variation in beam intensity for our ^{26g}Al runs.

Figure 50 shows the separator TOF (coincidence, no cuts) spectra for all E_{26gAl} = 201 keV/u and E_{26gAl} = 197 keV/u runs. The distinct recoil peaks are seen at about channel 7500, in reasonable agreement with that expected from the discussion following table IX. The data at 197 keV/u suffer from less ‘leaky beam’ background than the data at 201 keV/u; see below.

To extract the number of recoils for the on-resonance runs, we relied on cuts in separator TOF and DSSSD energy; figs. 51, 52 and 53 show plots of separator TOF versus DSSSD energy for the two beam energies, with cuts for potential recoils indicated. Note that two

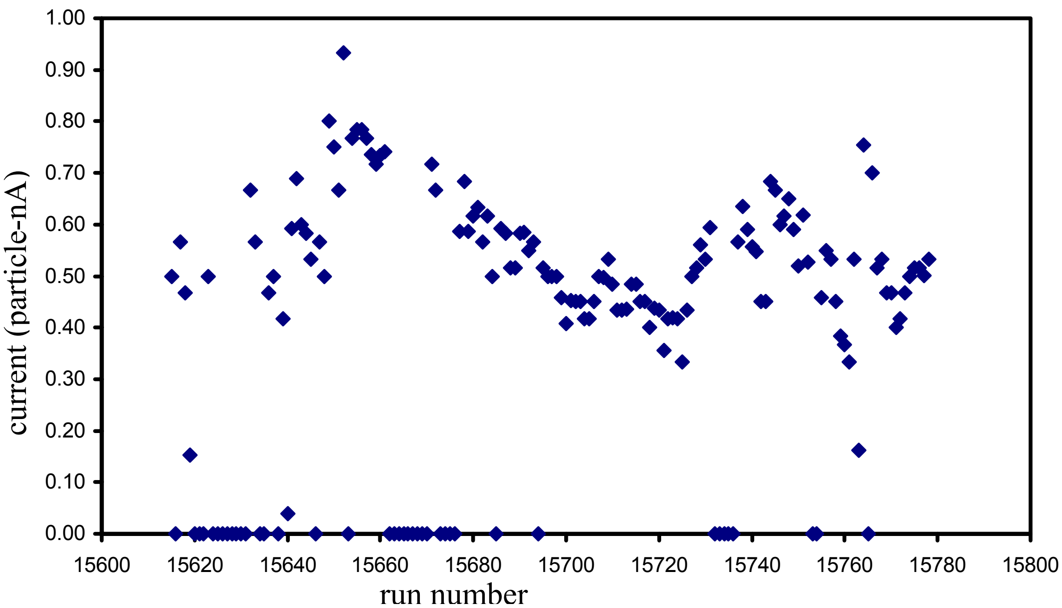

Figure 49: the variation in ^{26g}Al beam intensity measured with the faraday cup FC4 (upstream of the DRAGON gas target and the iris) during the experiment. Each run was ~ 2 hours long. Runs plotted with zero current were test runs.

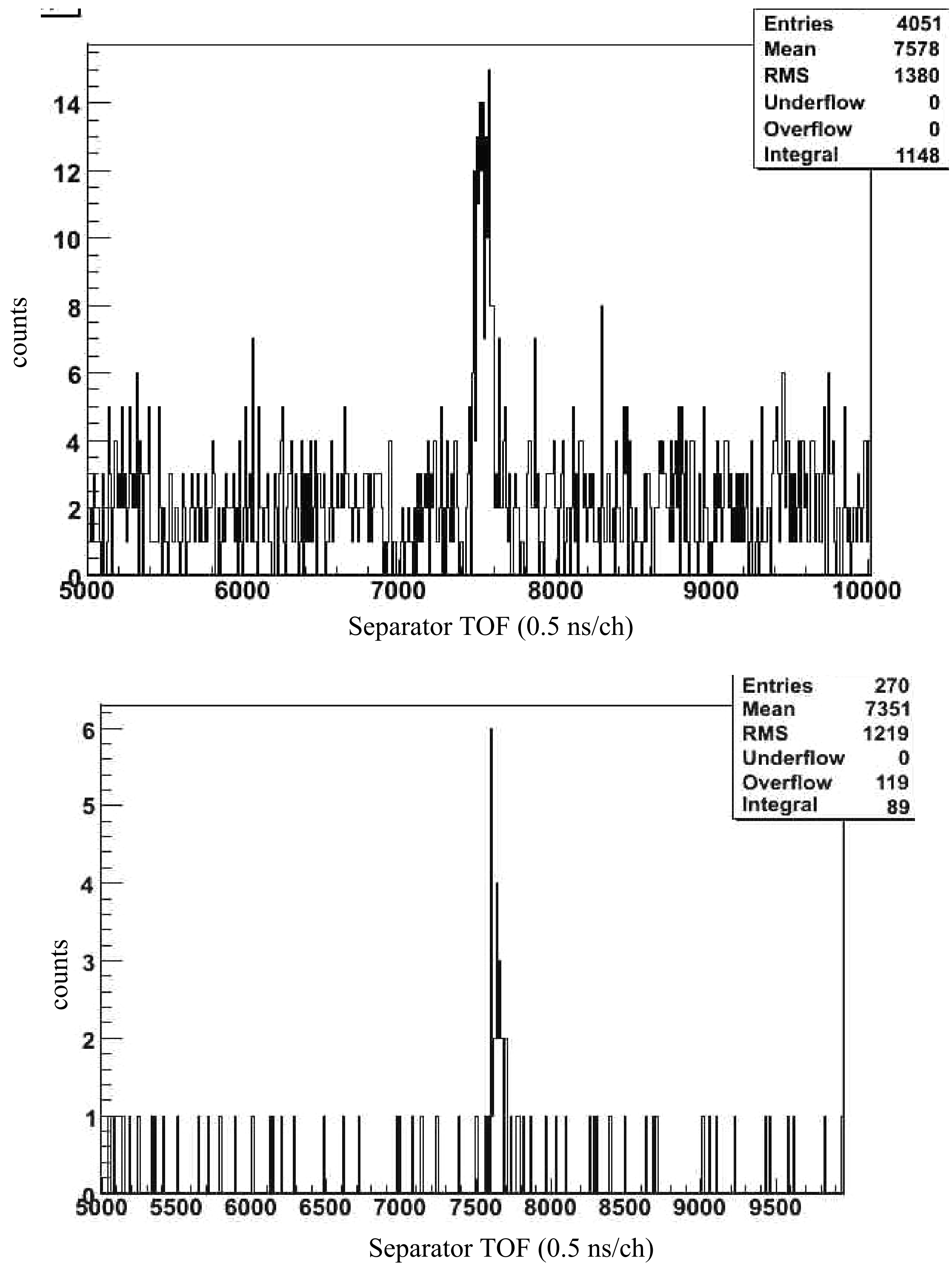

Figure 50: separator TOF spectra for coincidence events in (top) all E_{26gAl} = 201 keV/u runs and (bottom) all E_{26gAl} = 197 keV/u runs. No cuts have been applied to these plots.

cases are shown for E_{26gAl} = 201 keV/u, labeled 'uncooled' and 'cooled'. This is because midway through the experiment we noticed the DSSSD leakage current had risen and we subsequently ran with the DSSSD cooled to -10 °C (see section B, ii, d). This caused a systematic shift in the energies measured by the DSSSD, as can be seen from comparing figs. 51 and 52. A shift of ~30 keV may be expected because of the increased energy required for creating an electron-hole pair in the silicon (see [Cal73], where an energy shift of 0.85 keV/K is observed for 5.5 MeV alpha particles), but the ~350 keV shift seen here cannot be similarly explained, and is not understood. Because of this shift from cooling the DSSSD, the ^{26g}Al data for 201 keV/u were analyzed as two separate cases: '201 keV/u uncooled' and '201 keV/u cooled'. We see that the mean ^{27}Si recoil DSSSD energy of about 2.7 MeV for the '201 keV/u uncooled' case differs from that predicted above. This is likely due to our assumption of a 0.4 μm dead layer for the DSSSD, as well as the pulse-height defect model adopted. A DSSSD dead layer of 0.3 μm seems more likely, based upon the observed ^{27}Si recoil position. The predicted leaky-recoil separation of ~0.25 MeV seems to be reasonable. The 197 keV/u and 226 keV/u runs were all taken with the DSSSD cooled.

To understand the 'leaky beam' background, we relied on cuts in separator TOF versus DSSSD energy in a region of the space far from that of recoils – the background cuts are indicated in figs. 53, 51 and 52. Projections of these 'background' regions onto the DSSSD energy axis were fit with exponentials. We then scaled these 'leaky beam' fits (which used 10000 channels in separator TOF) to agree with the region selected by the recoil cuts (400 channels in separator TOF); fig. 54 shows the leaky fits superimposed on

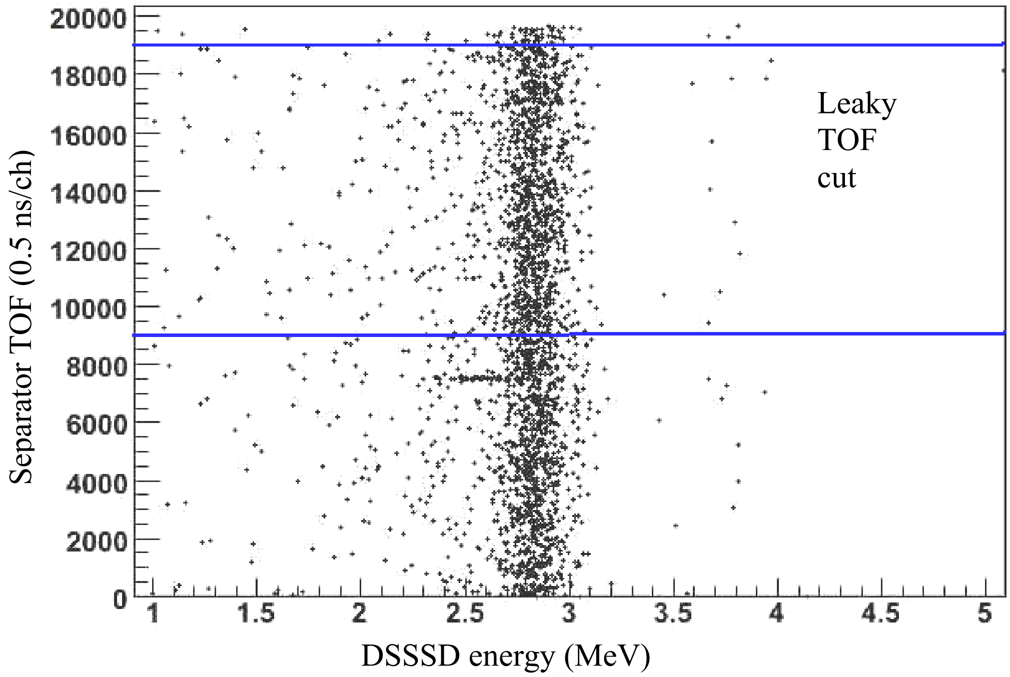

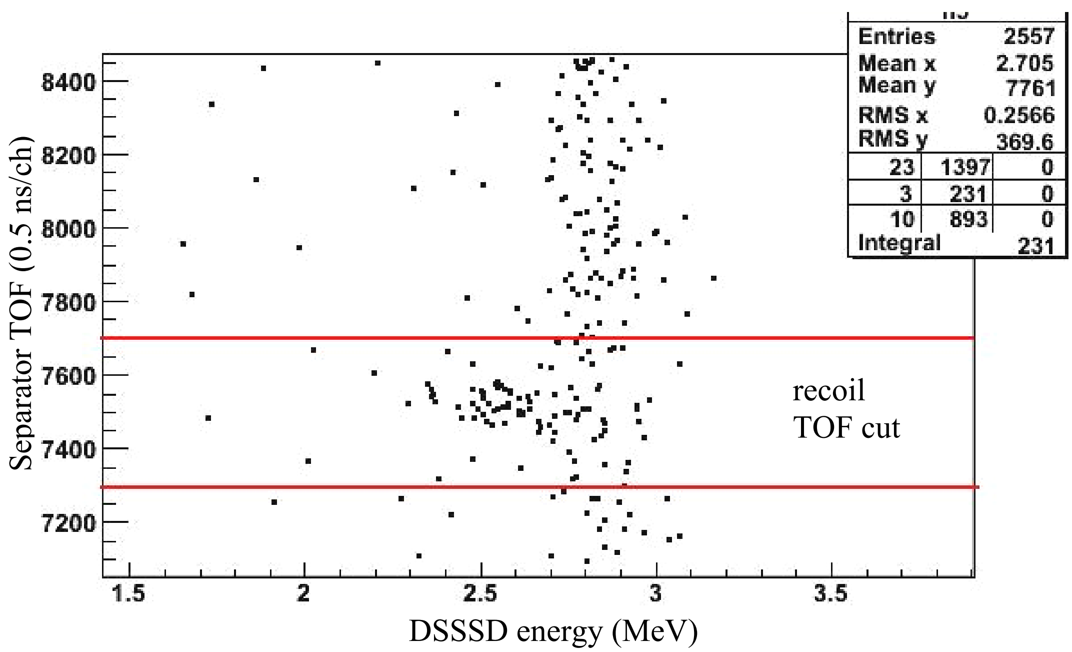

Figure 51: (top) separator TOF vs. E_{DSSSD} spectrum for all E_{26gAl} = 201 keV/u 'uncooled' runs (see text). The 'leaky cut' used to fit the E_{DSSSD} distribution of background is indicated. (bottom) same as (top), but zoomed into the region of potential ^{27}Si recoils. The 'recoil cut' (from which the scaled background was subtracted) is indicated.

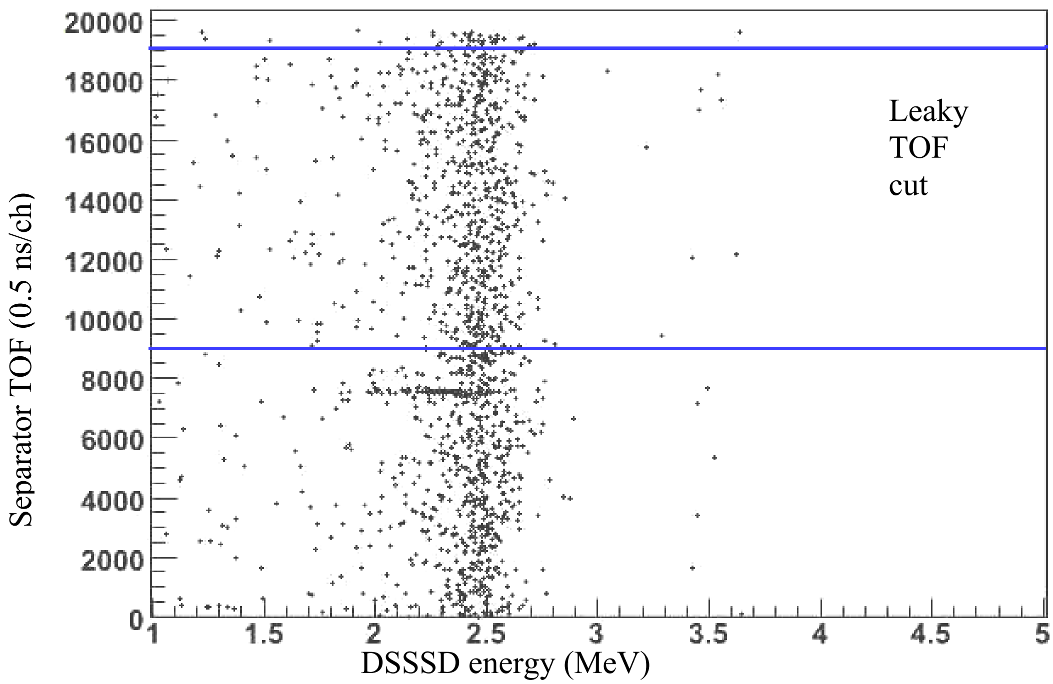

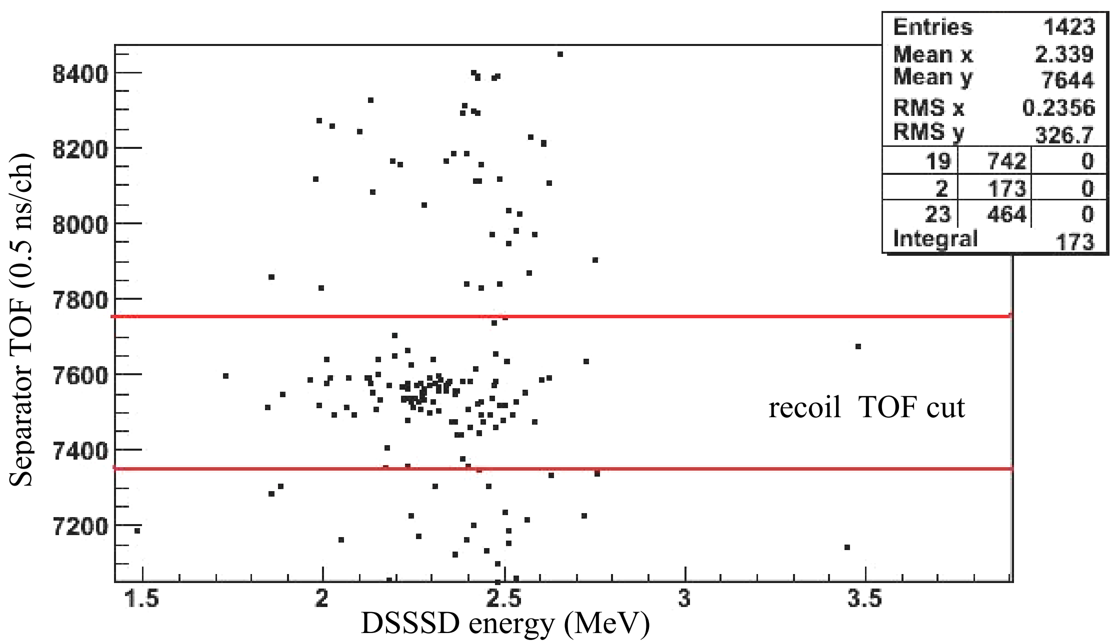

Figure 52: (top) separator TOF vs. E_{DSSSD} spectrum for all E_{26gAl} = 201 keV/u 'cooled' runs (see text). The 'leaky cut' used to fit the E_{DSSSD} distribution of background is indicated. (bottom) same as (top), but zoomed into the region of potential ^{27}Si recoils. The 'recoil cut' (from which the scaled background was subtracted) is indicated.

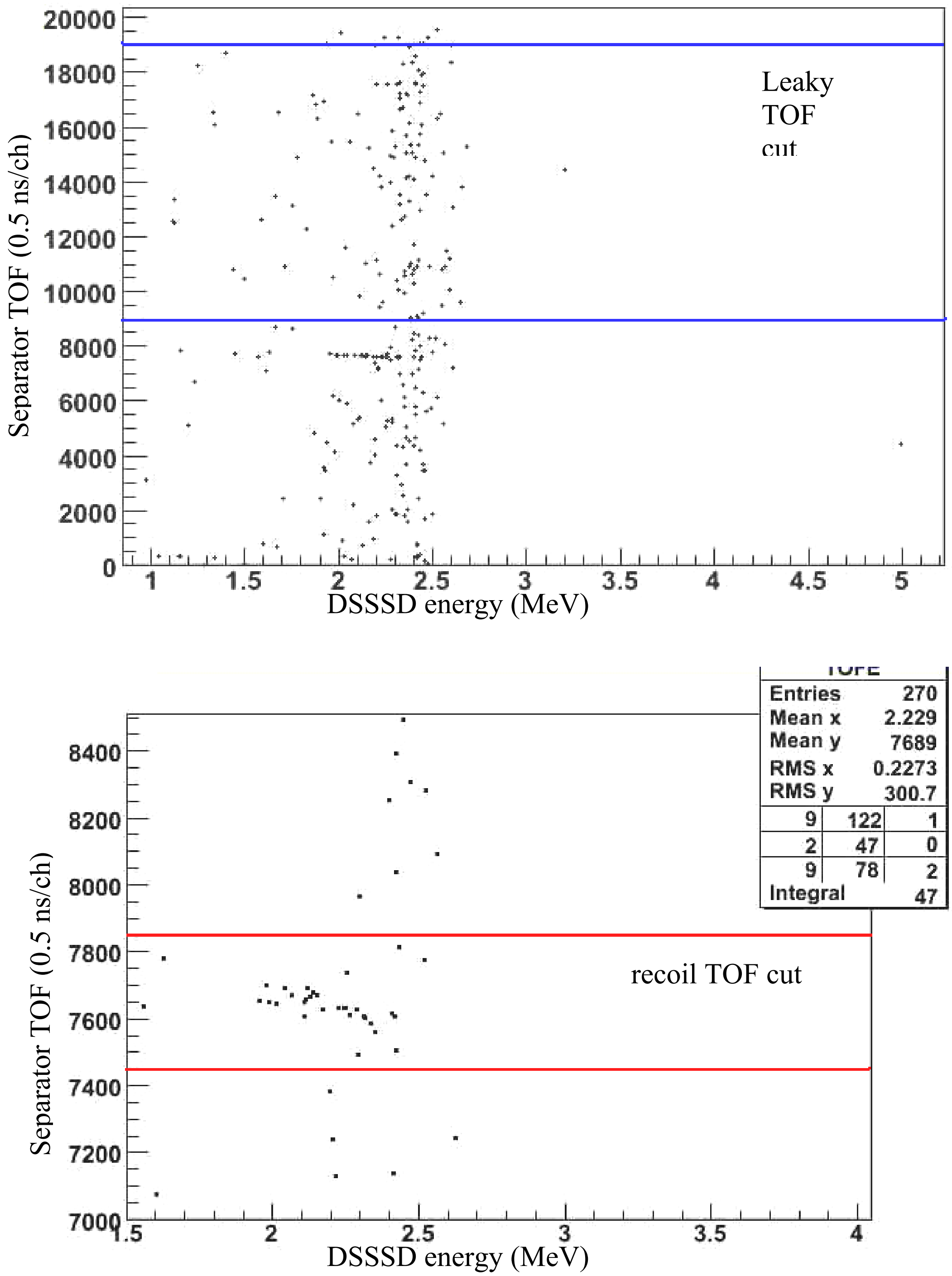

Figure 53: (top) separator TOF vs. E_{DSSSD} spectrum for all E_{26gAl} = 197 keV/u runs. The 'leaky cut' used to fit the E_{DSSSD} distribution of background is indicated. (bottom) same as (top), but zoomed into the region of potential ^{27}Si recoils. The 'recoil cut' (from which the scaled background was subtracted) is indicated.

the recoil region projected onto the DSSSD energy axis. Finally, we integrated the leaky fits over the E_{DSSSD} regions delineated in fig. 54 ('scaled background') and subtracted these values from the 'potential recoil' distributions to obtain the net number of recoils for the three cases. These results are summarized in table X. We note that narrowing the separator TOF recoil cut from 400 to 300 channels, or broadening it to 500 channels, did not have any significant effect on the net number of recoils for the three cases.

Table X: recoils found from the three on-resonance run groups. See fig. 54 and text.

Run Group	Potential recoils	Scaled background	Net recoils
201 keV/u, uncooled	93 ± 10	48.4 ± 0.1	45 ± 10
201 keV/u, cooled	99 ± 10	24.6 ± 0.5	74 ± 10
197 keV/u	31 ± 6	2.6 ± 0.8	28 ± 6

As can be seen from fig. 55, local TOF did not seem to give any enhanced separation between leaky beam and recoils. In addition, the efficiency of the MCP was difficult to gauge. Based on tests with stable $^{26}Mg^{6+}$ beam prior to accepting ^{26g}Al beam, the MCP efficiency was expected to be >97% for the MCP voltages (3100 - 3150 V) and threshold (-50 mV) we used – see table XI. However, while running with ^{26g}Al beam, we found lower and varying efficiencies for V_{MCP} = 3150 V: comparing singles in the MCP with those in the DSSSD, we found MCP efficiencies of 84% (run 15755, see fig. 56) and 91% (run 15691). Comparing the total (coincidence) counts in figs. 53 and 55, we find another estimate of the MCP efficiency as 226 / 270 = 84%. As well, we see that neither the expected position of recoils in local TOF (channel ~2300) nor the expected separation between beam and recoils (~200 channels, see the discussion following table IX) were observed. The former may be explained by the (undocumented) introduction of an

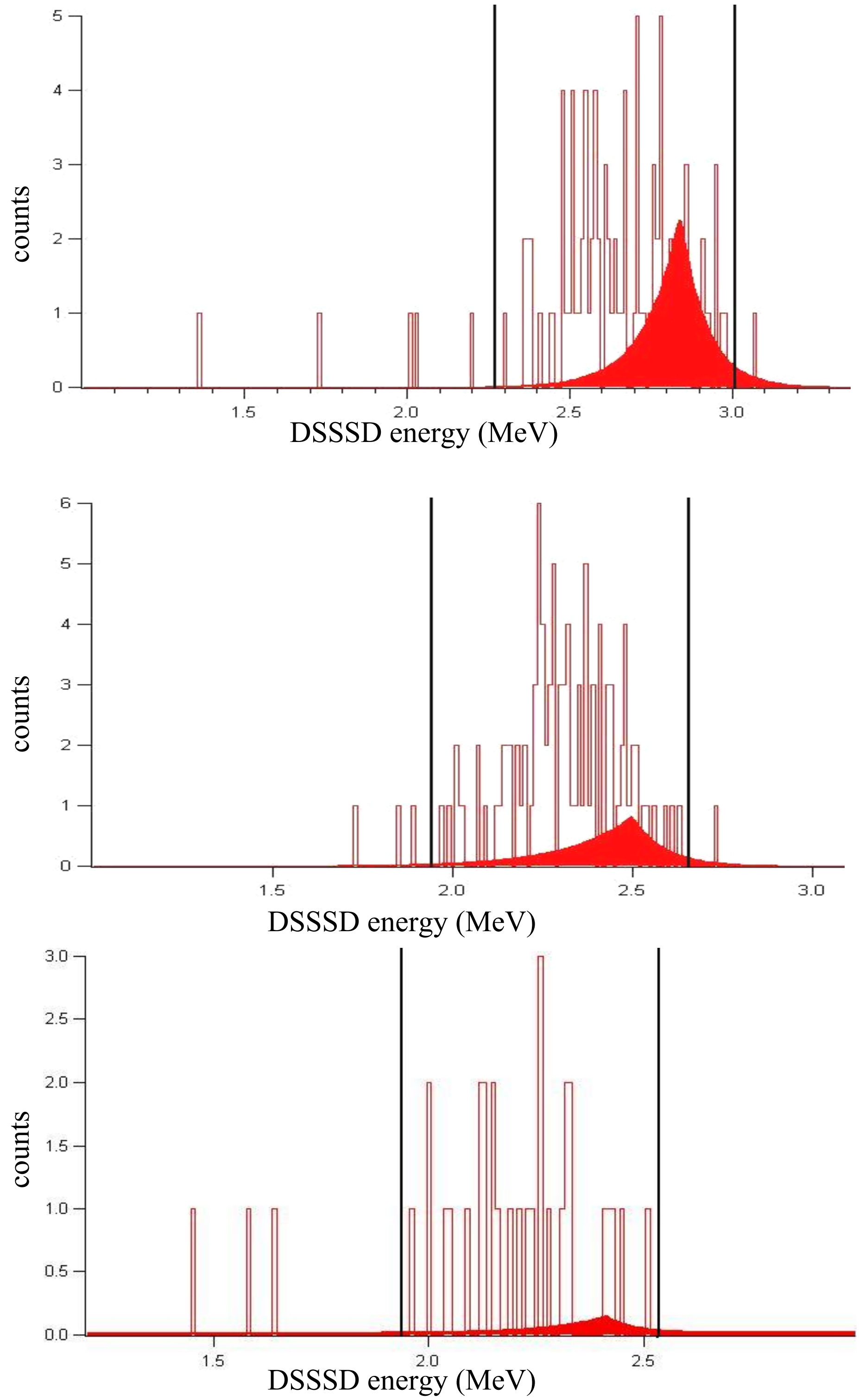

Figure 54: E_{DSSSD} projections for the cuts in figs. 51, 52 and 53. Scaled fits to the 'leaky cut' background are superimposed on the 'recoil cut' region for (top) 201 keV/u uncooled runs (middle) 201 keV/u cooled runs (bottom) 197 keV/u runs. The cuts we used on DSSSD energy are indicated here.

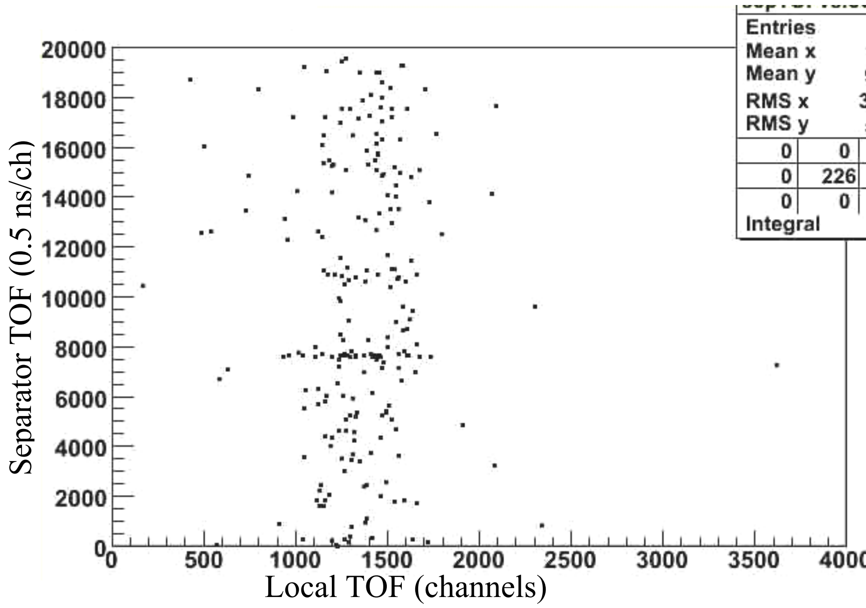

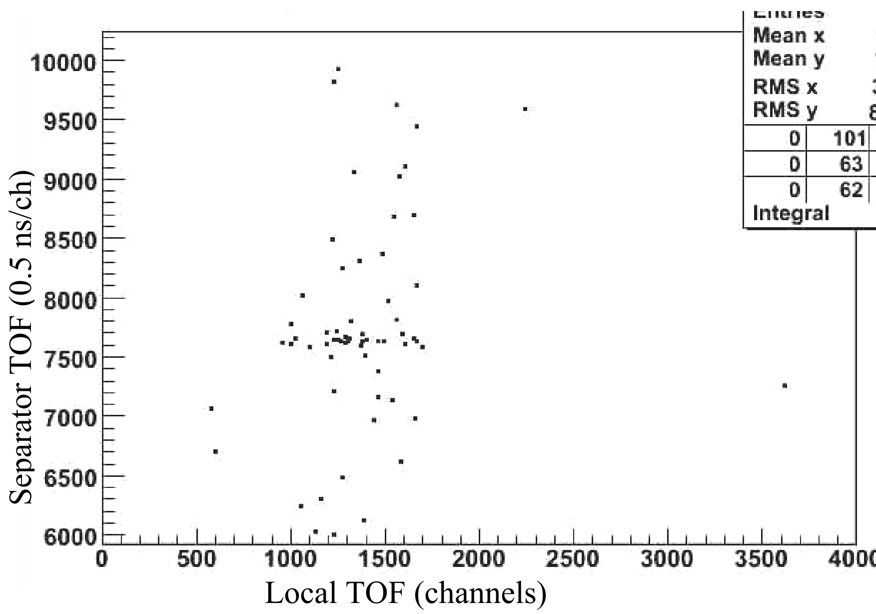

Figure 55: (top) separator TOF vs. local TOF for all E_{26gAl} = 197 keV/u runs. (bottom) same as (top) but zoomed into the region of potential recoils (~ ch. 7500 in separator TOF). Compare with the separation between recoils and leaky beam in fig. 53.

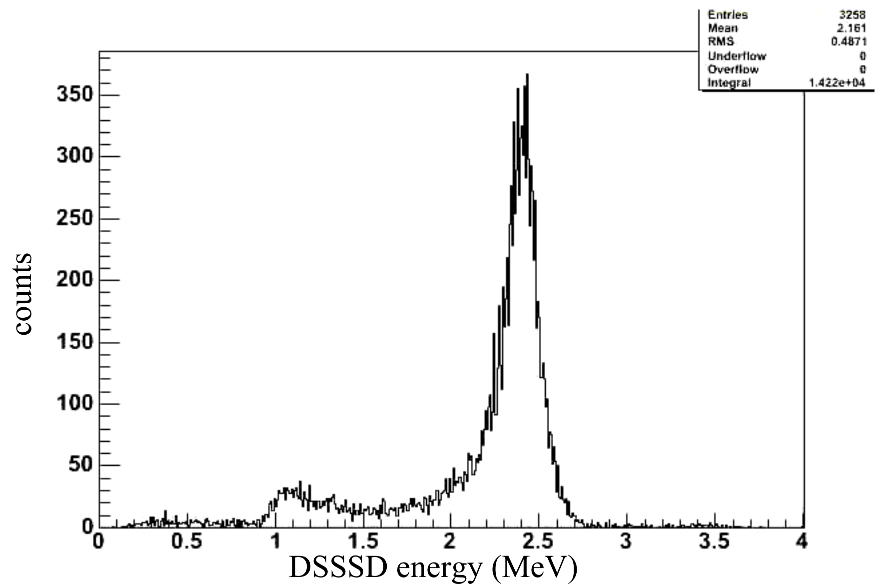

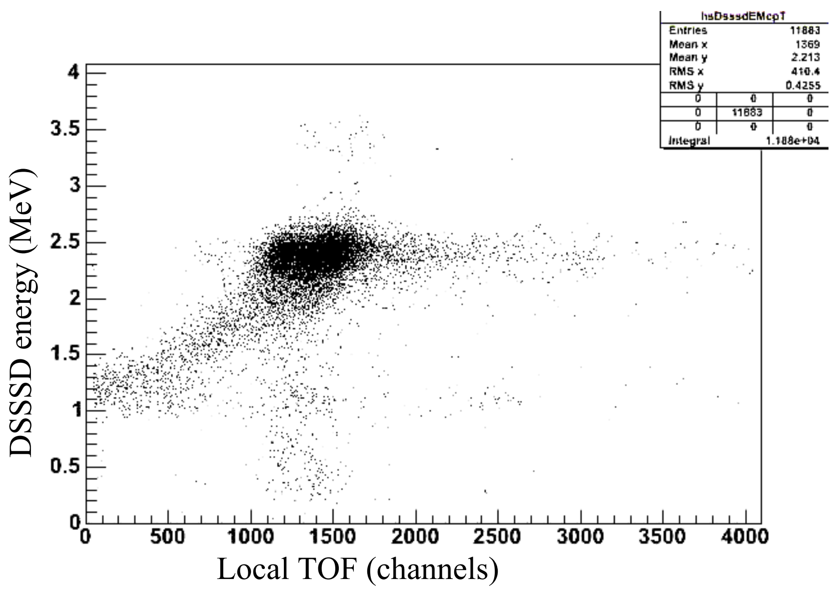

Figure 56: (top) Singles DSSSD energy spectrum (front strips only) for run 15755. (bottom) DSSSD energy vs. local TOF for run 15755 (singles). Comparing the total counts in these plots, we find the MCP efficiency as ~ 84%.

additional delay in the MCP signal to the TAC. The latter may be due to the MCP triggering on noise for much of its livetime. (The MCP triggered at ~5000/s; the DSSSD triggered at ~1/s.) In the interest of introducing as few cuts and efficiencies as possible, we did not use any information from the MCP in the analysis of this experiment.

Table XI: efficiency of the MCP (relative to total hits in the front strips of the DSSSD) as found with ^{26}Mg stable beam. Errors in these values are ~2% from statistics.

	MCP voltage				
	2900	2950	3000	3050	3100
Efficiency (%), threshold = -88 mV	56	83	93	96	97
Efficiency (%), threshold = -50 mV	93	97	97	97	98

For the E_{26gAl} = 226 keV/u off-resonance runs, we extracted confidence bounds for the number of events observed should there actually have been a resonance in ^{27}Si at this energy. If we use the positions of the ^{27}Si and ^{25}Al recoil peaks in separator TOF and E_{DS0SSD} as calibration points, we can use calculations like those in table IX to determine where a resonance for E_{26gAl} = 226 keV/u may appear, if any resonance is traversed within the target for that beam energy. We find that if a resonance is encountered for E_{26gAl} = 226 keV/u, it should appear at channel ~7100 in separator TOF and ~3.0 MeV in E_{DSSSD}. Figure 57 shows the separator TOF vs. E_{DSSSD} spectrum for this beam energy; nothing is seen above background, as expected from the level structure of ^{27}Si. We estimated the level of background in a simpler manner than that used for the on-resonance runs. The 'recoil' cut for fig. 57 used a 400-channel range in separator TOF centered upon channel 7100, and a DSSSD energy range of 2.5 – 3.3 MeV; the

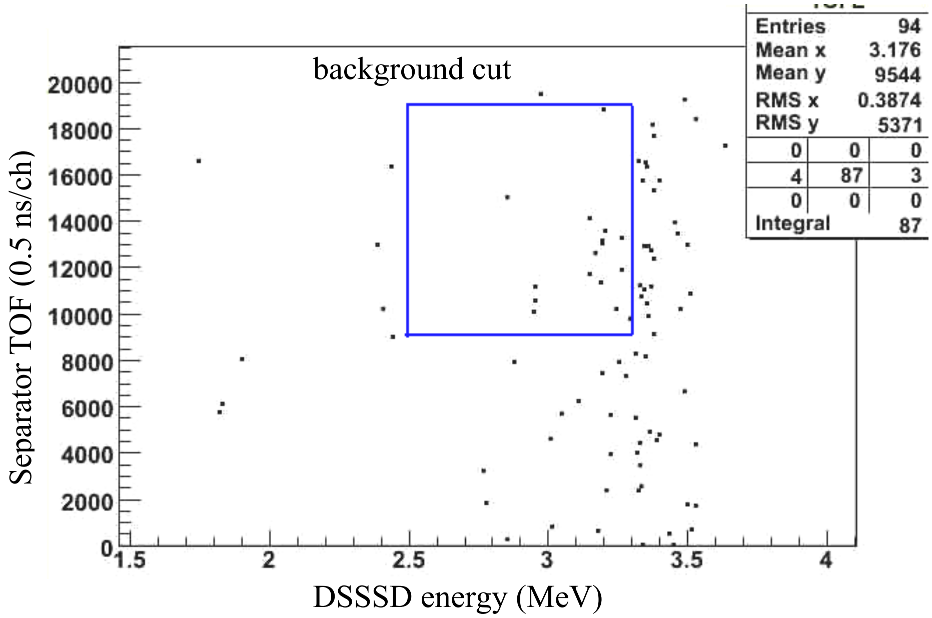

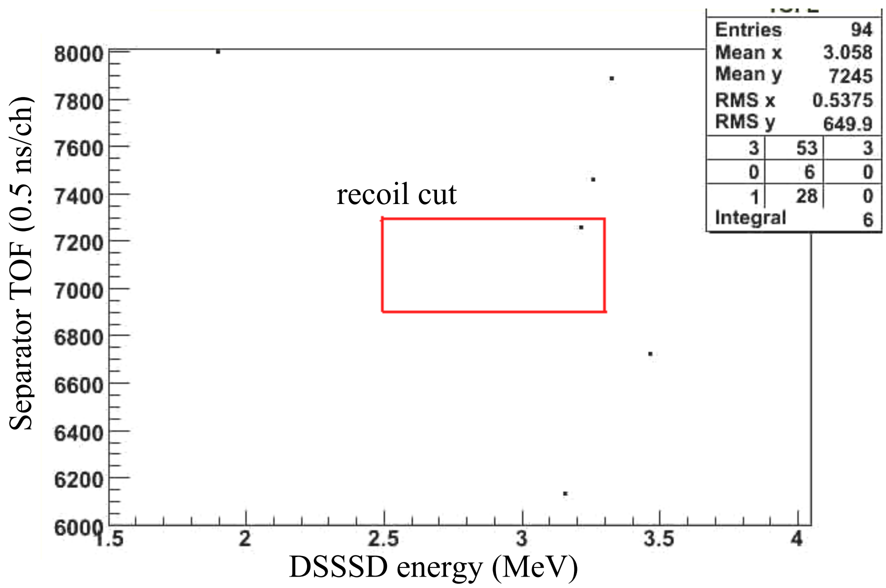

Figure 57: (top) separator TOF vs. E_{DSSSD} spectrum for all E_{26gAl} = 226 keV/u runs. The 'leaky cut' used to fit the E_{DSSSD} distribution of background is indicated. (bottom) same as (top), but zoomed into the region of potential ^{27}Si recoils. The 'recoil cut' (from which the scaled background was subtracted) is indicated.

‘background’ cut used a 10000-channel TOF range away from the ‘recoil’ range, and the same DSSSD energy range as that used for the ‘recoil’ cut. With 1 count in the recoil cut and 16 in the background cut, we simply took the background in the recoil cut as 16(400/10000) = 0.64 events. We relied on the treatment of errors for low-statistics Poisson processes with background as given in [Fel98]. As such, we find that the true number of recoils observed in 68% and 90% of experiments would be 0 – 2.11 and 0 – 3.72 respectively.

iii. <u>Resonance energy</u>

Since the detectors of the BGO array are arranged about the gas target (see fig. 37), the z-position of a resonance in the target (and hence the resonance energy) may be determined by examining the distribution of detectors triggered (for coincidence events). Since it is clear from fig. 53 that the ^{26g}Al(p,γ) data for E_{26gAl} = 197 keV/u has the least amount of background, we chose this set of data to find the resonance energy.

Figure 58 shows the distribution in z (i.e. along the gas target, with z = 0 mm corresponding to the target centre) of ‘leading gammas’ (highest-energy gamma-rays measured) for the 31 potential recoils from these runs. Figure 58 also shows the same for the background of fig. 53 (using the 10000 channel TOF cut in fig. 53 and the E_{DSSSD} cut from fig. 54). We expected 2.6 ± 0.8 (scaled) background events within the recoil cut for this data set (see table X). Since the background level is so low, we use a simple method for extracting the mean z of the ‘pure recoil’ distribution: we subtract the mean of the background z distribution (weighted for 2.6 ± 0.8 events) from the mean of the z distribution for potential recoils. This gives the mean of the 'pure recoil' z distribution as –0.8 mm. The uncertainty in this value was found as ± 9 mm from performing multiple low-statistics GEANT3 simulations of the BGO array. This uncertainty is reasonable considering the naïve error in the mean that one might obtain from simply using $\frac{RMS}{\sqrt{N}}$ (= 13 mm for the distribution of fig. 58).

Adopting z = -1 ± 9 mm for the position of the resonance in the gas target, we find the resonance energy as

$$E_R^{CM} = 184 \pm 1 \text{ keV}, \tag{20}$$

where we have used 15.4 ± 0.7 keV/u for the total energy loss of the beam in the gas target (eq. (19)). This value should be compared with the resonance energy from the direct measurement of [Vog89], as well as the energies derived from indirect measurements [Sch86, Wan89] - see fig. 59 and table XII.

Table XII: centre-of-mass resonance energy of the 'E_R^{CM} = 188 keV' ^{26g}Al(p,g) resonance in ^{27}Si. We have used Q = 7462.96 ± 0.16[Aud03] to convert the excitation energy measurements of [Sch86] and [Wan89].

	E_R^{CM} (keV)
[Sch86]	191 ± 5
[Wan89]	188 ± 3
[Vog89]	188.3 ± 1.1
Present work	184 ± 1

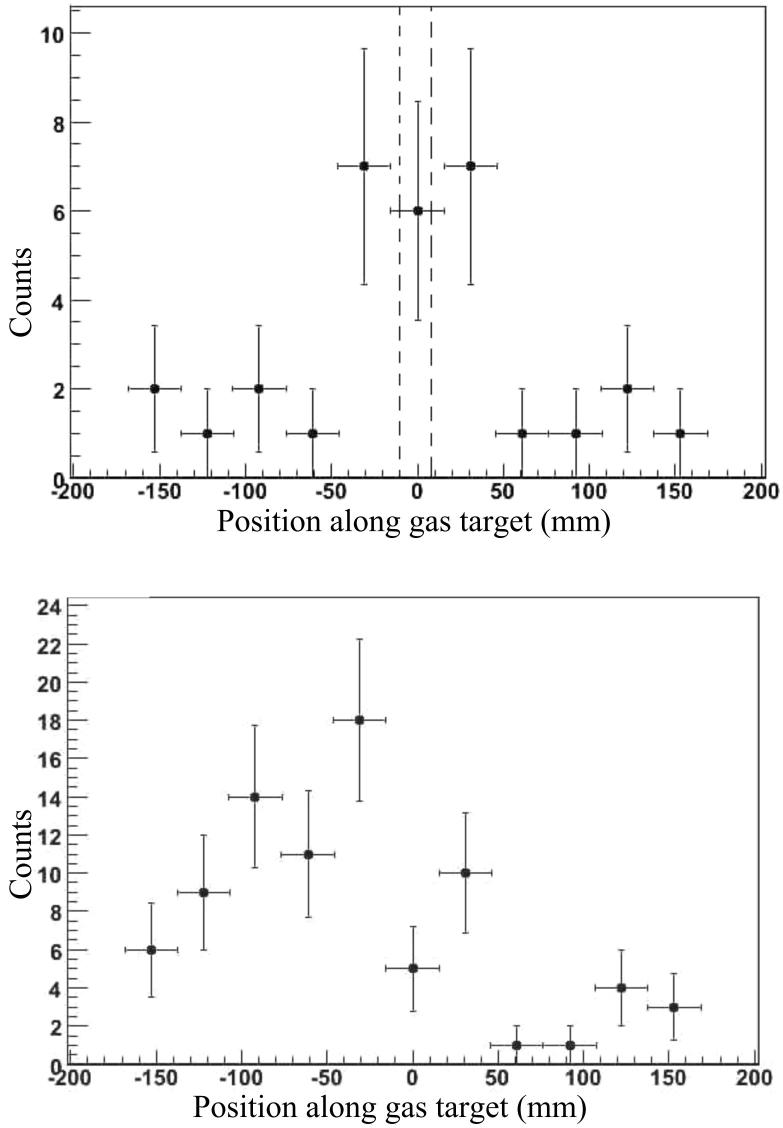

Figure 58: z-distribution of BGO detectors measuring highest-energy gamma-rays ('g0') from the (top) 31 potential recoils of the E_{26gAl} = 197 keV/u runs (found using both separator TOF and E_{DSSSD} cuts) and (bottom) the 82 background events from the same runs (found using a separator TOF cut 25x larger than that used for the recoils, along with the same E_{DSSSD} cut). The positions of the BGO detectors are given relative to the centre of the gas target. The dotted lines in (top) indicate the 1σ bounds of the centroid of the 'true recoil' distribution (see section C, iii).

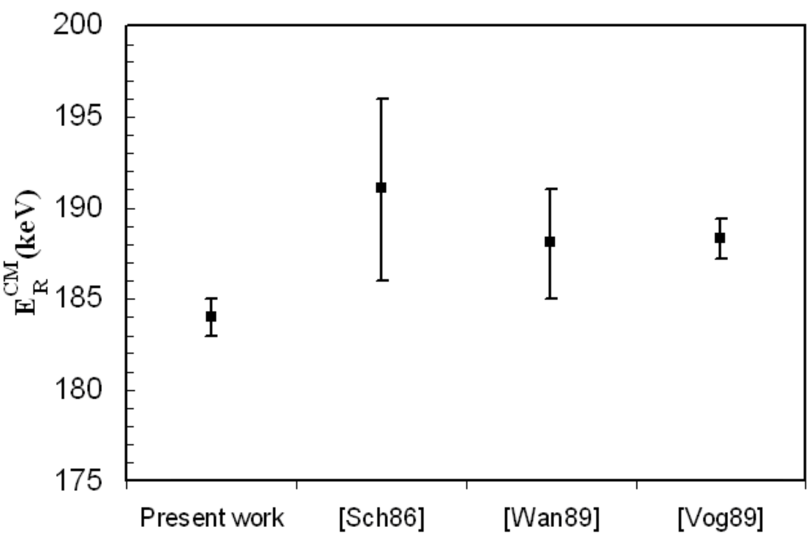

Figure 59: the energy (in the center-of-mass frame) of the nominally E_R^{CM} = 188 keV $^{26g}Al(p,\gamma)$ resonance in ^{27}Si. We have used Q = 7462.96(16) keV [Aud03] to convert the excitation energies measured in [Sch86] and [Wan89] into resonance energies.

iv. <u>Beam</u>

As shown in fig. 49, DRAGON received 0.3 - 0.8 particle-nA of beam as measured by the faraday cup FC4 just upstream of the gas target - see fig. 43. There are five faraday cups used by DRAGON as *absolute* monitors of beam intensity: FC4 and FC1, located just upstream and downstream of the gas target, respectively; FCCH and FCM, located just downstream of the charge slits and mass slits, respectively; and FCF, located upstream of the DSSSD. Readings were taken with FC4, FC1, and FCCH at the beginning and end of each 2 - 3 hour run for this experiment. To monitor *relative* beam intensity, DRAGON uses the surface barrier detectors installed within the gas target (see section B, ii, a). These measure elastically scattered protons, the number of which is proportional to the number of incident beam particles and the gas density in the target.

As most of the beam particles entering the EMS should be bent towards and stopped at the left mass slit (following ED2 – see fig. 34), the current on this slit also acts as a good measure of *relative* beam intensity (the slits are not electron-suppressed). The slit is a less reliable monitor, however, as the amount of beam falling upon it will have a dependence on the tune of the beam. Readings from the relative beam monitors were read out and monitored continuously. To obtain the amount of beam, then, we rely on normalizing the readings from the relative monitors to the currents read by the faraday cups. (In principle, absolute determinations of the beam intensity could be obtained using the Rutherford-scattered protons measured by the surface barrier detectors, as the geometry of the target assembly is known. This approach was explored briefly during this experiment, with the expected number of protons differing from the number actually detected by ~ 10%, for the few runs examined. An improved treatment of energy loss in the gas target, as well as more definitive tests may help to resolve this situation.)

Contamination of the ^{26g}Al beam with ^{26}Na and ^{26m}Al was monitored using Ge and NaI detectors respectively, located near the mass slits of DRAGON (see section B, ii, c). Figures 60 and 61 show typical spectra measured by these contaminant detectors during the run. The amounts of ^{26m}Al and ^{26}Na in the beam were determined on a run-by-run basis through the use of the number of coincident triggers in the NaI detectors, and the number of counts in the 1.809 MeV photopeak, respectively. These were both corrected for random events using the results of a background run. The number of contaminant particles could then be determined using

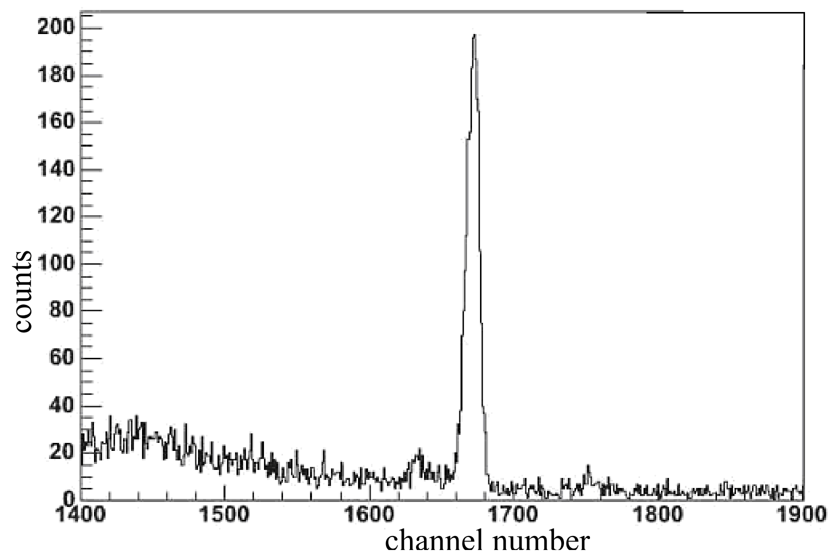

Figure 60: a Ge detector energy spectrum of the 1809 keV photopeak from the gamma-ray emitted in the decay of the beam contaminant ^{26}Na.

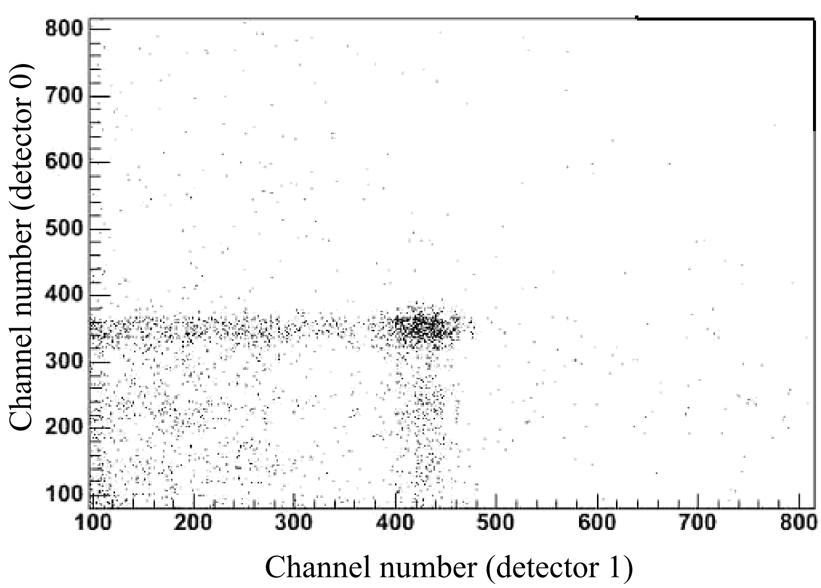

Figure 61: an energy spectrum of coincident events in the two NaI detectors. The intense patch corresponds to 511 keV gamma-rays detected in coincidence from pair annihilation following the beta-decay of ^{26m}Al.

$$N(^{26m}Al) = \frac{NaI\ coincident\ triggers}{\eta_{NaI}\eta_{Al4+}} \tag{21}$$

$$N(^{26}Na) = \frac{1809\ keV\ counts}{\eta_{Ge}\eta_{Na4+}\eta_{\mathrm{int}}}$$

where η_{NaI} and η_{Ge} are the detector efficiencies from eqs. (12) and (13); $\eta_{int} = 0.991$ is the intensity of the 1.809 MeV gamma-ray given the beta-decay branching of ^{26}Na and the gamma-decay branching in ^{26}Mg. The charge state fractions η_{Na4+} and η_{Al4+} for $^{26}Na^{4+}$ and $^{26m}Al^{4+}$ (as the EMS was tuned for $^{27}Si^{4+}$ recoils) were taken as 41 ± 1 % and 40 ± 1 % respectively. The former arises from a direct measurement of the sodium CSFs [Liu03] for a beam energy of 200 keV/u, while the latter is based on results from ^{26}Mg CSD measurements we had made prior to receiving ^{26g}Al beam.

Several steps were taken to minimize the ^{26}Na level in the beam, as this species could trigger random coincidences if it decayed either in the gas target or following implantation in the entrance aperture. (The thresholds for the BGO detectors were set to 1.75 MeV.) Contamination levels were minimized through employment of resonant laser-ionization tuned for ^{26}Al (see section B, i), use of the iris (see section B, ii, e), and subtle adjustment of the beam tune between the pre-separator and high-resolution mass separator.

The effect of laser-ionization in increasing the total amount of beam can be seen in fig. 33; LIS provided as much as 22x more beam than surface-ionization alone once both UV lasers were online. The reduction in beam contamination from using the LIS can be seen

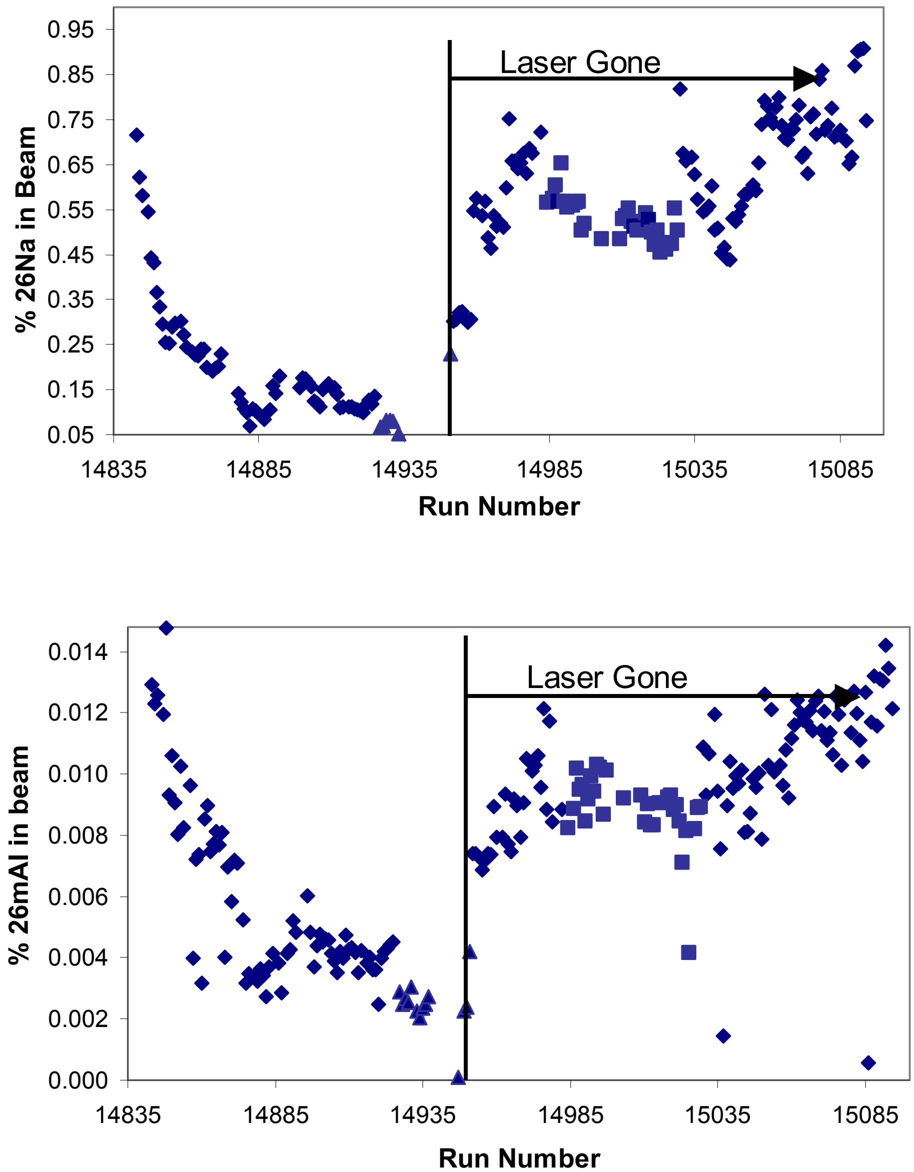

Figure 62: the effect of the laser ionization system on (top) ^{26}Na and (bottom) ^{26m}Al contamination of the ^{26g}Al beam. Note that these plots show data from runs taken during June and July 2005 (see Appendix A), when only one of the two lasers responsible for the resonant ionization was available (λ_{11}, see fig. 32). The iris had not been installed for these runs, nor had any tuning of the beam optics been implemented yet (see text).

from figs. 62; these plots show the effect of the LIS on the ^{26}Na and ^{26m}Al levels in the beam. Note that fig. 62 describes data taken during the ^{26g}Al runs of June/July 2005 (the iris had not yet been installed). As only one of the two UV lasers used for the resonant ionization was available in June/July 2005, the reduction in the contaminant level due to LIS was somewhat more pronounced (by a factor of ~1.5) in the latter runs of October 2005 (when both λ_{11} and λ_{12} were eventually used – see fig. 32).

The effect of the iris on reducing ^{26g}Al beam contamination was checked by examining the rate of singles in the BGO detectors as the iris was closed down, all the while noting the rate of singles in the elastics monitor SB0 (see fig. 35). As the iris was closed from 'wide open' to 3.6 mm in diameter (with 6 torr of H_2 in the target), the rate in the BGO detectors dropped by a factor of ~ 6 (to about 6x the room background rate), with a drop in the SB0 rate of only ~ 40%. From the NaI and Ge contaminant detectors, we expected our beam to be > 99% ^{26g}Al (see table XIII). The results with the iris (which include the effects of LIS) therefore showed that the small number of beam contaminant ions that stopped and decayed in the target made a substantial contribution to the BGO singles rate, and, appeared in a halo about the ^{26g}Al ions. The addition of the iris did, however, make the determination of the number of ions impinging upon the gas target more difficult as it lay between FC4 and the target. As well, the aperture diameter was adjusted several times (between 4 and 5 mm) during the run to optimize its effectiveness. These considerations suggested a slightly different treatment for beam normalization that that used in [Bis03b] – see below.

The effect of the beam tune (upstream of DRAGON) in reducing the contaminants was investigated because of odd behavior noted in the singles rate of the BGO array during a series of runs. Discontinuous changes in this rate were correlated to slight (sub-Gauss) changes in the magnetic fields of the pre-separator and HRMS. ISAC operators were able to reproduce the field settings giving the lowest BGO singles rate; indeed, they eventually were able to reduce the BGO singles rate to 1-2 x room background levels (i.e. ~50-100 counts/s) through tuning (in combination with LIS and the iris). With regular adjustments to the tune to account for natural drifts in the magnetic fields of the separators, this technique proved to be quite valuable in suppressing contaminants - allowing the acquisition of the clean 197 keV/u data of fig. 53. An explanation of this may rest upon the idea that the ^{26}Na and ^{26}Al ions may have different phase spaces, as the former is ionized primarily through contact with rhenium, while the latter is ionized primarily through the lasers. If the position and angle of surface-ionized and laser-ionized ions are different, then the quadrupoles following the ion source (which essentially focus ions to the slits following the pre-separator) may image these groups differently. By adjusting the fields of the pre-separator and HRMS, then, we may have just been searching for the laser-ionized group from the ion source. This hypothesis [Bri05] was examined briefly during the course of our experiment, and will continue to be tested in future ISAC beam development periods. Through the use of tuning of the optics, we were able to reduce the ^{26}Na level from 1:36 000 to 1:350 000; the ^{26m}Al level stayed at about 1:30 000 throughout the course of the experiment – see table XIII.

In light of the negligible ^{26}Na contamination level of the beam (given the uncertainty in the number of beam particles – see table XIII) as well as the considerations discussed in section B, i, we did not make a correction for any ^{26}Mg and/or ^{26}Si ions in the beam.

With beam contamination known reasonably well, we could now determine the total ^{26g}Al beam received into the gas target. To mirror the analysis of the recoils, the runs were subdivided into four groups: 201 keV/u 'uncooled', 201 keV/u 'cooled', 197 keV/u, and 226 keV/u.

As the iris limited the transmission of beam measured by FC4 into the target (see fig. 43), we chose to use the readings from FC1 as our absolute monitor of beam intensity. This, however, required knowledge of the average charge state q_{av} of the beam after passing through the gas target. Once q_{av} is known, it can be used with FC1 to provide an absolute, *transmission-independent* normalization for the relative monitors. We determined q_{av} as follows: with no gas in the target, the currents I_{FC1*} and I_{FC4*} were measured; these currents were again measured with 6 torr of H_2 in the target as I_{FC1} and I_{FC4}. We can then calculate q_{av} as

$$q_{av} = q \frac{I_{FC1}}{I_{FC4}} \frac{1}{T} \tag{22}$$

where $T = (I_{FC1*} / I_{FC4*})$, and $q = 6^+$ is the charge state of the beam prior to entering the target. We found

$q_{av} = 3.24 \pm 0.03$, with $T = 91\%$. (23)

The uncertainty in q_{av} arises from the uncertainty in the faraday cup readings. We used the scatter of I_{FC1}/I_{FC4} ratios for all the runs in the 201 keV/u cooled run group (during which q_{av} was measured) to minimize the contribution of the uncertainty in this ratio to the uncertainty in q_{av}.

With q_{av}, we could now normalize either the integrated current on the left mass slit (LMS) or the total number of scattered protons to FC1 for any particular run within the four groups.

With the LMS data, we used the expression

$$N_{LMS} = \frac{L_{av}^{*} Q}{q_{av} e} \frac{t_{live}}{t_{real}} \tag{24}$$

where N_{LMS} is the number of particles impinging on the gas target for a run, Q is the integrated charge (in C) on the left mass slit during the run (see fig. 63), and (t_{live}/t_{real}) is a correction for the fact that Q is found in the realtime of the system, and we desire N_{LMS} in the livetime of the system (as the recoil analysis was in livetime). This livetime correction was determined through the ratio of acquired-to-presented 'tail' triggers (i.e. triggers to the DSSSD and/or SB0) as measured by two scalers during a run, and was about 0.96. We now discuss the factor L_{av}* in eq. (24). The normalizing factor $L = FC1/I_{LMS}$ (with both currents in eA) was calculated for LMS values at the beginning and end of each run. These were then averaged to give L_{av} for each run. The values of L_{av} were then used to find an average normalizing value L_{av}* for each of the four run groups. For each run, then, the appropriate value of L_{av}* was used with eq. (24) to find N_{LMS}.

With the elastic monitor (SB0) data, the first step relied on determining S_0, the number of elastically scattered protons per particle-C of beam:

$$S_0 = \frac{(N_p / \Delta t)}{I_{FC1} / q_{av}} \tag{25}$$

where N_p is the number of scattered protons in the time interval Δt at the beginning of a run, and I_{FC1} is the FC1 current measured at the beginning of a run. Figure 64 shows a typical elastic proton peak; N_p was chosen as the number of counts in this peak for the first 150 *time* bins. Each time bin corresponded to about, but not exactly, 2 s because of a bug in the MIDAS acquisition system (identified and fixed after our experiment). We determined the correction by averaging the ratio of run duration-to-scaler bins for all the runs; we found 1 scaler bin = 2.0922 ± 0.0006 s. We could then find the Δt corresponding to our N_p.

For each run group, an average value of S_0, S_{0av}, was found. The number of particles impinging on the gas target N_{SB0} for any run could then be found as

$$N_{SB0} = \frac{N_p^{tot}}{S_{0av} e} \frac{t_{live}}{t_{real}} \tag{26}$$

where N_p^{tot} is the total integral (i.e. all time bins) of the elastically scattered proton peak for a run. The same livetime correction factor discussed above is also present in eq. (26), but it is used here to correct for how I_{FC1} in eq. (25) is the realtime FC1 current.

The run-by-run values of N as given by the two methods, as well as the normalization constants L_{av}* and S_{0av} used for each run group, are given in Appendix B. In general, the agreement between the two methods is good to about ± 5%. Because of the dependence of the LMS method on the tune of the beam, as well as how the LMS data was not available for some otherwise acceptable runs (the method for recording data from the LMS was not in place for the beginning of the experiment), we relied on the SB0 method for the number of beam particles impinging on the gas target. Table XIII gives these values as well as the number of contaminant ions for each run group.

Table XIII: Total number of beam particles N_{tot} received in the target (found using the SB0 data – see text) and number of beam contaminant ions N_{26Na} and N_{26mAl}.

Run Group	N_{tot} (x10^{14}) (SB0 method)	N_{26Na} (x10^{10})	N_{26mAl} (x10^{10})
201 keV/u, uncooled	6.1 ± 0.3	1.7 ± 0.2	1.7 ± 0.2
201 keV/u, cooled	9.2 ± 0.3	2.1 ± 0.2	2.8 ± 0.3
226 keV/u	2.9 ± 0.2	0.074 ± 0.007	1.1 ± 0.1
197 keV/u	3.4 ± 0.3	0.10 ± 0.01	1.1 ± 0.1

We estimate the beam suppression S_{sgl} of the EMS alone by taking the ratio of the number of DSSSD singles events (front strips) to the total amount of beam for the 197 keV/u runs. We find:

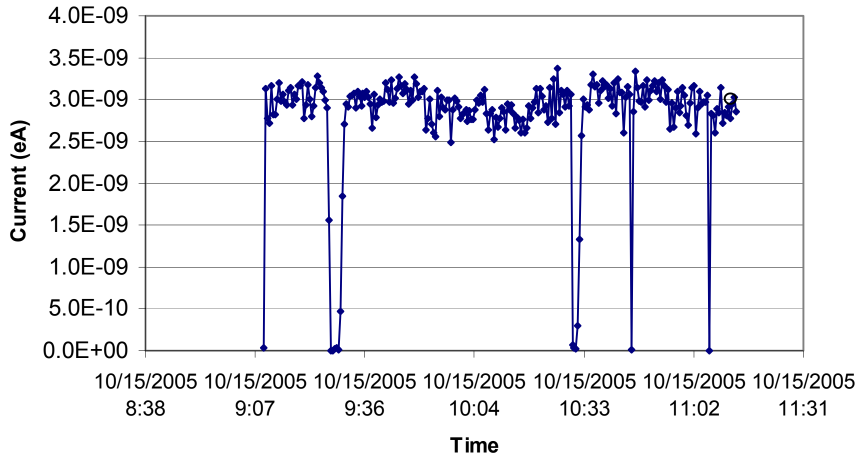

Figure 63: Current read from the left mass slit during a typical run.

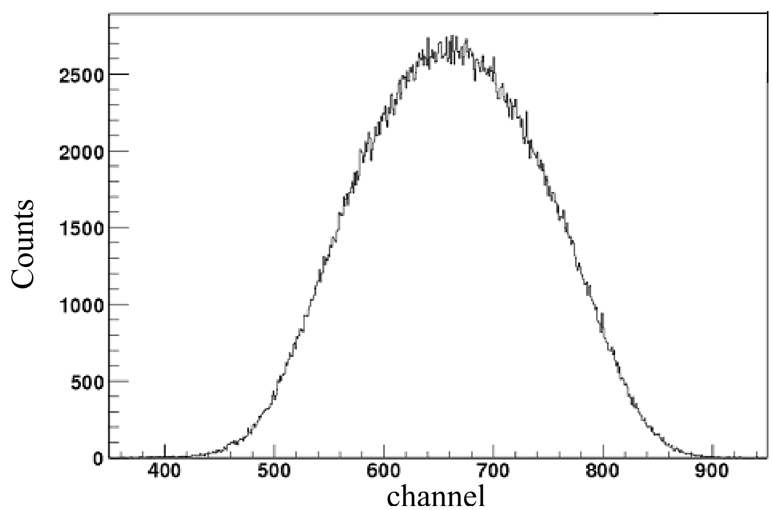

Figure 64: typical energy spectrum of elastically scattered protons as measured by the detector 'SB0' within the gas target.

$$S_{sgl} \sim \frac{1.0\times10^{5}}{3.4\times10^{14}} = 3.0\times10^{-10}.$$

When, however, we include the requirement of coincidence, as well as the additional cuts used on separator TOF and recoil DSSSD energy, we can use the background expected in the cuts on the 197 keV/u runs (see table X) to find S_{coinc}:

$$S_{coinc} \sim \frac{3}{3.4\times10^{14}} = 9\times10^{-15} \;.$$

v. BGO Array Efficiency

Since we relied on coincidences between detection in the BGO array and the DSSSD to identify ^{27}Si recoils, we need to know the efficiency of the BGO array. The gamma-decay scheme for the ^{26g}Al+p resonance at 'E_R^{CM} = 188 keV' (we use quotes in light of our measurement in eq. (20)) has been measured by [Vog89]; five different gamma cascades may be expected – see fig. 36 and table XIV. A trigger threshold on the BGO detectors of about 1.75 MeV was implemented during the experiment to help discriminate against false coincidences; this hardware threshold represented the minimum energy required of the highest-energy gamma-ray in a cascade (g0, also called the "leading-gamma") to allow *all* other cascade radiation to be registered. Note that this energy threshold was found to be 'soft' rather than 'sharp' – the percentage of accepted leading-gammas rose gradually from 0% at E_{g0} = 0 MeV to 100% at E_{g0} ~ 2.2 MeV (see fig. 65).

Figure 65 shows both the leading-gamma energy distribution for potential recoils for the 197 keV/u runs, and, a room background (singles) g0 distribution. The soft threshold is evident in the background distribution; we also see that it should not have interfered with the detection of the majority of leading-gammas from $^{26g}Al(p,\gamma)^{27}Si$ reactions (compare fig. 47).

The BGO array efficiency was found by simulating 5000 gamma-decays of the 'E_R^{CM} = 188 keV' resonance in GEANT3 (taking into account the branching ratios of fig. 36), adding to the g0 distribution output by GEANT3 the effect of a function fit to the soft threshold, and then comparing the number of leading-gammas remaining to the total number of decays simulated. A detailed account of the GEANT3 simulation used for determining the efficiency of the BGO array can be found in [Gig04]. (See also [Gal03] and [Cra05] for the incorporation of BGO detector resolution to this simulation.)

Table XIV: gamma-ray cascades expected from the 'E_R^{CM} = 188 keV' resonance in $^{26g}Al(p,\gamma)^{27}Si$.

Cascade	Probability (%)	g0 (MeV)	g1 (MeV)	g2 (MeV)	g3 (MeV)
7651→4447→2164→0	80.10	3.205	2.284	2.164	--
7651→4447→2910→2164→0	0.59	3.205	1.538	0.746	2.164
7651→4447→2910→0	9.31	3.205	1.538	2.910	--
7651→2910→0	9.40	4.743	2.910	--	--
7651→2910→2164→0	0.60	4.743	0.746	2.164	--

Different possible angular distributions (isotropic, dipole, quadrupole) for the gamma-ray from the E_x = 7.651 MeV state in ^{27}Si (i.e. the 'E_R^{CM} = 188 keV' ^{26g}Al+p resonance) were assumed as the spin-parity of this state is unknown. To understand the level of our dependence on the gamma-decay branching ratios from [Vog89] for this state (see fig.

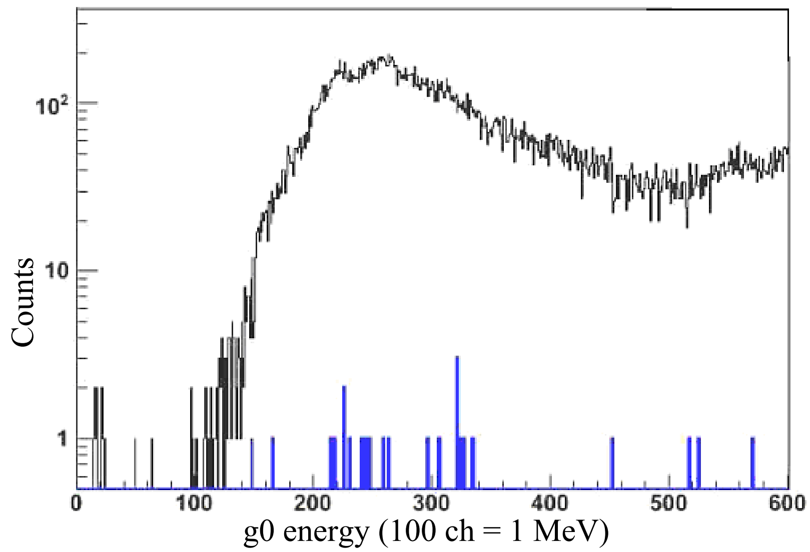

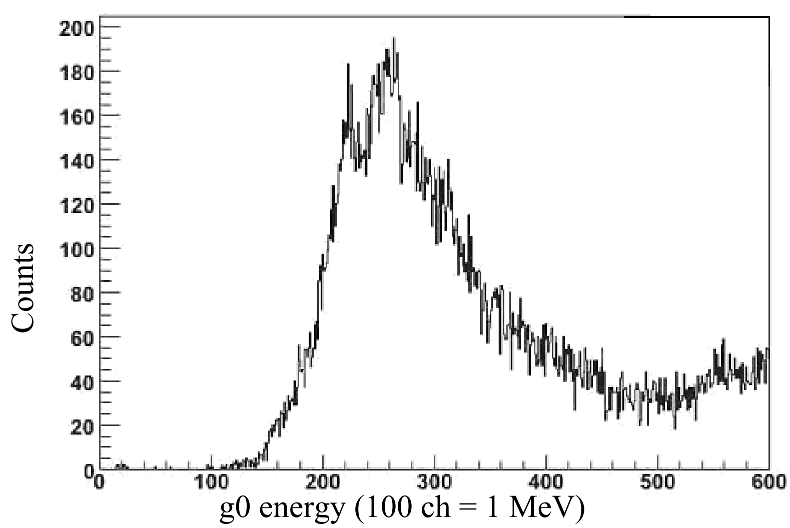

Figure 65: (top) highest-energy gamma-rays (g0) detected from potential recoil events from the E_{26gAl} = 197 keV/u runs (blue). These are superimposed on singles g0 events from a background run. (bottom) The same singles g0 events as in (top), but shown on a linear scale to highlight the location of the 'soft' trigger threshold on the BGO detectors. Note that 10 channels (= 100 keV) were added to the raw data stream for the BGO signals; absolute energies read from the above plots must be corrected accordingly.

36), we repeated the efficiency calculations for different branching ratios. The three variations considered are shown in fig. 66; these cases were chosen as they alter the intensities of those gamma rays most likely to be affected by the threshold (i.e. the 2.284 and 2.164 MeV gamma-rays).

The uncertainty in the final efficiency η_{BGO} includes uncertainty from the different possible angular distributions of the gamma-ray from the E_x = 7.651 MeV state, from variation of the branching ratios, and from the fit to the threshold. The dominant source of uncertainty is, however, the 10.3% global *relative* error in the GEANT3 simulation [Gig04] (see section B, ii, b). Considering all of these sources, we find

$$\eta_{BGO} = 76.4 \pm 10.0\ \%. \tag{27}$$

vi. Silicon charge state distribution

As we had tuned the EMS for the 4^+ charge state of ^{27}Si, it was necessary to know what fraction of all ^{27}Si charge states this represented. For this purpose, we made a charge state distribution measurement using DRAGON and a stable silicon beam. The off-line microwave ion source was used in concert with silane (SiH_4) gas to provide a $^{28}SiH_3^{1+}$ beam (other choices of beam were observed to have high levels of ^{14}N contamination). This beam was sent through the RFQ and the stripper foil, after which a beam of A/q = 5.6 (i.e $^{28}Si^{5+}$) was selected and accelerated to DRAGON. The ^{28}Si beam energy was chosen to have a similar *velocity* [e.g. Liu03] as a ^{27}Si recoil would have in the 6 torr gas target given our measurement of the resonance energy. (For a ^{26g}Al beam of 197 keV/u

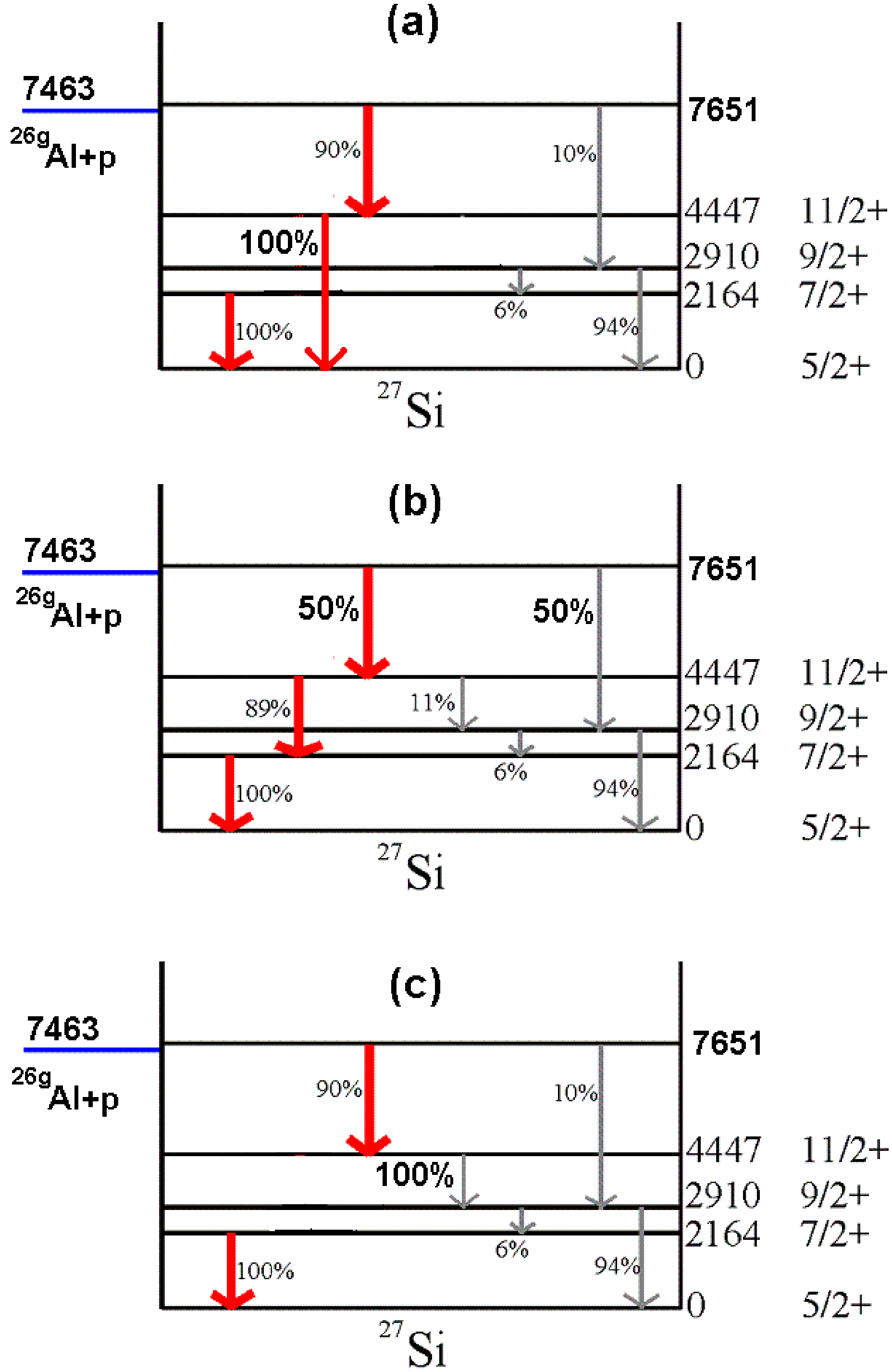

Figure 66: gamma-decay branching variations used in GEANT3 simulations for the efficiency of the BGO array. Compare fig. 36.

and a resonance in ^{27}Si at E_R^{CM} = 184 keV, ^{27}Si recoils would have a lab energy of 175 keV/u and a velocity of 5.82 x 10^6 m/s). The energy of the ^{28}Si beam was measured with MD1 as 179 keV/u (= 5.88 x 10^6 m/s), and it was tuned through the EMS. The *A/q* of the beam was verified using eq. (11) to within 0.5%. As a final check to ensure the beam was $^{28}Si^{5+}$ (and not, say, $^{17}O^{3+}$, with *A/q* = 5.67), the beam was directed into the DRAGON ionization chamber. The IC was operated with a 15 μg/cm^2 SiN entrance window and 8 torr of isobutane for this measurement. Figure 67 shows the subsequent energy loss data; the beam is seen to lose about 2/3 of its energy in the first anode. This is consistent with calculations for a ^{28}Si beam – a ^{17}O beam is expected to lose much less. As well, no separate contamination peak can be seen in the ΔE-E spectrum.

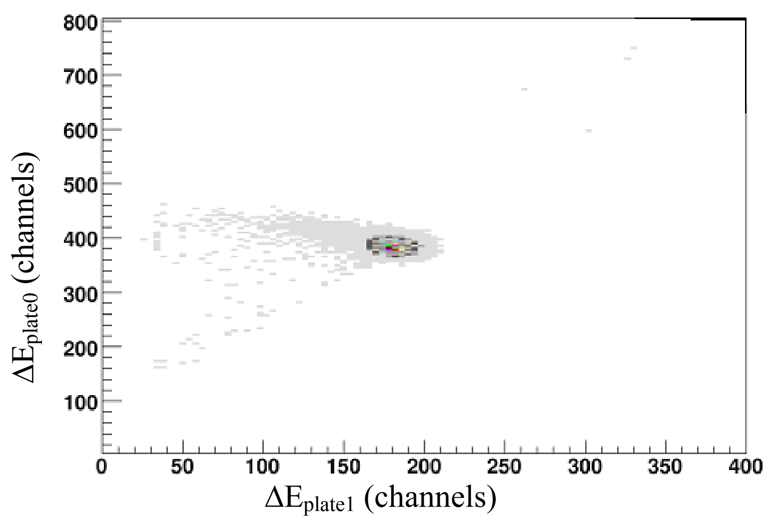

Figure 67: Energy spectrum resulting from the $^{28}Si^{5+}$ beam in the DRAGON ionization chamber. See fig. 41.

Reasonably confident in the nature of the beam, we then measured the CSD of ^{28}Si at several target pressures to check whether or not charge state equilibrium in the gas was at all an issue. From experimental data at E_{beam} = 200 keV/u in [Liu03], the critical thickness (defined as the target thickness where all charge states are within 5% of their equilibrium populations) was found to be $\lesssim 2 \times 10^{17}$ atoms/cm^2 for beams of ^{23}Na and ^{24}Mg (initial charge states 3+ - 6+) in H_2 ($v_{beam} \sim 6.2 \times 10^6$ m/s). For 1 and 6 torr of H_2 in our 12.3 cm target, 2×10^{17} atoms/cm^2 is equivalent to 3.1 and 0.5 cm, respectively. This critical thickness was noted in [Liu03] to increase 'slightly' with increasing Z_{beam} (for a given v_{beam}). Even given this, the above calculation suggests that charge state equilibrium should be achieved for both a E = 179 keV/u ^{28}Si beam traversing the entire 12.3 cm gas target for P $\gtrsim$ 1 torr, and, for E = 175 keV/u ^{27}Si recoils traversing half of the gas target at P = 6 torr.

As OLIS was unstable at the relatively high voltage (63 kV) needed to extract the $^{28}SiH_3^{1+}$ primary beam, we were only able to complete the important low-pressure measurements. For each gas pressure, the technique involved (see fig. 43):

1. measuring the FC4-to-FC1 transmission (with no gas in the target)
2. filling the target to the desired pressure, measuring the FC4-to-FC1 ratio again, and using the transmission to find the average charge state q_{av} after the gas (see eq. (22))
3. running with current on FC1, and then running with current on FCCH (repeating this step for charge states 3+, 4+, 5+, as selected by the MD1 field)

The charge state fractions (CSFs), for each pressure, follow from comparing the currents on FCCH ($I_{FCCH}/q_{selected}$) with the current on FC1 (I_{FC1}/q_{av}). The results are summarized in table XV and figure 68. If we average the results for the 4^+ charge state at all pressures, we find the CSF to use for the $^{26g}Al(p,\gamma)^{27}Si$ measurement:

$$CSF(Si^{4+}) = \eta_{Si4+} = 42 \pm 2\%. \tag{28}$$

Table XV: ^{28}Si charge-state fractions measured at E_{beam} = 179 keV/u, for different target pressures.

P (torr)	q_{av}	$q_{selected}$	CSF (%)
1	3.44(3)	3+ 4+ 5+	42.0(5) 42.5(4) 5.9(2)
1.5	3.44(3)	3+ 4+ 5+	43.2(4) 43.0(5) 5.9(6)
2	3.33(2)	3+ 4+ 5+	42.0(3) 43.3(3) 6.1(2)
3	3.38(6)	3+ 4+ 5+	40.9(8) 39.1(8) 5.0(2)

We can compare this value with results from [Liu03]. They fit a relation

$$\ln(1-\frac{q_{av}}{Z_{beam}}) = -1.4211\left(v_{reduced}\right) + 0.4495 \tag{29}$$

where

$$v_{reduced} = \frac{v_{beam}}{3.6\times10^{6}(Z_{beam})^{0.44515}}$$

to experimental data from their CSD measurements with ^{16}O, ^{24}Mg, ^{23}Na, and ^{15}N beams in H_2 gas. The relation seems to fit well for $0.4 < v_{reduced} < 1.4$. For a q_{av} then, the width of a gaussian distribution centered upon q_{av} can be interpolated from data also in [Liu03] and used to determine CSFs.

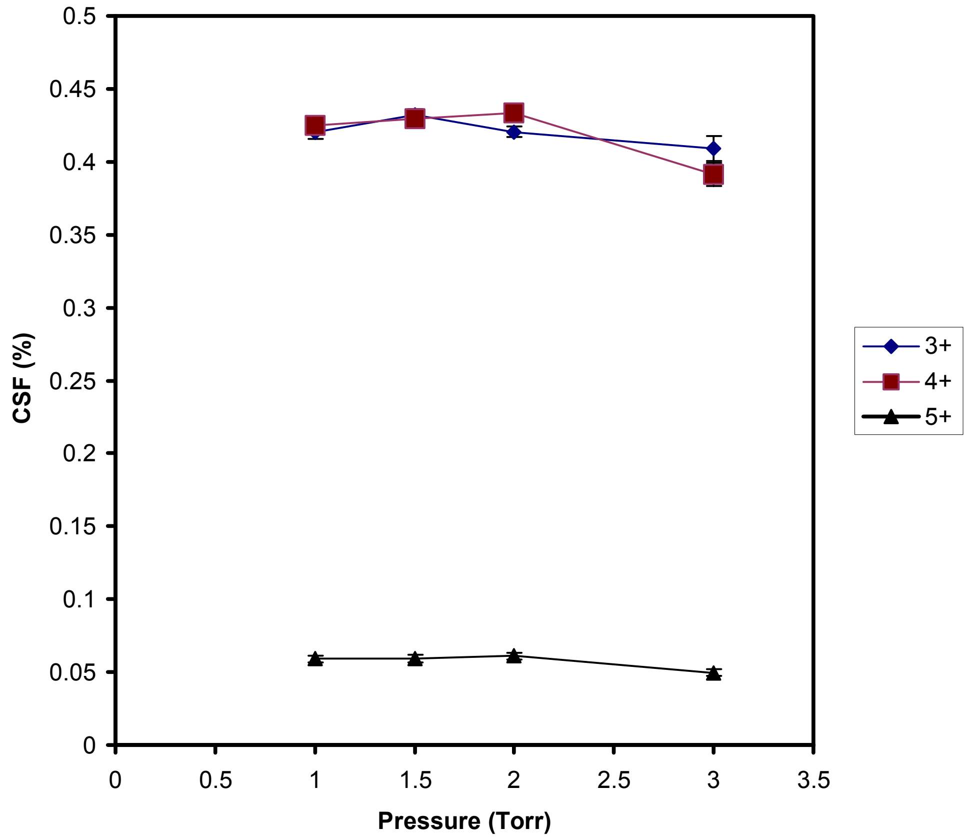

Figure 68: charge-state fractions (CSFs) as a function of H_2 pressure in the target, measured for E_{28Si} = 179 keV/u.

For the ^{28}Si and ^{27}Si velocities given above (5.88 x 10^6 and 5.82 x 10^6 m/s, respectively) we find q_{av} = 3.28 and 3.20 respectively with eq. (29) (both have $v_{reduced}$ = 0.50). Using a distribution width of 0.75 [Liu03], we find CSFs of about 52%, 32% and 4% for charge states 3+, 4+ and 5+. The deviations we find between these calculated CSFs and those measured in table XV are likely due to the dearth of data on CSD widths. Nonetheless, it is encouraging to see the good agreement between the q_{av} calculations and those in table XV and eq. (23).

vii. DRAGON acceptance

The acceptance of DRAGON for ^{27}Si recoils at our beam energies should not be an issue, given the expected maximum recoil cone half-angle of 15.5 mrad relative to design specifications (< 20 mrad) – see section B, ii, a. Nonetheless, GEANT3 simulations incorporating the DRAGON geometry were performed to compare the total number of reactions in the gas target with the number of recoils successfully traversing DRAGON through to the DSSSD position. These simulations were run with the beam entering the target on axis, as well as mistuned by ± 1 mm in a direction normal to the beam axis and/or ± 1 mrad off the beam axis. Three different positions for the reaction within the gas cell were considered (-3 cm, 0 cm, and +3 cm relative to the centre of the gas cell) as well as ^{26g}Al beam energies of 197 and 201 keV/u. In addition, the effect on the acceptance of changing the branching ratios for the decay of the 'E_R^{CM} = 188 keV' resonance (see section C, v) was examined. Finally, it was noticed through tests with an alpha source [Pea06] that the first quadrupole following the gas target (Q1) may have been operating during the experiment at a field +5% different from that expected with a normal tune. The result would be a broadened beam spot that could affect the ^{27}Si recoil transmission through DRAGON. To check this, we ran more simulations with Q1 overfocusing by +5%. (We also simulated the effect of Q1 underfocusing by 5%.) No significant effect on the acceptance of ^{27}Si recoils was found. Considering all this, we used the following efficiency factor for transmission of ^{27}Si recoils:

$$\eta_{sep} = 97.8 \pm 2.0\ \%. \tag{30}$$

viii. Yields and Resonance Strengths

The reaction yield Y is given by

$$Y = \frac{N_{recoils}}{N_{beam}\eta_{BGO}\eta_{sep}\eta_{Si4+}\eta_{DSSSD}} \tag{31}$$

where $N_{recoils}$ and N_{beam} are the number of detected recoils and net ^{26g}Al beam particles respectively (see tables X and XIII). The other factors in this expression are the BGO efficiency η_{BGO} (eq. (27)), the separator transmission η_{sep} (eq. (30)), the charge-state fraction of $^{27}Si^{4+}$ recoils η_{Si4+} (eq. (28)), and the DSSSD efficiency η_{DSSSD} (eq. (15)). Our yields Y at the three beam energies (an upper limit for the off-resonance run, where we conservatively assume the 90% confidence bounds) are given in table XVI and fig. 69.

With these yields and eq. (4), we can calculate the strength of the 'E_R^{CM} = 188 keV' resonance in ^{27}Si. We use the stopping cross-sections ε in eq. (19), the ^{26}Al and p masses from [Aud03], and find the de Broglie wavelength λ with our measured resonance energy (eq. (20)). Our results are given in table XVI. Adopting the result from the higher-statistics 201 keV/u runs, we find

$$\omega\gamma = 34.6 \pm 4.1_{stat} \pm 5.3_{sys} = 35 \pm 7 \quad \mu eV\,. \tag{32}$$

The statistical error is this value arises purely from the error in $N_{recoils}$; the systematic uncertainty incorporates the error in N_{beam} and the error in the four efficiencies of eq. (31). We have added the systematic and statistical errors in quadrature to give an estimate of the total error.

It is important to note that the resonance strengths in table XVI were found using eq. (4) directly – i.e. we have assumed that our measured yields Y correspond to the asymptotic yield Y_{max} from fig. 9. This assumption is justified if the target thickness Δ is much greater than the resonance width Γ. A more accurate yield expression would be [Rol88]

$$\frac{Y(E_{beam})}{Y_{\max}} = \frac{1}{\pi}\left[\arctan\left(\frac{E_{beam} - E_R}{\Gamma/2}\right) - \arctan\left(\frac{E_{beam} - E_R - \Delta}{\Gamma/2}\right)\right]$$

where $Y(E_{beam})$ is the actual measured yield for a finite target thickness. For this experiment, $\Delta \sim 15$ keV (see eq. (19). Our data are not sufficient to determine Γ for the 'E_R^{CM} = 188 keV' resonance, but based on the measurements of [Buc84] for other resonances in the $^{26g}Al(p,\gamma)$ reaction, Γ is probably < 1 keV. With these values, we find $Y(E_{beam}) > 0.95 Y_{max}$; any correction to our derived resonance strengths due to our finite target thickness would seem to be small relative to our uncertainties (see table XVI). Nonetheless, if a future measurement were to find the width of this resonance to be larger than 1 keV, our derived strengths should then be appropriately scaled (e.g. $\Gamma = 2$ keV gives $Y(E_{beam}) = 0.89 Y_{max}$).

Table XVI: Reaction yields and resonance strengths measured for the 'E_R^{CM} = 188 keV' resonance in $^{26g}Al(p,\gamma)^{27}Si$.

	$Y \pm \sigma_{stat} \pm \sigma_{sys}$	$\omega\gamma \pm \sigma_{stat} \pm \sigma_{sys}$ (μeV)
201 keV/u (uncooled)	$(2.4 \pm 0.5 \pm 0.4) \times 10^{-13}$	$32.6 \pm 7.2 \pm 5.1$
201 keV/u (cooled)	$(2.7 \pm 0.4 \pm 0.4) \times 10^{-13}$	$35.9 \pm 4.8 \pm 5.5$
201 keV/u (combined)	$(2.6 \pm 0.3 \pm 0.4) \times 10^{-13}$	$34.6 \pm 4.1 \pm 5.3$
197 keV/u	$(2.7 \pm 0.6 \pm 0.4) \times 10^{-13}$	$36.0 \pm 7.7 \pm 6.1$
226 keV/u	$< 4.3 \times 10^{-14}$	< 6.10

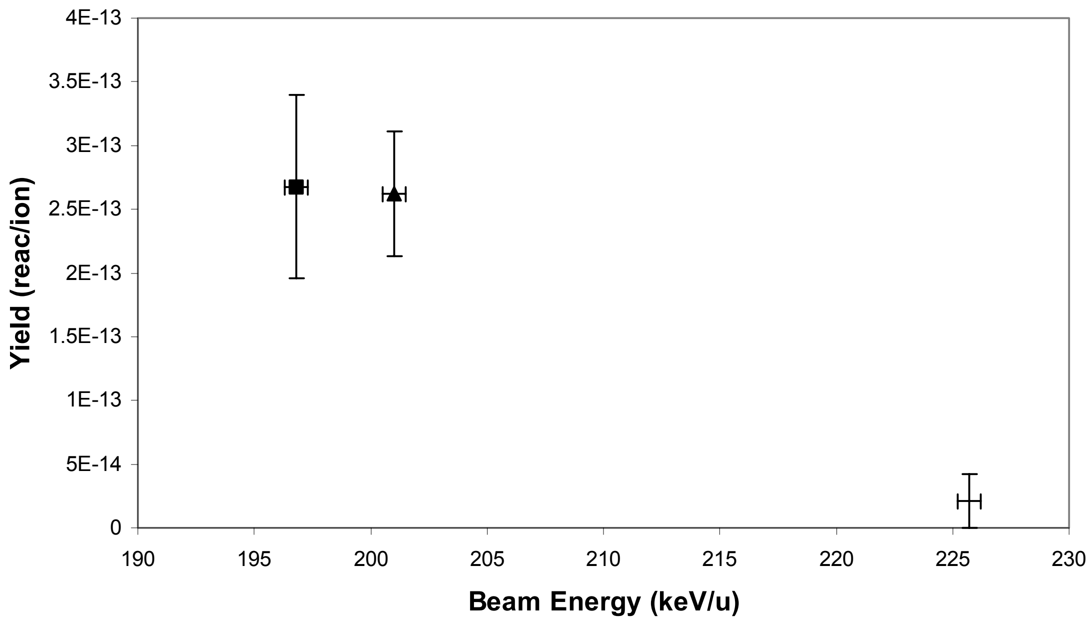

Figure 69: Reaction yields measured for E_{26gAl} = 196.8, 201.0, 225.7 keV/u beams in 6 torr of H_2 gas. We have added statistical and systematic errors in quadrature to give the error bars.

Our result in eq. (32) should be compared to the strength from the direct ^{26g}Al(p,γ) measurement of [Vog89]:

$$\omega\gamma^{[Vog89]} = 55 \pm 9 \quad \mu eV \ . \tag{33}$$

Equation (33) had been determined, however, relative to the strength of the E_p = 406 keV resonance in ^{27}Al(p,γ)^{28}Si. The actual value used for the normalization is not given in [Vog89]; the reduced strength of this ^{28}Si resonance $S = (2J+1)\Gamma_p\Gamma_\gamma/\Gamma$ is given as 0.10 eV in [End78] and 0.077 eV in [End98]. As [End78] was the reference used in [Vog89] to normalize their ^{26g}Al(p,γ) resonance energies (to those for ^{27}Al(p,γ)), we believe it likely that the strength reported in [End78] was indeed used in [Vog89]. Renormalizing the strength in eq. (33) according to the E_p = 406 keV strength from [End98], we find

$$\omega\gamma_{renorm}^{[Vog89]} = (55 \pm 9) \times \frac{0.077}{0.1} = 42 \pm 7 \quad \mu eV\,. \tag{34}$$

(We note that [End78] warns that there are ‘indications’ that the strengths they list are ~40% high [Lyo69]; as no quantitative correction is given, we do not consider that S = 0.10×0.6 = 0.06 eV was used for normalization in [Vog89].) We will refer to eqs. (33) and (34) as the ‘original’ and ‘renormalized’ strength of [Vog89], respectively.
We also give the results extracted from the ^{26g}Al(^{3}He,d) angular distribution measurements in [Vog96] (where pure l transfers were assumed for the DWBA fits):

$$\omega\gamma_{l=\{0,1,2,3\}}^{[Vog96]} = \{290, 64, < 3.2, < 0.099\} \quad \mu eV\,. \tag{35}$$

D. **Discussion**

i. Comparisons

As none of the DWBA calculations leading to eq. (35) fit the experimental data particularly well [Vog96], we confine our comments on $\omega\gamma$ here to the comparison of our result and that in [Vog89]. We find agreement between our measurement of $\omega\gamma$ in eq. (32) and the renormalized [Vog89] measurement in eq. (34) (i.e. the 1σ error bars overlap). Our result disagrees with the original [Vog89] result of eq. (33).

The ^{26g}Al(p,γ) work of [Vog89] measured excitation functions for many ^{26g}Al(p,γ)^{27}Si resonances in normal kinematics, using both NaI and Ge detectors (separately) to observe gamma-rays following the decay of states populated in ^{27}Si. The $\omega\gamma$ measurements involving the NaI detectors (which included the result of eq. (33)) were all normalized to the strength of the E_p = 406 keV resonance in ^{27}Al(p,γ)^{28}Si; the measurements with the Ge detector do not seem to be similarly normalized. For strengths measured in both [Vog89] *with the Ge detector*, and [Buc84] (who used a similar technique), fig. 70 shows a comparison. Although the error bars are large, the strengths of [Vog89] seem to be systematically larger than those of [Buc84] for the higher energy resonances. (The discrepancies at E_R^{CM} = 701 and 893 keV could be explained by the presence of background gamma-rays in the spectra of [Buc84], as mentioned in [Vog89].) Since similar systematic corrections (target deterioration, dead time) were applied to data found using the Ge and NaI detectors, the trend of fig. 70 may help explain why even the renormalized result of [Vog89] in eq. (34) is somewhat larger than our measurement in eq. (32).

The resonance energy we found in eq. (20) is 4 keV lower than that expected from [Vog89]; it is also lower than that expected from the lower-precision measurements of [Sch86] and [Wan89] with particle-transfer reactions. We point to the excellent agreement between our measurement of the E_R^{CM} = 214 keV resonance in ^{24}Mg(p,γ)^{25}Al (eq. (17)) and that of [Pow99] as validation of our technique. The resonance energy of [Vog89] was found relative to the E_p = 202.8 keV resonance in ^{27}Al(p,γ)^{28}Si (which has not changed between [End78] and [End98]). Figure 71 shows a comparison between resonance energies measured in [Buc84] and those found in [Vog89] for resonances in common. The error bars in the results of [Buc84] prevent any definite conclusions, but a trend towards higher measured energies in [Vog89] is suggested.

ii. Implications

Table XVII lists the resonance parameters we suggest for calculation of the ^{26g}Al(p,γ)^{27}Si rate for T < 0.4 GK. We use a weighted average of available energy measurements for E_R^{CM} [Buc84, Sch86, Wan89, Vog89, Lew05, this work]; the corresponding E_x were then found by adding Q = 7462.96(16) keV [Aud03]. When more than one measurement of a strength exists, we use a weighted average. As no measurement or calculation of the width Γ exists for the E_R^{CM} = 366 keV resonance, we do not use the Γ_p/Γ measurement of [Lew05] in the determination of that resonance strength. We consider the strengths from

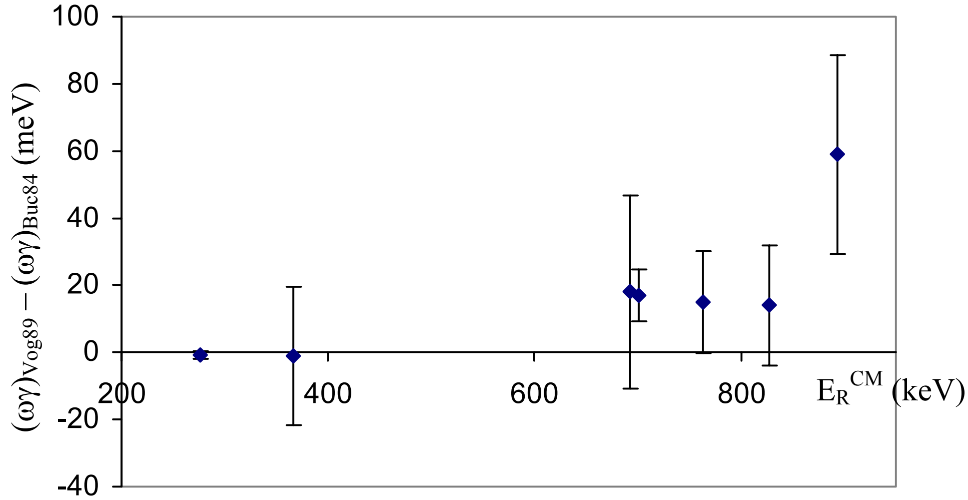

Figure 70: differences in $^{26g}Al(p,\gamma)^{27}Si$ resonance strengths found by [Vog89] and [Buc84] (for resonances measured in common). We only consider the strengths found in [Vog89] from his data taken with the Ge detector, as no renormalization is needed (see text). The error bars in the differences were found by adding the uncertainties in the individual measurements in quadrature. For the resonances at E_R^{CM} = 893 keV (which [Buc84] found as a single state, but [Vog89] found as a doublet) we have added the strengths found in the [Vog89] measurements for the purpose of this comparison.

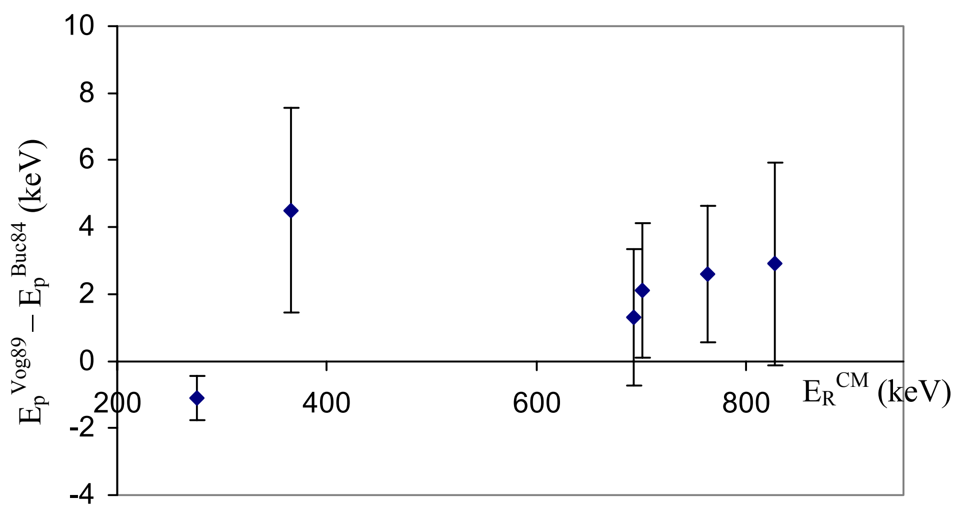

Figure 71: differences in $^{26g}Al(p,\gamma)^{27}Si$ resonance energies found by [Vog89] and [Buc84] (for resonances measured in common). The error bars in the differences were found by adding the uncertainties in the individual measurements in quadrature. We omit the resonances at E_R^{CM} = 893 keV here as [Buc84] found a single state, but [Vog89] found a doublet.

Table XVII: suggested resonance parameters for calculation of the $^{26g}Al(p,\gamma)^{27}Si$ rate in ONeMg nova explosions, see text for details. The lower-adopted-upper format is used for resonances where only calculations or upper limits are available for strengths.

E_R^{CM} (keV)	E_x (keV)	ωγ (meV)			Refs.
		lower	adopted	upper	
5(3)	7468(3)	2.9×10^{-76}	1.5×10^{-75}	2.7×10^{-75}	[Sch86, Wan89, Cha93, Ang99]
69(3)	7532(3)	2×10^{-13}	2.2×10^{-11}	2.2×10^{-10}	[Sch86, Wan89, Cha93, Ang99]
96(3)	7559(3)	2.3×10^{-10}	5.3×10^{-9}	5.3×10^{-8}	[Sch86, Wan89, Cha93, Ang99]
129(2)	7592(2)	0	5.9×10^{-7}	5.9×10^{-6}	[Sch86, Wan89, Vog96, Ang99]
186.2(7)	7649(1)		38 ± 5		[Sch86, Wan89, Vog89, this work]
227(3)	7690(3)	0	0.0008	0.008	[Wan89, Vog89]
237.7(9)	7700.7(9)		0.008 ± 0.004		[Sch86, Wan89, Vog89]
275.7(3)	7738.7(3)		2.4 ± 0.3		[Buc84, Sch86, Wan89, Vog89]
329(2)	7792(2)	0.19	0.2	0.22	[Sch86, Wan89, Cha93, Ang99]
366.4(6)	7829.4(6)		62 ± 6		[Buc84, Sch86, Wan89, Vog89, Lew05]

the $^{26g}Al(^3He,d)$ data of [Vog89] to be superseded by the results in [Vog96]. The renormalization of the strengths from the NaI data of [Vog89] is as in eq. (34). For the possible resonances at E_R^{CM} = 5, 69, 96, and 329 keV, we rely on the shell-model calculations of [Cha93] for strengths. For the possible resonance at E_R^{CM} = 227 keV (seen only in [Wan89]), our 'adopted value' is 1/10 of the (renormalized) upper limit from [Vog89]. Observed states without data or calculations for (p,γ) resonance strengths [Sch86, Wan89, Lew05] are not included in table XVII.

Figure 72 highlights the importance of the strength of the 'E_R^{CM} = 188 keV' resonance. We compare the resonant rate (see eq. (2)) found using our new measurement of the strength in eq. (32) to the rate found using the 'original' strength in eq. (33) ($\omega\gamma$ = 55 μeV, used in the nova nucleosynthesis models of [Jos99]). All other resonance parameters used were as in table XVII ('adopted' values). We see that the greatest change in the resonant rate occurs at about $T \sim 0.08 - 0.2$ GK, in the regime of nova burning temperatures ($T = 0.1 - 0.4$ GK). (Note that the direct capture component of the ^{26g}Al(p,γ) rate should be negligible for $T > 0.02$ GK [Cha93]).

Figure 73 shows the effect on the ^{26g}Al(p,γ)^{27}Si rate of our new measurement of the energy E_R^{CM} of this resonance. We compare the rate found using our measurement (E_R^{CM} = 184 keV) and that using the value of [Vog89] (E_R^{CM} = 188.3 keV); all other resonance parameters used were as in table XVII ('adopted' values). Here we see an increase in the rate of 15 – 50% over nova burning temperatures.

Finally, in fig. 74, we compare the $^{26g}Al(p,\gamma)^{27}Si$ rate found using the energy *and* strength of the 'E_R^{CM} = 188 keV' resonance of the present work with the rate found using the energy and strength from [Vog89] (where we use the 'original' strength, as that was used for the nova models of [Jos99]). In fig. 74 we also compare the rate found using the 'adopted' values in table XVII with the rate found using the 'original' strength and energy of [Vog89]. Over nova temperatures, we see a *net decrease* in the rate of as much as ~15% using our resonance energy and strength or the 'adopted' values. This favours the production of ^{26g}Al in novae, as the destruction of this species is inhibited.

To explore the implications of the new $^{26g}Al(p,\gamma)$ rate on the nova yield of ^{26g}Al, hydrodynamic simulations of nova outbursts -from the onset of accretion on a 1.25 $M_{\odot}$ ONeMg white dwarf up through the explosion and ejection stages- have been computed [Rui06]. (See [Jos98] for details on the model and code.) About ~20% more ^{26g}Al was found in the nova ejecta when the strength and energy of the 'E_R^{CM} = 188 keV' resonance from this work (E_R^{CM} = 184 keV, $\omega\gamma$ = 35 μeV) were used in the simulation compared to that found using the strength and energy from [Vog89] (E_R^{CM} = 188.3 keV, $\omega\gamma$ = 55 μeV). Given the ~3 $M_{\odot}$ of ^{26g}Al in the Galaxy (e.g. [Die06]) and the expected contribution of 0.1 – 0.4 $M_{\odot}$ by novae [Jos97], the results of these simulations support the notion that novae are responsible for a non-negligible, though secondary, fraction of the Galactic ^{26g}Al.

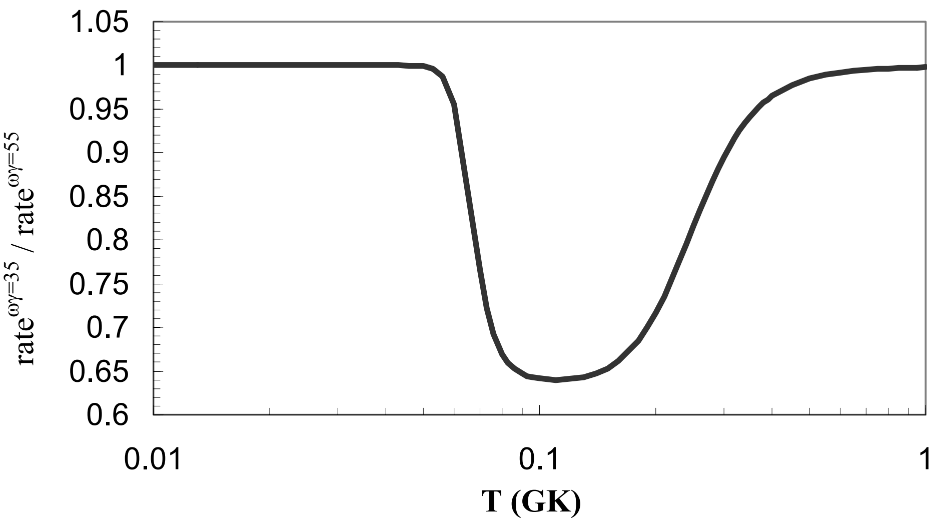

Figure 72: ratio of the resonant $^{26g}Al(p,\gamma)^{27}Si$ rates found using $\omega\gamma = 35$ μeV (this work) and $\omega\gamma = 55$ μeV (the original, ' unrenormalized' value from [Vog89] used with the nova nucleosynthesis models of [Jos99]) for the strength of the 'E_R^{CM} = 188 keV' resonance. All other parameters used in the calculation are from table XVII.

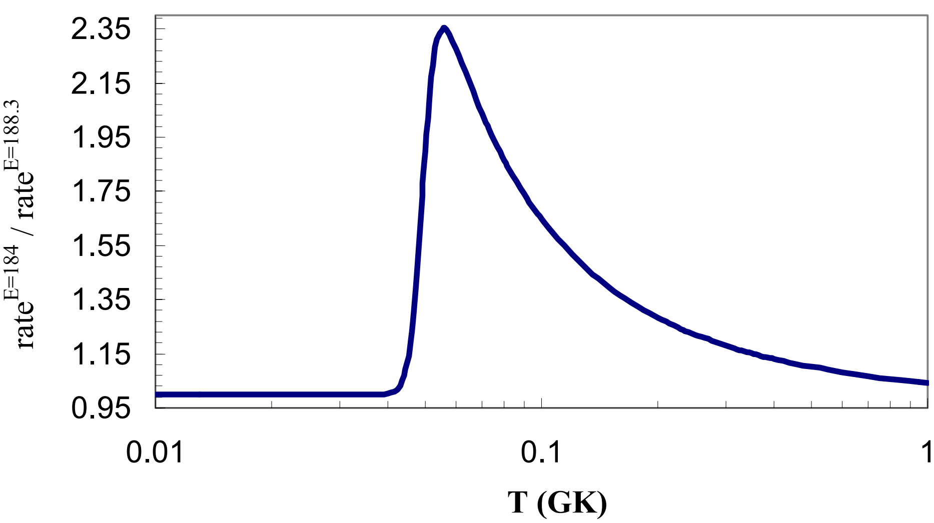

Figure 73: ratio of the resonant $^{26g}Al(p,\gamma)^{27}Si$ rates found using E_R^{CM} = 184 keV (this work) and E_R^{CM} = 188.3 keV [Vog89]. All other parameters used in the calculation are from table XVII.

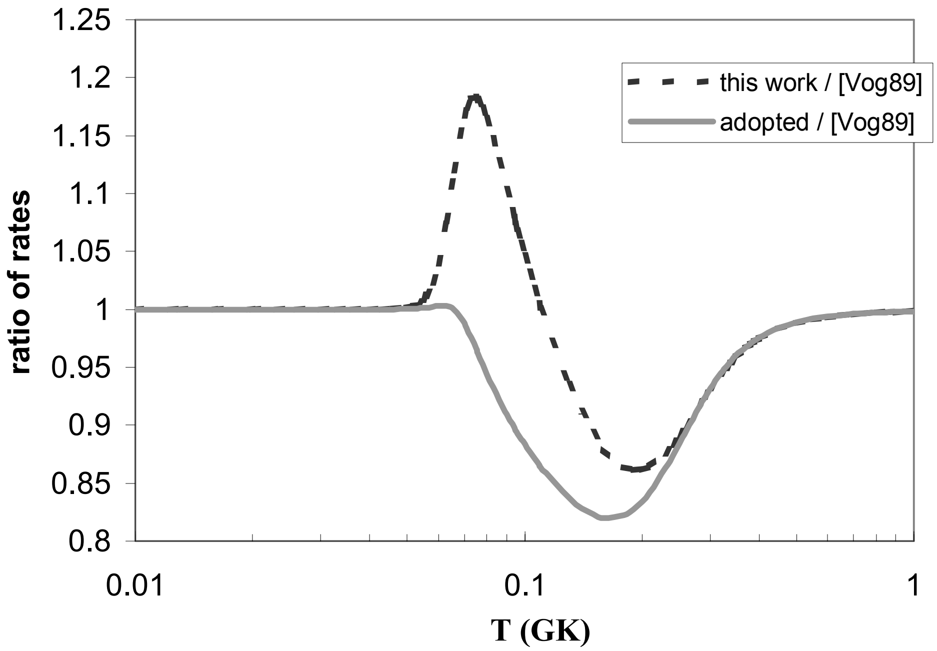

Figure 74: ratios of the resonant $^{26g}Al(p,\gamma)^{27}Si$ rates found using E_R^{CM} = 184 keV and $\omega\gamma$ = 35 μeV (this work) and the 'adopted values' of E_R^{CM} = 186.2 keV and $\omega\gamma$ = 38 μeV (table XVII) to that found using E_R^{CM} = 188.3 keV and $\omega\gamma$ = 55 μeV [Vog89]. All other parameters used in the calculation are from table XVII.

V. CONCLUSIONS

We have made new measurements of the mass of ^{26}Si and the strength and energy of a resonance in the ^{26g}Al(p,γ)^{27}Si reaction to further constrain model calculations for ^{26}Al nucleosynthesis in nova explosions on ONeMg white dwarfs.

Using the ^{28}Si(p,t)^{26}Si reaction, we find $\Delta(^{26}\mathrm{Si}) = -7139.5 \pm 1.0$ keV for the mass excess of ^{26}Si. Our value is 5.5 keV greater than that given in the 2003 atomic mass evaluation: $\Delta(^{26}\mathrm{Si}) = -7145 \pm 3$ keV [Aud03]. (The value in [Aud03] was based upon only one previous measurement [Har74]. Hardy and Towner (2005) use a re-calibration of that measurement, along with selected lower-precision earlier measurements to find $\Delta(^{26}\mathrm{Si}) = -7145.8 \pm 2.9$ keV [Har05a].) We made a simultaneous measurement of the ^{22}Mg mass using the ^{24}Mg(p,t)^{22}Mg reaction: the excellent agreement of our result ($\Delta(^{22}\mathrm{Mg}) = -400.5 \pm 1.0$ keV) with the results from recent high-precision Penning-trap measurements [Sav04, Muk04] lends support to our method. Using our new ^{26}Si mass, we find that the ^{25}Al(p,γ)^{26}Si reaction rate may be reduced by as much as 30% for $T > 0.2$ GK. This is significant as the ^{25}Al(p,γ) reaction leads to the production of ^{26m}Al – which does not decay through the observable 1.809 MeV gamma-ray. A reduction in this rate would tend to increase the amount of ^{26g}Al produced in nova explosions. Our new mass, when used in conjunction with investigations of the excitation energies of low-energy resonances in ^{26}Si [Cag02, Bar02, Par04], will also determine the energy regions of interest in the future direct study of the ^{25}Al(p,γ) ^{26}Si reaction at TRIUMF-ISAC [Che01].

More examinations of the ^{26}Si mass would help to clarify the discrepancy between our result and that of [Aud03] or [Har05a].

Through a direct measurement in inverse kinematics, we found $E_R^{CM} = 184 \pm 1$ keV and $\omega\gamma = 35 \pm 4_{stat} \pm 5_{sys}$ μeV for the centre-of-mass resonance energy and strength, respectively, of the '$E_R^{CM} = 188$ keV' resonance in the ^{26g}Al(p,γ)^{27}Si reaction. The single, unpublished, previous measurement [Vog89] found $E_R^{CM} = 188.3 \pm 1.1$ keV and $\omega\gamma = 55 \pm 9$ μeV (though we believe this strength should be renormalized to $\omega\gamma = 42 \pm 7$ μeV – see Chapter VI, C, viii). Our new measurements reduce the ^{26g}Al(p,γ)^{27}Si rate by as much as 15% over nova temperatures, compared to the rate calculated using the results of [Vog89] (without renormalization, as the model calculations of [Jos99] did not use a renormalized strength). Hydrodynamic simulations of nova outbursts on ONeMg white dwarfs show a net increase by about 20% in the ^{26g}Al yield when our results are used, compared to simulations performed using the [Vog89] results (again, without renormalization) [Rui06]. Gamma-ray measurements of the excitation energy of this ^{27}Si state are needed to resolve the discrepancy between our work and that of [Vog89] for the resonance energy. (The masses of ^{26}Al and ^{27}Si are known to 0.06 and 0.15 keV, respectively [Aud03].) A proposal to produce a ^{26}Al target to study ^{26}Si proton branching ratios via the ^{26}Al(^{3}He,t)^{26}Si*(p)^{25}Al reaction [Dei05] has been accepted at TRIUMF-ISAC; it may be interesting to measure the strength of the '$E_R^{CM} = 188$ keV' resonance in ^{26g}Al(p,γ) again, with this target.

Our results from both the ^{26}Si mass measurement and the study of the resonance in ^{26g}Al(p,γ)^{27}Si imply a slight increase in the nova yield of ^{26g}Al. Nevertheless, our findings confirm novae as *secondary* sources of Galactic ^{26g}Al, with dominant contributions probably arising from core-collapse supernovae and/or Wolf-Rayet stars.

APPENDIX A: $^{26g}Al(p,\gamma)^{27}Si$ measurement in June/July 2005

Over the period of June 18 – July 12, 2005, ISAC produced and accelerated a ^{26g}Al beam to DRAGON to try to measure the 'E_R^{CM} = 188 keV' resonance in the $^{26g}Al(p,\gamma)^{27}Si$ reaction. The beam energy for the majority of runs was 202 keV/u; we switched to 199 keV/u for the final days of the run because of indications of a lower resonance energy (e.g. Chapter IV, C, iii). Figure A1 shows the beam intensities measured at FC4 (see fig. 43) during this experiment. The sharp drop in intensity around run 14950 corresponds to the failure of a power supply used with the laser ionization source; a replacement was unavailable for the remainder of the experiment. The beam intensity for the majority of runs was ~0.03 particle-nA, about 5% of the average beam received in the October 2005 runs (see fig. 49). The level of beam contamination by ^{26m}Al and ^{26}Na was ~ 0.01% and ~0.6%, respectively (see fig. 62). Indeed, the false coincidences triggered by the level of ^{26}Na in the beam prompted us to install the iris and examine other methods to reduce contamination (such as optimizing the beam optics) for the October runs (see table XIII). Due to an oversight, the trigger thresholds on the BGO detectors were set to ~ 2.0 MeV for about 2/3 of the experiment, after which they were reduced to 1.75 MeV. Finally, about halfway through this measurement, operator error resulted in exposure of the DSSSD to the full beam intensity; the detector eventually used for the October measurement replaced it.

To estimate the resonance strength, we consider here only runs from the first half of the experiment (14843 – 14978) as the DSSSD, beam energy (202 keV/u), and BGO

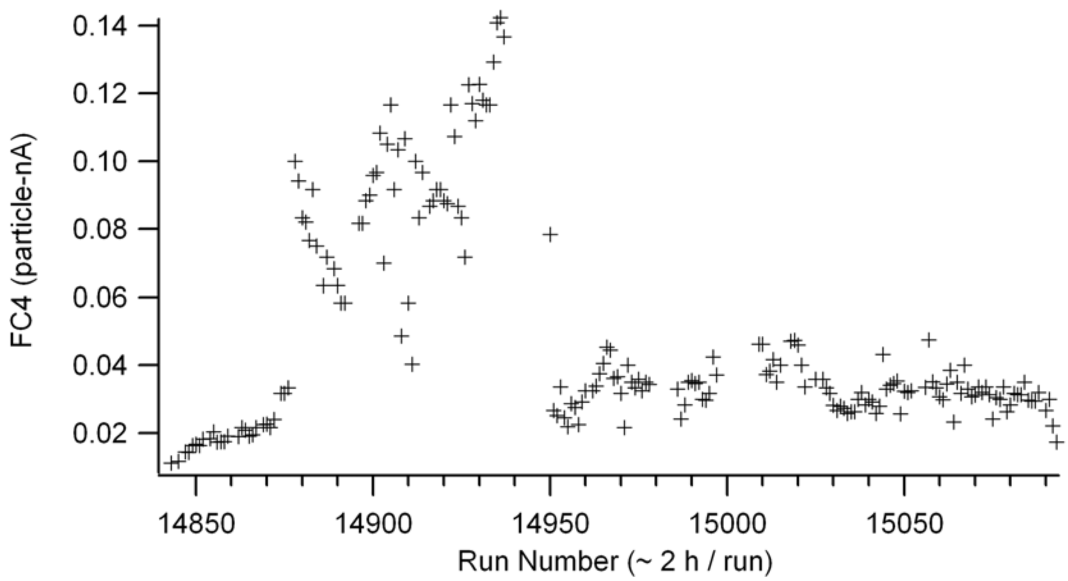

Figure A1: the variation in ^{26g}Al beam intensity measured with the faraday cup FC4 (just upstream of the DRAGON gas target) during the ^{26g}Al(p,γ) measurement of June/July 2005. Note that the iris had not been installed for these runs. A power supply used with the laser ionization source failed after run 14950.

thresholds (2 MeV) were constant throughout. This set also incorporates the period when the laser ionization source was online, allowing the most favourable signal-to-noise ratio. The E_R^{CM} = 214 keV resonance in ^{24}Mg(p,γ) was examined prior to receiving ^{26g}Al beam, just as it was in October. The ^{25}Al recoil peak was seen at channel 6990 in separator TOF, similar to that in fig. 46, so we expect the ^{27}Si recoil peak at channel ~ 7500 in separator TOF (just as in fig. 51). Figure A2 shows separator TOF vs. E_{DSSSD} for the ^{26g}Al runs under consideration; recoils seem to be clustered around channel 7500. We find 17 potential recoils in the ‘recoil cut’ (which used the same cut in separator TOF as that used for the 201 keV ‘uncooled’ October runs), and estimate 7.6 background events from scaling the ‘background cut’. Given the low statistics involved, we rely on the treatment of [Fel98] (which was used to analyze the off-resonance October runs): in

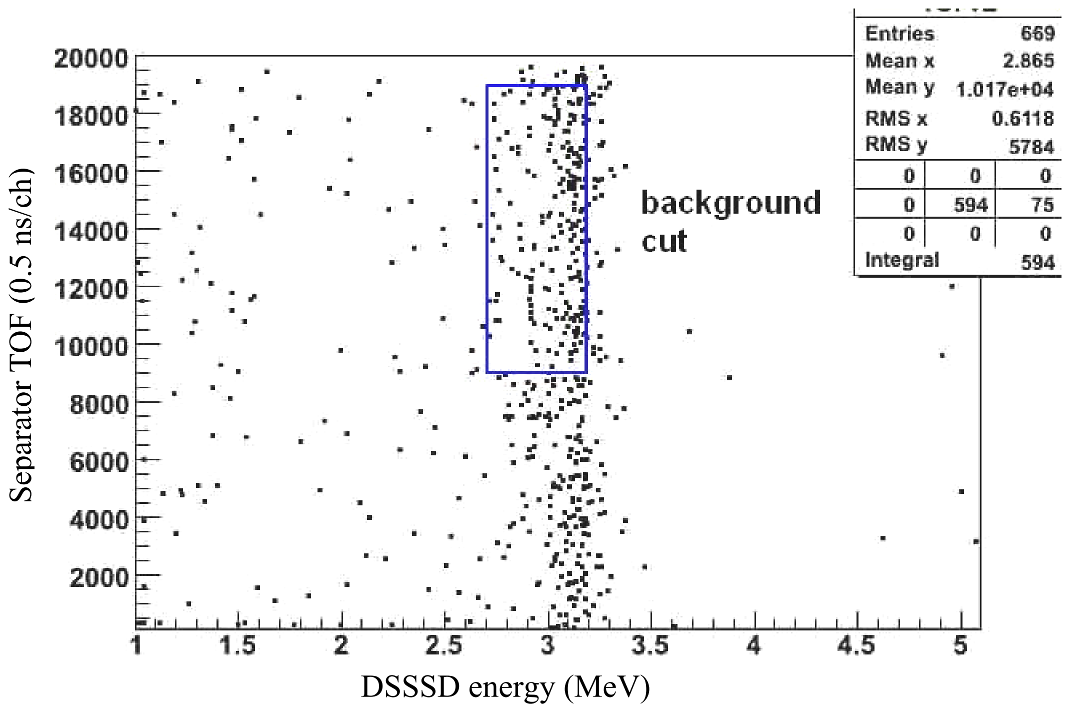

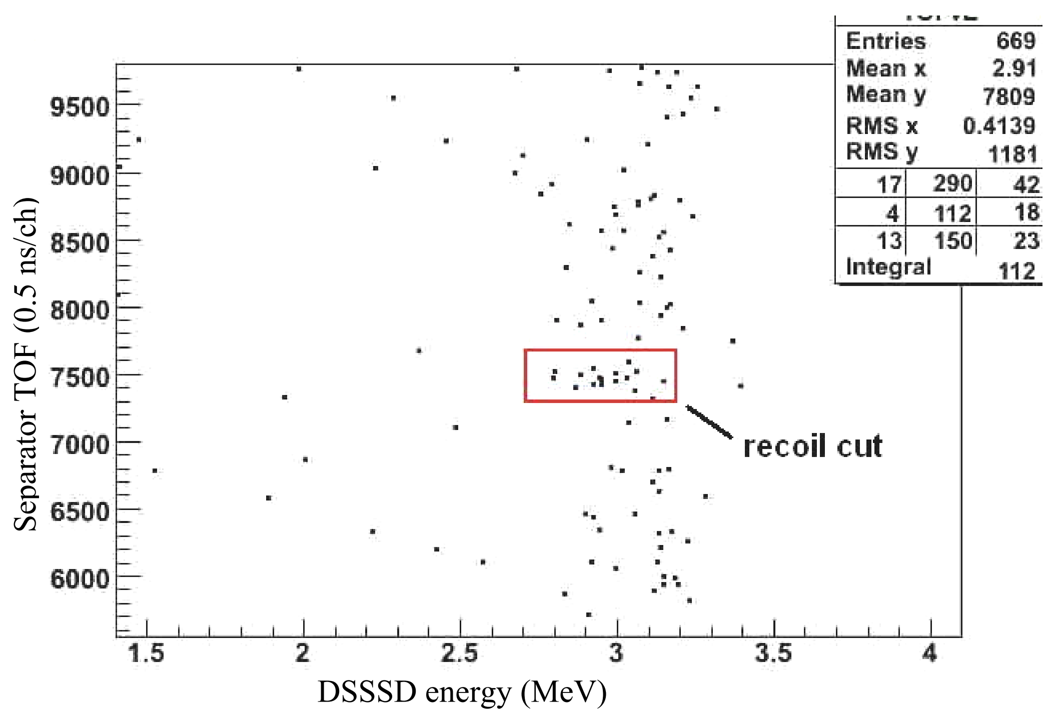

Figure A2: (top) separator TOF vs. E_{DSSSD} spectrum for E_{26gAl} = 202 keV/u runs in June/July 2005 (see text). The cut used to estimate the level of background is indicated. (bottom) same as (top), but zoomed into the region of potential ^{27}Si recoils. The 'recoil cut' (from which the scaled background was subtracted) is indicated. Note that the separator TOF region selected in the 'recoil cut' is the same as that used for the 201 keV/u 'uncooled' runs of October 2005.

68.27% of experiments, the true number of recoils will fall within the range

$N_{recoils} = 9.7 \pm 4.5$.

(Note that this is very similar to the result found from simply subtracting the scaled background from the number of potential recoils, and adopting a statistical error.)

The number of beam particles accepted by the gas target was found using the left mass slit method (see Chapter IV, C, iv) as the amplifier gain on the signal from the elastics detector SB0 had mistakenly been set too low for most of the runs under consideration here. After correcting for ^{26}Na and ^{26m}Al contamination, we found

$N_{beam} = (2.18 \pm 0.11) \times 10^{14}$.

(Note that this value differs from that in [Cra05]: the livetime of the system had not been considered in that work.)

Using the same efficiencies as in the analysis of the October run, as well as the resonance energy from eq. (20) (see Chapter IV, C, viii), we find

$$\omega\gamma = 19.8 \pm 9.5_{stat} \pm 2.9_{sys} = 20 \pm 10 \quad \mu eV \qquad \text{(A1)}$$

(We have also used the 201 keV/u stopping cross-section in eq. (19), which was in agreement with that measured in the June/July runs.) The strength in eq. (A1) is consistent with that in eq. (32). Note that we would also expect a somewhat lower efficiency for the BGO array (increasing the above strength) than we adopted here, as the trigger thresholds were set at 2.0 MeV for the June/July runs, versus 1.75 MeV for the October run (but see also [Cra05]).

APPENDIX B: Data Summary

Run groups used in the analysis presented in Chapter IV, C:

201 keV/u 'uncooled' : runs 15615 – 15661

201 keV/u 'cooled' : runs 15671 – 15731

226 keV/u : runs 15737 – 15752

197 keV/u : runs 15755 – 15778

See table B2 for actual data runs (as opposed to testing and background runs) in these general groups.

Table B1: Normalization constants L_{av}^* and S_{0av} used with eqs. (24) and (26) to determine N_{beam} using the LMS and SB0 methods, respectively, for the four run groups. The uncertainties are standard errors of the mean found using all runs included in the respective groups.

	201 keV/u 'uncooled'	201 keV/u 'cooled'	197 keV/u	226 keV/u
L_{av}*	0.343(3)	0.343(2)	0.352(6)	0.311(3)
S_{0av}	655(33)	666(25)	681(53)	410(34)

Table B2: Summary of N_{beam} as determined with the LMS and SB0 methods (see Chapter IV, C, iv) for all runs used in the analysis presented in Chapter IV, C. The capability to read the current from the LMS was not setup until run 15634. The average pressure in the target during each run is also given, when it was noted.

Run Number	Time (s)	Target Pressure (torr)	N_{beam}(LMS) x10^{13}	$\sigma_{N(LMS)}$ x10^{13}	N_{beam} (SB0) x10^{13}	$\sigma_{N(SB0)}$ x10^{13}
15615	10154	--	--	--	2.518	0.128
15617	10067	6.005	--	--	2.548	0.129
15618	7612	--	--	--	1.493	0.076
15619	3056	--	--	--	0.153	0.008

15623	7249	5.905	--	--	1.030	0.052
15632	10033	6.022	--	--	2.382	0.121
15634	1083	--	0.287	0.011	0.282	0.014
15635	10673	--	2.357	0.093	2.351	0.119
15636	10821	6.089	2.472	0.098	2.456	0.125
15637	9580	6.095	2.005	0.079	2.034	0.103
15639	7480	6.099	1.340	0.053	1.333	0.068
15640	7570	6.094	1.298	0.051	1.256	0.064
15641	3718	6.085	0.501	0.020	0.453	0.023
15642	7277	6.087	1.741	0.069	1.603	0.081
15643	10807	6.079	2.065	0.082	1.917	0.097
15644	10677	6.082	2.283	0.090	2.105	0.107
15645	11160	6.110	2.395	0.095	2.254	0.115
15647	7742	6.125	1.924	0.076	1.937	0.098
15648	7890	6.127	1.819	0.072	1.856	0.094
15649	8110	5.937	2.612	0.103	2.864	0.146
15650	9143	5.968	3.276	0.130	3.349	0.170
15651	9226	6.086	2.780	0.110	2.922	0.149
15652	13647	6.050	5.518	0.218	2.949	0.150
15654	9221	6.060	3.190	0.126	3.318	0.169
15655	9681	6.083	3.666	0.145	3.833	0.195
15657	8127	6.087	2.238	0.089	2.243	0.114
15658	7515	6.036	2.281	0.090	2.308	0.117
15659	7301	6.067	2.076	0.082	2.096	0.107
15660	7271	6.057	2.081	0.082	2.123	0.108
15661	5828	6.050	1.484	0.059	1.502	0.076
15671	7337	6.168	--	--	2.305	0.087
15672	5939	6.187	1.578	0.073	1.571	0.059
15677	10009	6.155	1.964	0.091	1.972	0.075
15678	4150	6.062	1.414	0.066	1.403	0.053
15679	9857	6.098	3.121	0.145	3.148	0.119
15680	2546	6.098	1.087	0.051	1.115	0.042
15681	9706	6.089	3.167	0.147	3.199	0.121
15682	10312	6.079	2.888	0.134	2.911	0.110
15683	10563	6.073	3.212	0.149	3.245	0.123
15684	10832	6.173	2.575	0.120	2.684	0.102
15686	8198	6.083	2.044	0.095	2.109	0.080
15687	7649	6.09	1.885	0.088	1.935	0.073
15688	2940	6.087	0.671	0.031	0.694	0.026
15689	3443	6.436	0.579	0.027	0.601	0.023
15690	2426	6.067	0.303	0.014	0.304	0.012
15691	2426	6.057	2.017	0.094	2.049	0.077
15692	7359	6.0495	1.768	0.082	1.782	0.067
15693	7728	6.055	2.212	0.103	2.252	0.085
15695	6573	6.046	1.789	0.083	1.796	0.068
15696	6995	--	1.625	0.076	1.532	0.058
15697	5376	--	1.325	0.062	1.357	0.051
15698	10754	--	2.363	0.110	2.461	0.093
15699	10765	6.074	2.355	0.110	2.413	0.091

15700	12060	6.063	0.953	0.044	0.889	0.034
15701	8262	6.0245	1.648	0.077	1.659	0.063
15702	7278	6.02	0.103	0.005	0.102	0.004
15703	8106	6.015	1.801	0.084	1.802	0.068
15704	7215	6.005	1.406	0.065	1.420	0.054
15705	6236	6.005	1.180	0.055	1.184	0.045
15706	8419	6.04	1.988	0.093	2.030	0.077
15707	9280	6.075	2.452	0.114	0.527	0.020
15708	10801	6.0825	2.559	0.119	2.630	0.099
15709	10616	6.062	2.620	0.122	2.695	0.102
15710	11060	6.033	2.662	0.124	2.721	0.103
15711	10622	6.031	2.377	0.111	2.347	0.089
15712	2419	6.040	0.344	0.016	0.491	0.019
15713	8079	6.027	1.575	0.073	1.511	0.057
15714	9657	6.012	2.122	0.099	2.080	0.079
15715	7637	--	1.857	0.086	1.831	0.069
15716	323	--	0.072	0.003	0.072	0.003
15717	10643	6.000	2.310	0.108	2.287	0.086
15718	9960	5.994	2.059	0.096	1.998	0.076
15719	10656	5.975	2.283	0.106	2.218	0.084
15721	7666	5.952	1.635	0.076	1.544	0.058
15722	11618	5.931	2.007	0.093	1.867	0.071
15724	7563	5.943	1.842	0.086	1.708	0.065
15726	2901	5.984	0.675	0.031	0.633	0.024
15727	8202	6	4.662	0.217	2.163	0.082
15728	8276	6.030	2.359	0.110	2.230	0.084
15729	7389	6.05	2.039	0.095	1.940	0.073
15730	7388	6.056	2.127	0.099	2.040	0.077
15731	1651	6.064	0.454	0.021	0.437	0.017
15737	5499	6.100	1.561	0.057	1.371	0.115
15738	7433	6.099	1.605	0.059	1.371	0.115
15739	8837	6.134	1.982	0.073	1.741	0.146
15740	8768	6.140	1.986	0.073	1.920	0.161
15741	7153	6.107	1.963	0.072	1.411	0.119
15743	7480	6.085	1.595	0.059	1.661	0.140
15744	7712	6.062	2.528	0.093	2.643	0.222
15745	3019	6.059	0.966	0.035	1.050	0.088
15746	11914	6.044	4.277	0.157	4.509	0.379
15747	7221	6.028	2.209	0.081	2.317	0.195
15748	7402	5.996	2.166	0.080	2.228	0.187
15749	7299	6.072	2.207	0.081	2.310	0.194
15750	9135	6.055	2.295	0.084	2.351	0.198
15751	2746	6.064	0.680	0.025	0.721	0.061
15752	5426	6.067	1.286	0.047	1.363	0.115
15755	12164	6.120	2.717	0.272	2.888	0.225
15756	10227	6.126	2.412	0.241	2.402	0.187
15757	9407	6.116	1.678	0.168	1.635	0.127
15758	8180	6.105	1.321	0.132	1.282	0.100

15759	9640	6.090	1.377	0.138	1.292	0.101
15760	8896	6.080	1.130	0.113	0.288	0.022
15761	7940	--	1.043	0.104	0.978	0.076
15762	8352	6.088	2.204	0.220	2.097	0.163
15765	1617	--	0.362	0.036	0.265	0.021
15766	9543	6.150	2.579	0.258	2.559	0.199
15767	1203	6.159	0.300	0.030	0.298	0.023
15768	10145	6.161	2.246	0.225	2.246	0.175
15769	7728	6.165	1.627	0.163	1.626	0.127
15770	10820	6.163	2.098	0.210	2.094	0.163
15771	9959	6.108	2.374	0.237	1.580	0.123
15772	3816	6.09	0.767	0.077	0.777	0.061
15773	9870	6.125	2.107	0.211	2.216	0.173
15774	10344	6.168	2.343	0.234	2.530	0.197
15775	10055	6.156	1.992	0.199	2.164	0.169
15776	6362	6.16	1.119	0.112	1.197	0.093
15777	4491	6.149	1.851	0.185	0.949	0.074
15778	5212	6.158	0.958	0.096	1.022	0.080

Figure B1 shows N_{beam} *(LMS) /* N_{beam} *(SB0)* for all runs used in the analysis (see table B2) with both LMS and SB0 information. The scatter in the ratios indicates that for most runs, the agreement between the two methods is good to ± 5%. There appear to be nine runs in fig. B1 with ratios that deviate significantly from 1: 15652, 15707, 15712, 15727, 15741, 15760, 15765, 15771, 15777. If we exclude these runs in the analysis, we find the following resonance strengths for the run groups:

201 keV/u combined: $\omega\gamma = 34 \pm 4_{stat} \pm 5_{sys}$ μeV

197 keV/u: $\omega\gamma = 37 \pm 8_{stat} \pm 6_{sys}$ μeV (B1)

226 keV/u: $\omega\gamma < 6.4$ μeV

The above values are in accord with the strengths in table XVI. Since the LMS method is sensitive to the beam tune, and no other problems were seen after examining these nine runs in detail, we chose to include these runs in the determination of our final resonance strengths (table XVI).

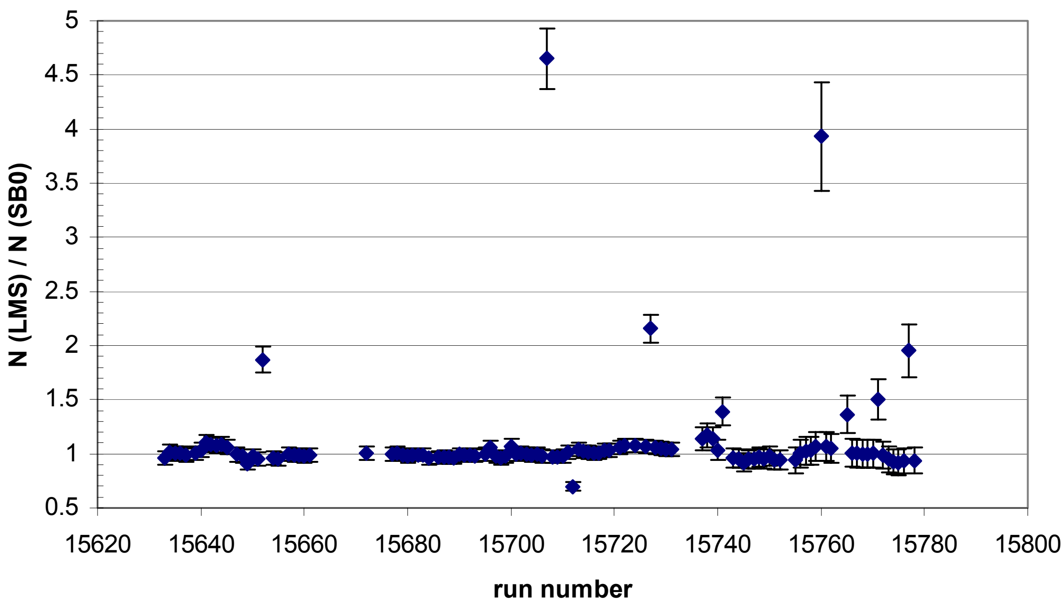

Figure B1: run-by-run ratio of the total number of beam particles N as found from the left mass slit (LMS) data to N as found from the data with the elastics monitor (SB0).

REFERENCES:

[Abb82] D. C. Abbott, Astrophys. J. 263 (1982) 723.

[Alf86] W. P. Alford et al., Nucl. Phys. A457 (1986) 317.

[Ama01a] S. Amari et al., Astrophys. J. 546 (2001) 248.

[Ama01b] S. Amari et al., Astrophys. J. 551 (2001) 1065.

[Ama01c] S. Amari et al., Astrophys. J. 559 (2001) 463.

[And82] E. Anders and M. Ebihara, Geochim. Cosmochim. Acta 46 (1982) 2363.

[Ang99] C. Angulo et al., Nucl. Phys. A656 (1999) 3.

[Aud03] G. Audi et al., Nucl. Phys. A729 (2003) 337.

[Bar02] D. W. Bardayan et al., Phys. Rev. C 65 (2002) 032801R.

[Baz93] G. Bazan et al., Rev. Mex. Astron. Astrofis. 27 (1993) 87.

[Bet85] H. A. Bethe and J. R. Wilson, Astrophys. J. 295 (1985) 14.

[Bis03a] S. Bishop et al., Phys. Rev. Lett. 90 (2003) 162501.

[Bis03b] S. Bishop, PhD Thesis, Simon Fraser University, 2003.

[Boh82] W. Bohne et al., Nucl. Phys. A378 (1982) 525.

[Bra78] J. G. Bradley et al., J. Geophys. Res. 83 (1978) 244.

[Bri97] P. G. Bricault and H. Weick, TRIUMF Design Note TRI-DN-97-15.

[Bri05] P. G. Bricault, private communication.

[Buc84] L. Buchmann et al., Nucl. Phys. A415 (1984) 93.

[Bur57] E. M. Burbidge et al., Rev. Mod. Phys. 29 (1957) 547.

[Bus99] M. Busso et al., Ann. Rev. Astron. Astrophys. 37 (1999) 239.

[Cag02] J. A. Caggiano et al., Phys. Rev. C 65 (2002) 055801.

[Cal73] F. Calligaris et al., Nucl. Instr. Meth. 112 (1973) 591.

[Car96] B. W. Carroll and D. A. Ostlie, **An Introduction to Modern Astrophysics** (Addison-Wesley Publishing Company, Inc.: Reading, Mass.) 1996.

[Cha82] A. E. Champagne, PhD Thesis, Yale University, 1982.

[Cha93] A. E. Champagne et al., Nucl. Phys. A556 (1993) 123.

[Che01] A. A. Chen et al., TRIUMF EEC Proposal E922 (unpublished).

[Coc95] A. Coc et al., Astron. Astrophys. 299 (1995) 479.

[Cor02] J. M. Cordes and T. J. W. Lazio, astro-ph/0207156.

[Cra05] H. Crawford, Summer Work Report, 2005. See http://dragon.triumf.ca

[CRC04] http://www.hbcpnetbase.com/

[Dei05] C. Deibel et al., TRIUMF EEC Proposal E1071 (unpublished).

[Die03] R. Diehl et al., Astron. Astrophys. 411 (2003) L451 and references therein.

[Die06] R. Diehl et al., Nature 439 (2006) 45.

[DRA] http://dragon.triumf.ca/

[Edm] http://www.edmundoptics.com/

[End78] P. M. Endt and C. van der Leun, Nucl. Phys. A310 (1978) 1.

[End90] P. M. Endt, Nucl. Phys. A521 (1990) 1.

[End98] P. M. Endt, Nucl. Phys A633 (1998) 1.

[Eng79] H. A. Enge, Nucl. Instr. Meth. 162 (1979) 161.

[Eng03] S. Engel, PhD Thesis, Ruhr-Universitat Bochum, 2003.

[Eng05] S. Engel et al., Nucl. Instr. Meth. Phys. Res. A 553 (2005) 491.

[Esa78] T. M. Esat et al., Geophys. Res. Lett. 5 (1978) 807.

[Fel98] G. J. Feldman and R. D. Cousins, Phys. Rev. D 57 (1998) 3873.

[Gal03] C. Galt, Summer Work Report, 2005. See http://dragon.triumf.ca

[GEA] http://wwwasd.web.cern.ch/wwwasd/geant/

[Geh98] R. D. Gehrz et al., PASP 110 (1998) 3.

[Gig04] D. Gigliotti, MSc Thesis, University of Northern British Columbia, 2004.

[Gil03] P. Gil-Pons et al., Astron. Astrophys. 407 (2003) 1021.

[Har74] J. C. Hardy et al., Phys. Rev. C 9 (1974) 252.

[Har03] J. C. Hardy et al., Phys. Rev. Lett. 91 (2003) 082501.

[Har05a] J. C. Hardy and I. S. Towner, Phys. Rev. C 71 (2005) 055501.

[Har05b] M. J. Harris et al., Astron. Astrophys. 433 (2005) L49.

[Her04] M. Hernanz and J. Jose, New Astron. Rev. 48 (2004) 35.

[Hig04] J. C. Higdon et al., Astrophys. J. 611 (2004) L29.

[Hil00] W. Hillebrandt and J. Niemeyer, Ann. Rev. Astron. Astrophys. 38 (2000) 191.

[Hut03] D. A. Hutcheon et al., Nucl. Instr. Meth. Phys. Res. A 498 (2003) 190.

[Ili96] C. Iliadis et al., Phys. Rev. C 53 (1996) 475.

[Ili01] C. Iliadis et al., Astrophys. J. S. 134 (2001) 151.

[Ili02] C. Iliadis et al., Astrophys. J.S. 142 (2002) 105.

[Iyu94] A. F. Iyudin et al., Astron. Astrophys. 284 (1994) L1.

[JAM] http://sourceforge.net/projects/jam-daq/

[Jew05] C. Jewett, PhD Thesis, Colorado School of Mines (2005).

[Jos97] J. Jose et al., Astrophys. J. 479 (1997) L55.

[Jos98] J. Jose and M. Hernanz, Astrophys. J. 494 (1998) 680.

[Jos99] J. Jose et al., Astrophys. J. 520 (1999) 347.

[Jos04] J. Jose et al., Astrophys. J. 612 (2004) 414.

[Kno79] G. F. Knoll, **Radiation Detection and Measurement** (John Wiley and Sons: New York) 1979.

[Kno99] J. Knodlseder, Astrophys. J. 510 (1999) 915.

[Koe03] U. Koester et al., Spec. Chim. Acta B, 58 (2003) 1047.

[Kra88] K. S. Krane, **Introductory Nuclear Physics** (John Wiley and Sons: New York) 1988.

[Kre03] K. Kretschmer et al., Astron. Astrophys. 412 (2003) L47.

[Kur92] J. D. Kurfess et al., Astrophys. J. 399 (1992) L137.

[Lam04] M. Lamey, MSc Thesis, Simon Fraser University, 2004.

[Lee76] T. Lee et al., Geophys. Res. Lett. 3 (1976) 41.

[Lee77] T. Lee et al., Astrophys. J. 211 (1977) L107.

[Lee79] T. Lee et al., Astrophys. J. 228 (1979) L93.

[Lew05] R. Lewis, PhD Thesis, Yale University, 2005.

[Lim03] G. Limongi and A. Chieffi, Astrophys. J. 592 (2003) 404.

[Lin99] G. Lindstrom et al., Nucl. Instr. Meth. A 426 (1999) 1.

[Liu03] W. Liu et al., Nucl. Instr. Meth. Phys. Res. A 496 (2003) 198.

[Lor77] J. C. Lorin et al., Meteoritics 12 (1977) 299.

[Lyo69] P. B. Lyons et al., Nucl. Phys. A130 (1969) 1.

[Mah82] W. A. Mahoney et al., Astrophys. J. 262 (1982) 742.

[Mah88] W. A. Mahoney et al., Astrophys. J. 334 (1988) L81.

[Mey97] G. Meynet et al., Astron. Astrophys. 320 (1997) 460.

[Mey02] J. D. Meyer et al., Nucl. Meth. Phys. Res. B 190 (2002) 379.

[MID] http://midas.psi.ch/

[Mor95] D. J. Morris et al. in **Seventeenth Texas Symposium on Relativistic Astrophysics and Cosmology**, eds. H. Bohringer, G. E. Morfill and J. Trumper (New York Academy of Sciences: New York) 1995, p. 397.

[Mow00] N. Mowlavi and G. Meynet, Astron. Astrophys. 361 (2000) 959.

[Muk04] M. Mukherjee et al., Phys. Rev. Lett. 93 (2004) 150801.

[Nay96] J. E. Naya et al., Nature 384 (1996) 44.

[NASA] NASA's Beyond Einstein Roadmap Images Library: http://universe.nasa.gov/be/library/accretion-disk.jpg

[NIC9] A. Chieffi, R. Diehl and R. Hoffman, discussion at Nuclei in the Cosmos IX, Geneva, June 2006.

[NOVA] http://daq-plone.triumf.ca/nova/

[Obe96] U. Oberlack et al., Astron. Astrophys. Suppl. Series 120 (1996) 311.

[Oul07] C. V. Ouellet, PhD Thesis, McMaster University (2007).

[Ove69] J. C. Overley et al., Nucl. Instr. Meth. 68 (1969) 61.

[Oxo87] K. Oxorn et al., Nucl. Instr. Meth. Phys. Res. B 26 (1987) 143.

[Pad72] R. A. Paddock, Phys. Rev. C 5 (1972) 485.

[Pal05] A. Palacios, Astron. Astrophys. 429 (2005) 613.

[Par04] Y. Parpottas et al., Phys. Rev. C 70 (2004) 065805.

[Par05] A. Parikh et al., Phys. Rev. C 71 (2005) 055804.

[Pea06] J. Pearson, private communication.

[Plu01] S. Pluschke et al. in **Exploring the Gamma-Ray Universe: Proceedings of the Fourth INTEGRAL Workshop**, eds. A. Giminez, V. Reglero, and C. Winkler (ESA SP-459: Noordwijk, The Netherlands) 2001, p. 55; S. Plüschke, PhD Thesis, TU München, 2001.

[Pow99] D. C. Powell et al., Nucl. Phys. A660 (1999) 349.

[Pra96] N. Prantzos and R. Diehl, Phys. Rep. 267 (1996) 1.

[Pra04] N. Prantzos, Astron. Astrophys. 420 (2004) 1033.

[Rau02] T. Rauscher et al., Astrophys. J. 576 (2002) 323.

[Rau04] C. Rauth et al., Nucl. Instr. Meth. B 215 (2004) 268.

[Ray95] M. Rayet et al., Astron. Astrophys. 298 (1995) 517.

[Rol73] C. Rolfs, Nucl. Phys. A217 (1973) 29.

[Rol88] C. E. Rolfs and W. S. Rodney, **Cauldrons in the Cosmos** (The University of Chicago Press: Chicago) 1988.

[ROOT] http://root.cern.ch/

[Rou04] T. Rounsaville, "Tedector User's Manual" (unpublished).

[Rui06] C. Ruiz et al., Phys. Rev. Lett. 96 (2006) 252501.

[Run01] R. C. Runkle et al., Astrophys. J. 556 (2001) 970.

[Rya99] S. G. Ryan et al., Astrophys. J. 523 (1999) 654.

[Sav04] G. Savard et al., Phys. Rev. C 70 (2004) 042501(R).

[Sch86] P. Schmalbrock et al., Nucl. Phys. A457 (1986) 182.

[Sch00] V. Schonfelder et al., Astron. Astrophys. Suppl. 143 (2000) 145.

[Sch01] H. Schatz et al., Phys. Rev. Lett. 86 (2001) 3471.

[Sew05] D. Seweryniak et al., Phys. Rev. Lett. 94 (2005) 032501.

[Smi03] D. M. Smith, Astrophys. J. 589 (2003) L55.

[Smi04a] D. M. Smith, New Astron. Rev. 48 (2004) 87.

[Smi04b] D. M. Smith in **Proceedings of the 5th INTEGRAL Workshop on the INTEGRAL Universe**, eds. V. Schönfelder, G. Lichti and C. Winkler (ESA SP-552) 2004, p.45.

[Spe67] J. E. Spencer and H. A. Enge, Nucl. Instr. Meth. 49 (1967) 181.

[SRIM] J. Ziegler, http://www.srim.org/

[Swa01] K. B. Swartz et al., Nucl. Instr. Meth. Phys. Res. A 463 (2001) 354.

[Tay93] J. H. Taylor and J. M. Cordes, Astrophys. J. 411 (1993) 674.

[Tho04] J.-C. Thomas et al., Eur. J. Phys. A21 (2004) 419.

[Tim95] F. X. Timmes et al., Astrophys. J. 449 (1995) 204.

[Tol06] A. Tollsion, Edmund Optics, private communication.

[Vin01] J. Vink et al., Astrophys. J. 560 (2001) L79.

[Vog89] R. B. Vogelaar, PhD Thesis, California Institute of Technology (1989).

[Vog96] R. B. Vogelaar et al., Phys. Rev. C 53 (1996) 1945.

[Wan89] T. F. Wang et al., Nucl. Phys. A499 (1989) 546.

[War80] R. A. Ward and W. A. Fowler, Astrophys. J. 238 (1980) 266.

[Was82] G. J. Wasserburg and D. A. Papanastassiou in **Essays in Nuclear Astrophysics**, eds. C. A. Barnes, D. D. Clayton and D. N. Schramm (Cambridge Press) 1982, p. 77.

[Wil67] R. G. Wilson, IEEE Trans. Nuc. Sci. (1967) 72.

[Woo95] S. Woosley and T. Weaver, Astrophys. J.S. 101 (1995) 181.

[Woo04] S. E. Woosley et al., Astrophys. J.S. 151 (2004) 75.

[Wre03a] C. Wrede, MSc Thesis, Simon Fraser University, 2003.

[Wre03b] C. Wrede et al., Nucl. Instr. Meth. Phys. Res. B 204 (2003) 619.

[Yor87] J. Yorkston et al., Nucl. Instr. Meth. A 262 (1987) 353.